

X-660-73-245

PREPRINT

NASA TM X-70463

PROPORTIONAL COUNTER OBSERVATIONS OF DISCRETE GALACTIC X-RAY SOURCES

(NASA-TM-X-70463) PROPORTIONAL COUNTER
OBSERVATIONS OF DISCRETE GALACTIC X-RAY
SOURCES Ph.D. Thesis - Maryland Univ.

N73-31708

(NASA) 493 P

12.00

CSSL 03B

Unclass

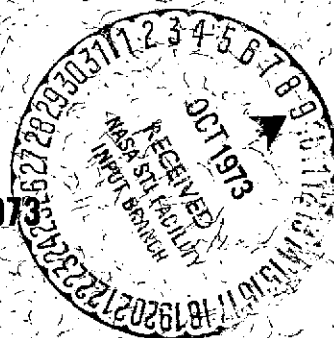
197

G3/29

13777

AXEL FERDINAND BRISKEN

AUGUST 1973



GODDARD SPACE FLIGHT CENTER
GREENBELT, MARYLAND

PROPORTIONAL COUNTER OBSERVATIONS OF
DISCRETE GALACTIC X-RAY SOURCES

by
Axel Ferdinand Briskén

Dissertation submitted to the Faculty of the Graduate School
of the University of Maryland in partial fulfillment
of the requirements for the degree of
Doctor of Philosophy
1973

*Support in part by NASA Grant NGL 21-002-033

/

ABSTRACT

A sounding rocket experiment launched from White Sands Missile Range on May 19, 1972 carried two multilayer multianode xenon filled proportional counters and observed the supernova remnants Cas A and Tycho. No evidence for a stable 2 to 10 keV periodic emission from Cas A or Tycho in the period range of .001 to 10.0 seconds is found. Upper limits to the pulsed fraction are presented as a function of the assumed light curve, with absolute 99% confidence upper limits of 0.089 and 0.195 for Cas A and Tycho, respectively.

Analysis of the spectral data revealed that no single component synchrotron or thermal bremsstrahlung model would adequately represent the data, nor would combinations of these, for both Cas A and Tycho. The main features of the spectra include a steep continuum and a broad emission feature at 7 keV. Synchrotron model fits to the continuum alone are rejected because the spectra would be too steep to have a break by a factor of 1/2 when compared with radio observations and because their intensity at low energies would exceed the extrapolated radio data.

To explain the broad emission feature at 7 keV, a model was developed in which supernova ejecta collide with the interstellar gas

producing characteristic X-rays via charge exchange and continuum power law X-ray emission via non thermal bremsstrahlung. This ejecta is assumed to resemble low energy cosmic rays in composition and energy spectrum. Furthermore, this ejecta energy distribution is assumed to have a collisionally induced lower cut off energy going as Z^2/A . The explanation provided by this model gives the first direct evidence yet obtained for the emission of subrelativistic energetic nuclei by a supernova. Such nuclei are severely excluded from the inner solar system by the solar wind.

For Cas A, this low energy cosmic ray model producing X-rays via charge exchange and non thermal bremsstrahlung required an iron collisional cut off energy of 17 MeV/nucleon and the addition of a thermal bremsstrahlung continuum with $kT = .5$ keV to produce an acceptable fit. The inferred thermal bremsstrahlung is found to be inadequate to produce the observed HII region; sufficient ionization can be obtained from the charge exchange/non thermal bremsstrahlung component.

Folding the identical model through the data from Tycho with an iron collisional cut off energy of 7 MeV/nucleon necessitated a low energy thermal continuum of $kT = .38$ keV to provide acceptable fits. An inferred excess electron density suggests that possibly the ejecta from Tycho contains relatively few or no protons.

In a series of balloon flights with a 600 cm² multilayer multi-anode xenon filled proportional counter, hard X-ray observations of Cyg X-1, Cyg X-2 and Cyg X-3 were made. On June 19, 1972, Cyg X-1 was observed for approximately 1000 seconds and found to exhibit no periodicities in the hard X-ray band in the .1 to 156 Hz band with

99% confidence upper limits to the pulsed fraction of 18%. Spectral analysis in the 15 to 60 keV band suggested a power law fit of $.17 \text{ E}^{-1.15} \text{ photons/cm}^2 \text{ sec keV}$; a thermal bremsstrahlung model was rejected. Rapid transits of Cyg X-2 and Cyg X-3 on June 19, 1972 resulted in a detectable emission consistent with previous observations. An observation of Cyg X-3 on August 31, 1972 suggested no detectable emission from Cyg X-3 with 10σ upper limits in the 14 to 33 keV band placing the intensity a factor of 20 below previous observations at a level of $3.5 \times 10^{-10} \text{ ergs/cm}^2 \text{ sec}$. A weak radio flare at 3.7 cm with an intensity change from .012 to .040 flux units had no corresponding observable emission in the hard X-ray region.

ACKNOWLEDGEMENTS

I wish to express my sincere thanks to the many people who contributed to the success of this research, which was conducted in its entirety with the X-Ray Group of the Laboratory for High Energy Astrophysics at NASA Goddard Space Flight Center. In particular, I wish to thank my advisor, Dr. Frank B. McDonald, for continued encouragement and for providing all the necessary facilities for the conduct of this work.

From the X-Ray Group, I would like to thank Dr. Peter Serlemitsos, who directed most of my experimental efforts, and who lead the expedition to White Sands Missile Range for the launch of the sounding rocket experiment, and Dr. Elihu Boldt and Dr. Stephen Holt for the many discussions and suggestions which contributed to the development of the experiment, the understanding of the physical principles involved, and the completion of the analysis.

From the X-Ray Laboratory, Mr. Charles Glasser's continued enthusiasm and willing help through all difficulties was an inspiration. Mr. Frank Birsa's precise and exact electronics support, Mrs. Julie Saba's meticulous support with calibrations and tests, and Mr. Michael Ziegler's and Mr. Emanuel Karageorge's support in the fabrication of components are greatly appreciated.

For the sounding rocket experiment, I wish to thank the Sounding Rocket Branch of NASA Goddard Space Flight Center for a perfect rocket flight, particularly Mr. Thomas Budney and Mr. David Shrewsberry for the tedious work in checking the alignment of the guidance system.

Also to be recognized are the U. S. Navy and Goddard launch crew at White Sands Missile Range for an excellent launch, and the U. S. Army for a swift recovery of the experiment.

During the field trip to Palestine, Texas for the launch of balloon flight 646-P, I wish to acknowledge the many suggestions on the conduct of balloon experiments from Dr. Daniel Schwartz. For balloon flight 683-P, Mr. Charles Glasser provided invaluable physical support. The willingness to provide perfect flights plus the technical competence of the crew from the National Center for Atmospheric Research Balloon Flight Station for all of the balloon experiments is gratefully acknowledged.

For drafting support both in the design of equipment and the layout of results, Mr. Adam Thompson, Mr. Frank Shaffer, and Mr. Harry Trexel provided swift and excellent quality work. For secretarial support I wish to note Mrs. Barbara Shavatt, Mrs. Barbara Dallas, and Mrs. Rose Ramberg, and finally, Mrs. Naomi Howe, who typed this manuscript.

This research position was approved by Dr. Howard Laster, Director of the Department of Physics and Astronomy, and supervised by Dr. Elske v. P. Smith, under National Aeronautics and Space Administration Grant NGR-21-002-316.

Lastly I wish to recognize the entire staff of the Laboratory of High Energy Astrophysics who were always willing to discuss any problem and offered many free suggestions.

TABLE OF CONTENTS

Chapter	Page
ACKNOWLEDGEMENTS	iii
LIST OF TABLES	ix
LIST OF FIGURES	xi
I. INTRODUCTION	1
A. Electromagnetic Astronomy	1
B. X-Ray Astronomy	3
1. Historical Development	3
2. Present Understand of X-Ray Astronomy	5
3. Purpose of this Study	8
II. MECHANISMS FOR THE PRODUCTION OF X-RAYS	12
A. General Discussion	12
B. Non Thermal Processes	12
1. Synchrotron Radiation	12
2. Inverse Compton Scattering	15
3. Nuclear Processes	16
4. Non Thermal Bremsstrahlung	16
5. Charge Exchange	18
C. Thermal Processes	19
1. Blackbody Radiation	19
2. Optically-Thin Thermal Bremsstrahlung	20
3. Optically-Thin Radiative Recombination	22
4. Optically-Thin Line Emission	22
5. Power Emitted from Optically-Thin Sources	23
6. Optically-Thick Sources	24

Chapter	Page
III. DESCRIPTION OF THE INSTRUMENTS	25
A. Proportional Counters	25
B. Detector Description	27
1. Detector Logic	27
2. Rocket Borne Detectors	28
3. Balloon Borne Detector	28
C. Energy Calibration	29
1. Photoelectric Interaction	29
2. Balloon Experiment Resonance Escape/ Photoelectron Anticoincidence	30
3. Rocket Experiment Resonance Escape/ Photoelectron Anticoincidence	33
4. Linearity	35
5. Resolution	36
D. Electronics and Timing	36
E. Collimation	40
F. Comparison of Balloon Experiment	42
IV. OBSERVATIONAL PROGRAM	44
A. Summary of Flights	44
B. Rocket Flight 13.009	44
C. Balloon Program	46
1. Gondola System	46
2. Balloon Flight 646-P	49
3. Balloon Flight 683-P	49
4. Balloon Flight 695-P	53

Chapter	Page
5. Balloon Flight 696-P	53
V. RESULTS AND DISCUSSION	55
A. Data Analysis Procedure	55
1. Spectral Analysis	55
2. Temporal Analysis	59
3. Background Subtraction	62
4. Interstellar Absorption	63
B. Cas A Observation	64
1. Temporal Analysis	64
2. Spectral Analysis - First Order	67
3. Spectral Analysis - Charge Exchange	69
C. Tycho Observation	77
1. Temporal Analysis	77
2. Spectral Analysis	78
D. Discussion of Cas A and Tycho	79
E. Cyg X-1	88
1. Temporal Analysis	88
2. Spectral Analysis	89
3. Discussion	91
F. Cyg X-2	93
G. Cyg X-3	93
1. Observation	93
2. Discussion	96

Chapter	Page
VI. SUMMARY	98a
APPENDIX. Star Field Analysis	99
REFERENCES	103
TABLES	111
FIGURES	136

LIST OF TABLES

Table	Page
3.1 Relative Probabilities, α , for Photoelectric Absorption into Various Shells	111
3.2 Interaction Probabilities for an X-Ray with the K-Shell of Xenon	112
3.3 Interaction Probabilities for an X-Ray with the L-Shell of Xenon	113
3.4 Fractions of Fluorescence Photons Leaving the Balloon Detector (Resonance Escape) and Remaining in the Same Cell, for Initial Photon Energies ≥ 15 keV	114
3.5 Fractions of Fluorescence Photons Leaving the Rocket Detectors (Resonance Escape) and Remaining in the Same Cell	115
3.6 X-Ray Lines from Laboratory Calibration Sources	116
3.7 Fractional Inhibit and Dead Times in Balloon and Rocket Electronics Systems	119
3.8 Collimator Parameters for the Balloon and Rocket Detectors	120
3.9 Results of Study to Determine the Amount of Bowing of the $1/2^\circ$ Collimator in a Vacuum	121
3.10 Typical Balloon Experiments in X-Ray Astronomy	122
4.1 Summary of the Observational Program	123
4.2 Temporal History of Rocket Flight 13.009	124
4.3 Summary of Rocket Observation Times	125
4.4 Effective Exposure to Sources, Balloon Flight 683-P ...	126
5.1 Relative Abundances of Elements in the Interstellar Gas	127
5.2 Comparison of Observed Probability Distributions in 10.49 sec Fourier Analyses of Cas A with That Expected from Random Data	128

Table		Page
5.3	Summary of Models Tested on the Cas A Spectrum as a Function of Chi-Square per Degrees of Freedom	129
5.4	Summary of Models Tested on the Tycho Spectrum as a Function of Chi-Square per Degrees of Freedom	130
5.5	Thermal Bremsstrahlung, Charge Exchange, and Non Thermal Bremsstrahlung components of the Cas A Spectrum	131
5.6	Charge Exchange Cross Sections Calculated for 17 MeV/ Nucleon Fe Nuclei Impinging on Interstellar Matter	132
5.7	Comparison of Observed Probability Distributions in 104.9 sec Fourier Analyses of Cyg X-1 with That Expected from Random Data. The Contributions to the Oscillations of the Gondola have been removed	133
5.8	Cyg X-3 Observations During 696-P	134

LIST OF FIGURES

Figure		Page
3.1	Three-dimensional view of a multilayer multianode X-ray proportional counter, typical of the ones used in these experiments. The cutaway shows the geometry of the cells under the thin window and collimator	136
3.2	Side view of balloon borne multilayer multianode proportional counter showing location and wiring of cells under the window and collimator. Alternate cells in this detector are coded "A" and "B".	137
3.3	X-ray proportional counter front-end electronics with the wiring of the cells, pulse transformers, and pre-amplifiers shown, for the rocket experiments.	138
3.4	Block diagram of the electronics system used for the balloon and rocket experiments.	139
3.5	Distribution of characteristic photons leaving a cell (resonance escape) and remaining in the same cell for the K- and L-shell in the balloon experiment as a function of depth (layer).	140
3.6	Observed and computed response of layer 1 of the balloon experiment to the laboratory calibration sources Am^{241} , Cd^{109} , Ba^{133} , and Pm^{145}	141
3.7	Fractions of characteristic photons leaving the detector (resonance escape, RE) and remaining in the same cell (SC) for the rocket experiment. The data presented are (A) K-Shell RE for layer 2, detector A, (B) K-RE for 3A, (C) K-RE for 1B, (D) K-RE for 2B and 3B, (E) L-SC for all layers, (F) L-RE for 1B and 2A, (G) K-SC for all layers, (H) L-RE for 3A, (I) L-RE for 2B and 3B.	142
3.8	Computed electron anticoincidence coefficient as a function of energy for the rocket experiment	143
3.9	X-ray energy vs. channel number (linearity calibration) for layer 2 of the balloon experiment as determined with laboratory calibration sources.	144
3.10	Channel number for Cd^{109} calibration source as a function of count rate.	145

Figure		Page
3.11	Observed widths of lines from calibration sources as a function of energy in layer 2 of the balloon experiment.	146
3.12	Transmission efficiency of the collimator on the balloon and rocket experiments as a function of off-set angle.	147
4.1	Sky scan of sounding rocket experiment 13.009 showing times in seconds at which key milestone were reached .	148
4.2	Aspect solution for sounding rocket experiment 13.009 showing offsets in degrees from the intended targets. The error bars represent statistical errors in the aspect solution only, and do not include systematic errors of $\pm 6.1'$ and $\pm 3.2'$ for the 3° and $1/2^\circ$ detector, respectively.	149
4.3	Observed count rate as a function of time for rocket flight 13.009 for layers B1, A1 and A2.	150
4.4	Sketch of balloon gondola, pointing out relative location of (A) detector in swivel mount, (B) experiment camera, (C) gondola system camera, (D) guidance magnetometer, (E) fine readout magnetometer, (F) elevation drive, (G) inertia wheel, (H) momentum un-loader, (I) electronics and computer storage bin, (J) power supplies and converters, (K) crush pad, and (L) cable to parachute and balloon.	151
4.5	Ephemeris for balloon flight 683-P. Displayed are the latitude, longitude, altitude, and elevation angle of the detector.	152
4.6	Celestial position for balloon flight 683-P. Numbers indicate sequential photos, one 3 second exposure every 78.6 seconds.	153
4.7	Observed count rate as a function of time for balloon flight 683-P. Data corresponds to the 15 to 30 keV energy band.	154
4.8	Typical strip chart recordings from balloon flight 683-P showing the experiment camera on-times, coarse and fine readout magnetometer, and elevation angle used to compute the collimator transmission ef-ficiency.	155

Figure		Page
4.9	Ephemeris for balloon flight 696-P, showing latitude, longitude, elevation angle, and altitude. Altitude is given separately as determined by the Rosemount pressure transducer (R) and the barotransmitter (BT).	156
4.10	Observed count rate in the 20 to 30 keV band vs. time for balloon flight 696-P. Vertical bars in the upper trace represent the aspect solution as determined by the experiment camera; horizontal bars, by the gondola system.	157
5.1	99% confidence upper limits to the pulsed fraction for Cas A and Tycho, based on Cooley-Tukey harmonic analysis and fast-fold analysis.	158
5.2	Observed spectra of Cas A with the 3° and 1/2° detectors of the sounding rocket flight 13.009.	159
5.3	Residual counts after subtracting from the Cas A observed spectrum a computed power law spectrum with an index of 4.35 and a computed exponential spectrum with a temperature of $kT = .83$ keV.	160
5.4	Contours of acceptable χ^2 fits for the Cas A data for cosmic ray power law index vs. the iron low energy cut off.	161
5.5	Observed spectra of Tycho with the 3° and 1/2° detectors of the sounding rocket flight 13.009.	162
5.6	Contours of acceptable χ^2 fits for the Tycho data for cosmic ray power law index vs. the iron low energy cut off.	163
5.7	Inferred incident photon spectra of Cas A.	164
5.8	Inferred incident photon spectra from Tycho.	165
5.9	The charge exchange, non thermal bremsstrahlung, and thermal bremsstrahlung components of the spectrum which best represents Cas A. The numbers on the left side of the figure represent atomic numbers. Non thermal bremsstrahlung contributions are the power laws; charge exchange contributions are the line features.	166
5.10	Electromagnetic spectra of the three supernova remnants, the Crab Nebula, Cas A and Tycho.	167

Figures		Page
5.11	Observed counts in the 13 to 33 keV band per effective exposure for Cyg X-1 during balloon flight 683-P.	168
5.12	Observed energy spectrum (counts per channel) of Cyg X-1 from balloon flight 683-P.	169
5.13	Photon flux (photons/cm ² sec keV) of Cyg X-1 as observed by several experiments.	170
5.14	Upper limits on the duration of a single pulse at a 3 σ level vs. the fractional increase in count rate λ/λ_0 for Cyg X-3 as observed from balloon flight 696-P.	171
5.15	Event word spacing distribution for balloon flight 696-P. Typical error bars for the background data are shown by the vertical bar.	172
5.16	Distribution of number of event words per frame for balloon flight 696-P showing complete agreement between source and background data.	173
5.17	Distribution of events in Scalar II for balloon flight 696 P.	174
5.18	Photon flux (photons/cm ² sec keV) of Cyg X-3 as observed by several experiments.	175
A1	Coordinate system used in star field analysis in the celestial sphere (a) and the plane of the photograph (b).	176

CHAPTER I

INTRODUCTION

A. Electromagnetic Astronomy

Ever since the dawn of civilization, man has been doing optical astronomy. Observations were strictly limited to the 1.7 to 3 ev band, the region of sensitivity of the human eye. Early man did not understand the significance of his observations, but did acquire enough knowledge to make use of the heavens for navigational and religious purposes. Many of our ancestors even documented events in the sky, for example the Chinese, Japanese and American Indian observations of the Crab supernova explosion (Minkowski, 1964; Brandt et al., 1973). Instruments like the telescope helped observers discover many new stellar sources, and in spite of the limited energy range, optical observations have taught man most of what he understands about the universe.

The start of radio astronomy some thirty years ago provided the first major increase in the dynamic range of observations (from 10^{-7} to 10^{-3} ev). Radio waves have been detected from the sun and Jupiter and from stellar objects such as ionized hydrogen clouds, supernova remnants, quasars, radio galaxies, and the galactic arms and center. This list is void of stars, and not surprisingly. The most elaborate radio telescopes have sensitivities of approximately 10^{-28} watts/m²Hz. Large radio flares from the sun produce fluxes of 10^{-15} watts/m²Hz, which makes stars only 3 times more distant than our nearest neighbor visible.

In the early 20's, balloon borne experiments detected very penetrating radiations, much more energetic than could be produced by the sun. This, together with the radio observations suggested huge sources of energy in the universe. In the early 60's, in a sounding rocket experiment designed to observe characteristic X-ray fluorescence lines from the moon, Giaconni et al. (1962) observed a strong source of low energy x-rays from a discrete source, Sco X-1. This is still the strongest x-ray source in the sky. More sounding rocket and balloon borne experiments, and finally satellite borne experiments followed. The original low energy X-ray spectrum (1.5 to 10 kev) was extended up to 100's of kev. Finally, the gamma ray experiments flown on balloons and satellites extended the energy range up to 5×10^3 MeV.

While X-ray and gamma astronomy blossomed, the remaining sections of the electromagnetic spectrum were being observed such that today the electromagnetic spectrum over some 18 orders of magnitude is under observation, from approximately 10^{-8} to 10^{10} eV. X-rays are usually understood to be a result of atomic processes while gamma rays have their origins in nuclear interactions. However, both may be closely related to galactic cosmic rays. Unlike photons however, cosmic ray particles are deflected by magnetic fields, and thus retain little memory of their source. It is beginning to appear that X- and gamma ray astronomy may be observing the effects of cosmic rays as they start on their flight through the universe from the sites of evolving stars, typically supernovae. Thus, indirectly, cosmic rays and energetic photons may some day be understood in one grand order.

B. X-Ray Astronomy

1. Historical Development. Since its recent beginning in 1962, X-ray astronomy has grown very rapidly, partly because the straight forward technology existed to carry out the initial experiments and partly because of the immense implications involved regarding the understanding of the universe. Annual publications of more than 100 papers attest to this rapid growth; papers by Pounds (1970) and Friedman (1973) provide excellent overviews on the subject.

Following the 1962 experiment by American Science and Engineering (Giacconi et al., 1962), the next sounding rocket experiment by the Naval Research Laboratory (Friedman et al., 1965) varified the existence of Sco X-1 and also observed the Crab, the two strongest and most studied sources in X-ray astronomy. In these early experiments positional uncertainties made comparisons with optical objects difficult and little information on energy spectra was produced.

To overcome the lack of positional uncertainty, the MIT group (Bradt et al., 1968) made use of modulation collimators (where the transmission efficiency has several maxima and minima) to provide accurate source locations resulting in the identification of optical and radio counterparts for Sco X-1 and the Crab. Many of the sounding rocket experiments made sky scans to detect new sources. These were complimented by balloon borne experiments, typically those of Boldt et al. (1968), Riegler (1969), Lewin et al. (1968), and Overbeck and Tananbaum (1968). Furthermore, it was becoming accepted knowledge that some X-ray sources show extreme variability from one observation to the next. At this time too, energy spectra were beginning to be measured for the first time, and sources were beginning to be categor-

ized according to type.

The OSO-3 satellite was the first permanent platform outside the earth's atmosphere carrying an X-ray experiment, a large field of view scintillation crystal from the University of California, San Diego. Early measurements were restricted to observations of the diffuse x-ray background (Schwartz et al., 1970) but later, discrete source observations were possible (Peterson, 1970 ; Hudson et al., 1971). Sounding rocket and balloon experiments continued, with the development that most of the observed sources were on the galactic disk.

While it was clear that some X-ray sources showed great degrees of variability, this information was based on observations months apart and said nothing about the rate of variability. In 1969, it was found that roughly 10% of the emission from the Crab Nebula was pulsed with a period of 33 milliseconds. Reanalysis of the data obtained from the Crab before this time by other investigators confirmed this observation, complimenting the pulsed radio and optical emission, detected two year previous. This high frequency requires a neutron star core in the remnant, an idea first proposed by Oppenheimer and Volkoff (1939).

The radio and optical emission from the Crab was found to be polarized. After several sounding rocket observations, Novick et al. (1972) found the X-rays in the 5 to 20 keV band to also show polarization.

The most recent and certainly most important event in X-ray astronomy was the launch of the SAS-A, or UHURU, satellite by the ASE group in late 1970. This small satellite devoted solely to the study of the non-solar X-rays has made many surprising discoveries. The latest UHURU catalogue of the X-ray sky (Giacconi et al., 1973) lists only 161 sources down to a limiting sensitivity of 2.5×10^{-11} ergs/cm²sec

for a nearly complete sky coverage. Pre-UHURU observations suggested possibly 1000 X-ray objects, based on the expected number intensity distribution. Many pulsating X-ray sources have been decoded, such as Her X-1 (Tananbaum et al., 1972) with 1.24 second, 1.7 day, and 36 day periods. Error boxes defining source locations have been used to locate radio and optical counterparts; long term temporal variations and energy spectra are still being studied.

In spite of the success of the UHURU satellite sounding rocket and balloon programs continued and will so in the near future. The satellite provided for continuous and repeated observations with the same instrument, but this early experiment was necessarily simple, with a small energy band, low data rate, and low energy resolution. Furthermore, the satellite requires spin stabilization and cannot be readily pointed at any star in the sky.

The future holds bright prospects for X-ray astronomy. The OSO-I satellite will contain two experiments from NASA-GSFC, and one each from the University of Wisconsin and Columbia University. The revised HEAO program will again have a single satellite devoted entirely to X-ray astronomy, as will the smaller SAS-C and UK-5.

2. Present Understanding of X-Ray Astronomy. X-Ray objects can be classified into 4 categories. The first of these are the thermal sources, of which Sco X-1 and Cyg X-2 are examples. They are characterized by exponential spectra with temperatures of the order of 5×10^7 °K. Long term variations in intensity occur in both the hard and soft x-ray regions while not in the radio or optical, suggesting a two component model for the source. In addition, for Sco X-1, there exists a

flickering in the optical on time scales of minutes to hours which is correlated with fluctuations in the hard X-ray band, the low energy X-ray intensity remaining unchanged.

A second class of X-ray objects is that of supernova remnants, a good summary of which has been given by Woltjer (1972). At the end of its life, a star will burn out and become either a white dwarf or a supernova. In the later, as nuclear burning of the lighter elements causes the star to collapse, the intruding matter generates an instability which causes either all of the matter to be blown out into space, or a fraction thereof, in which case the inner layers go into a neutron star or black hole, depending on the initial size of the star. The Crab nebula is a supernova remnant, with the nebula region corresponding to the matter ejected in the explosion. The slow-down in the frequency of the 33 millisecond pulsar is believed to be the source of the 10^{37} ergs/sec being radiated. From the high frequency pulsations, a neutron star core with extremely strong magnetic fields is inferred. Unfortunately, of approximately 60 radio pulsars, only the Crab and Vela X-1 have been observed to pulse in the X-ray region. Yet, there are many known supernova remnants, typically Tycho (year 1572), Puppis A, Cygnus Loop, and Cas A (year ~1667). All of these sources exhibit filaments and/or shells of expanding gas and strong polarizations in the radio band. With the lack of a pulsar, information as to the nature of the supernova remnants must come from spectra. But this information is limited as none of the supernova remnants has been observed in the hard X-ray region with the exception of the Crab.

The third class of X-ray objects is that of binary systems, of

which Cen X-3, Her X-1, Cyg X-3, and Cyg X-1 are typical. In the case of Cen X-3, Her X-1, and Cyg X-3, periodicities of 2.1, 1.7, and 0.5 days, respectively, have been observed in the x-ray region. For Cyg X-1, a simultaneous transition in the low energy X-ray intensity and the intensity of a radio star in the X-ray error box fixed the position which is coincident with a spectroscopic binary with a 5.6 day period. No period of this type has been observed in the hard or soft X-ray band. Most of these objects show strong low energy absorption, and are subject to extreme fluctuations in intensity. These fluctuations are typically believed to be due to having one of the members of the binary pair being a black hole. This black hole will accrete matter from the companion star through the Lagrangian point of the Roche surface, but not in a continuous stream. The infalling matter onto the black hole would then be the source of copious X-ray emission at the observed random times.

Of the 161 presently known X-ray sources, all of the stronger sources (with flux $\geq 7.5 \times 10^{-10}$ erg/cm²sec) with the exception of Sco X-1 and Her X-1 lie within 15° of the galactic plane suggesting that these sources belong to our own galaxy. Examination of the luminosity vs. number distribution of the remaining sources suggests that a large number of weaker sources are of extragalactic origin (Matilsky et al., 1973), and thus, the possible last type of X-ray source, extra galactic objects. Most of these extra-galactic objects are typically radio galaxies (M-87, Cen A, Perseus A), seyfert galaxies (typically NGC 4151), quasars (typically 3C273), and clusters of galaxies (typically the Coma cluster). Many of the radio galaxies have dense active cores and jets suggesting violent explosions in the past, and have shown great

variability in both flux and spectrum. Seyferts and quasars may possibly be regions of active galactic formation as radio observations show large amounts of matter streaming at high velocities. For clusters of galaxies, the expected emission of X-rays from the summation over all galaxies is less than observed, suggesting a hot intercluster gas.

3. Purpose of this Study. The purpose of this thesis is to report on several observations, each observation pointing out the wide diversity in X-ray astronomy.

The first experiment was conducted to observe low energy X-rays from the supernova remnants Cas A and Tycho via a sounding rocket platform. Cas A is by far the strongest apparent radio source in the sky (Peimbert and van den Bergh, 1971) and yet is one of the weakest X-ray emitters. By examining the gaseous nebula around Cas A, van den Bergh and Dodd (1970) established an approximate date of 1667 for the supernova, and it is believed to be at a distance of 2.8 kpc (van den Bergh, 1971). Searle (1971) reports a faint HII region associated with Cas A, suggesting ionization due to emissions from the original supernova.

Cas A was first observed by Friedman et al. (1967) who found that the low energy X-ray spectrum could be fit, within statistics, by either a power law of $E^{-2.1}$ or an exponential of $kT = 1.3$ keV. A second observation by Gorenstein et al. (1970) gave a flux in the 1 to 10 keV band of $2 \text{ keV/cm}^2\text{sec}$, and pointed out that simple models would not fit the data. Giaconni et al. (1971) further verified the existence of Cas A as an X-ray emitter. The questions to be answered are; what is the energy spectrum and are there any periodic

fluctuations as in the Crab? Due to the uncertainties in the previous spectral studies, all that was clearly established was the existence of Cas A.

The same questions must be asked of Tycho, a second supernova remnant which is even weaker in the soft X-ray band. Unlike Cas A, Tycho is a weak radio source but like Cas A, it is strongly polarized. Radio maps show an almost circular shell (Baldwin, 1967) and optical studies of filaments in the shell show a rapidly expanding nebular region (van den Bergh, 1971). The distance to Tycho is taken to be 3 kpc.

Previous X-ray observations are similar to those of Cas A, a rocket observation by Friedman et al. (1967) suggesting a power law fit of $E^{-1.3}$ or an exponential fit with $kT = 2.7$ keV, with large uncertainties. Gorenstein et al. (1970) obtained a 1 to 10 keV flux of about $0.8 \text{ keV/cm}^2\text{sec}$ which was verified by Giaconni et al. (1971).

Sounding rocket borne experiments have durations of at most 250 seconds, making them impossible platforms for the study of long term temporal variations; balloon experiments can usually remain at ceiling for at least 6 hours. The peculiar behavior of Cyg X-1 makes it a likely source for observation at any time, in spite of the vast amounts of data already collected. The low energy X-ray observations of Gorenstein et al. (1967), Bleach et al. (1972), Meekins et al. (1969), and MacGregor et al. (1969) and the hard X-ray observations of Haymes and Harnden (1970) and Matteson (1971) suggest a power law of $E^{-1.8}$ from approximately 2 to 180 keV. However, this is not the complete picture. While the low energy X-ray region shows long term stability, the hard X-ray intensity varies by orders of magnitude (Overbeck and

Tananbaum, 1968; Matteson, 1971) so as to be characterized by a low state and high state (consistent with the $E^{-1.8}$ power law). These transitions take place on the time scales of days. While the overall intensity in the low energy X-ray region remains approximately the same, it is characterized by quasi periodic fluctuations (Oda et al. 1971 ; Holt et al. 1971) ranging from 100 milliseconds to seconds. Still a third variation is the 5.6 day periodicity in the optical counterpart of Cyg X-1 (Bolton, 1972; Webster and Murdin, 1972). Consequently it is of interest to extend the measurements of Bleach et al. (1972) using essentially the same type of experiment, a balloon borne multilayer multianode proportional counter, sensitive up to 80 keV.

A second peculiar object, Cyg X-3, has many features similar to Cyg X-1, particularly the long term fluctuations in the hard X-ray region. A weak radio source (just above the limits of detectability with the interferometer of the National Radio Astronomy Observatory) in the error box of the Uhuru **location** has been identified by Braes and Miley (1971) and exhibits many flare like increases in intensity by a factor of 2 to 4 (Hjellming et al., 1972). Simultaneous fluctuations in the radio and X-ray have yet to be observed. A previous observation by Bleach et al. (1972) in the low energy X-ray region and consistent with the low energy X-ray observations of MacGregor et al. (1970) indicates strong absorption in the source at low energies (possibly an optically thick source). The Bleach et al. (1972) observation was not able to distinguish between a power law or thermal model for the source. The hard X-ray data of Peterson (1970), Rocchia et al. (1969) in two flights, and Matteson (1971) show variations in intensity

of over an order of magnitude. If the data reported by Bleach et al. (1972) in the 2 to 10 keV band were to be extrapolated to the hard X-ray region, the various observations would fall above the Bleach et al. (1972) observation. Yet, this observation had a few statistically significant data points (Holt, 1972) above 10 keV which suggest a strong high energy component. Again, a search for temporal fluctuations is appropriate. As radio and X-ray intensity had not yet been correlated, the experiment was done in conjunction with the National Radio Astronomy Observatory.

Both of the balloon experiments were conducted with a 4° FWHM collimator. Previous experiments were consistently done with large angle telescopes thus generating source confusion, particularly in regions like Cygnus where several X-ray sources are in close proximity. In the case of the rocket observations, 3° and $1/2^\circ$ FWHM collimators were used. Here, however, source confusion is not the problem, but the diffuse X-ray background contributes strongly and reduces the significance of the data. The $1/2^\circ$ detector required pointing accuracy which represented the state-of-the-art in sounding rocket control as there were no error signals from the experiment to guide the pointing.

The following chapter discusses mechanisms for the production of X-rays. Chapter III describes the experiments and pertinent electronics, mechanisms for the interactions of X-rays within the detectors, and timing logic. The flight systems and individual launches are discussed in Chapter IV. The last chapter outlines the data analysis procedure, both spectral and temporal, and presents the results with a discussion for each of the sources observed. The technique for determining the aspect solution of the detectors is discussed in the Appendix.

CHAPTER II

MECHANISMS FOR THE PRODUCTION OF X-RAYS

A. General Discussion

In the astrophysical context X-ray production mechanisms usually fall into the realm of atomic physics, and are classified as either non thermal or thermal in nature. The two principle non thermal processes, synchrotron radiation and inverse Compton scattering, yield a power law photon spectrum while the thermal emission is usually characterized by an exponential spectrum. Details of these mechanisms have been discussed by numerous authors, typically Hayakawa and Matsuoka (1964), Ginzburg and Syrovatskii (1964), Tucker (1967), and Blumenthal and Gould (1970). The following is a brief summary of the most important features of these processes.

B. Non Thermal Processes

1. Synchrotron Radiation. An ultrarelativistic electron of energy $E = \gamma mc^2$ spiraling in a magnetic field B will lose energy by synchrotron radiation at a rate

$$-\frac{dE}{dt} = \frac{\sigma_0}{4\pi c} \gamma^2 B^2 v^2 \sin^2 \delta, \quad (2.1)$$

where

σ_0 = Thomson cross section = $6.65 \times 10^{-25} \text{cm}^2$,

c = speed of light,

m = electron rest mass,

$$\gamma = [1 - (v/c)^2]^{-1/2},$$

v = electron velocity,

δ = pitch angle.

For a randomly oriented field B in units of gauss and $v \approx c$, the energy loss in ergs/sec is

$$-\frac{dE}{dt} = 1.06 \times 10^{-15} B^2 \gamma^2, \quad (2.2)$$

with a characteristic lifetime for the electron of

$$\tau = \left[\frac{1}{E} \frac{dE}{dt} \right]^{-1} = \frac{6\pi}{B^2} \frac{mc}{\sigma_0 \gamma} = \frac{7.74 \times 10^3}{B^2 \gamma} \text{ sec.} \quad (2.3)$$

In the vicinity of neutron stars or black holes where fields of the order of 10^6 gauss are believed to exist, the electron population must be continuously replenished with energy as the lifetimes predicted would thus rule out such models for typically the Crab supernova remnant.

The spectrum generated by a synchrotron electron is strongly peaked around a critical frequency

$$\nu_c = \frac{3e B \gamma^2}{4\pi mc} = 4.20 \times 10^6 B \gamma^2, \quad (2.4)$$

allowing the spectrum to be approximated by a delta function

$$\frac{d}{dh\nu} \left(\frac{dE}{dt} \right) = \frac{dE}{dt} \left\{ \delta(h\nu - \langle h\nu \rangle) \right\}, \quad (2.5)$$

where $\langle h\nu \rangle$ is the mean photon energy of frequency $\nu = \nu_c$ of Equation 2.4. Assuming a power law spectrum for the initial distribution of electrons,

$$\frac{d}{dE} \left(\frac{dN}{dV} \right) = A E^{-T} \quad (2.6)$$

the observed photon spectrum

$$\frac{dq}{dh\nu} = \frac{1}{h\nu} \int_{h\nu}^{\infty} \frac{d}{dh\nu} \left(\frac{dE}{dt} \right) \frac{d}{dE} \left(\frac{dN}{d\nu} \right) dE \quad (2.7)$$

becomes

$$\frac{dq}{dh\nu} = \frac{\sigma_0 A c B^2}{12\pi (mc^2)^2} \left[\frac{\langle h\nu \rangle}{(\gamma mc^2)^2} \right]^{\frac{T-3}{2}} (h\nu)^{-\left(\frac{T+1}{2}\right)} \quad (2.8)$$

or

$$\frac{dq}{dh\nu} \propto (h\nu)^{-\left(\frac{T+1}{2}\right)} \quad (2.9)$$

The unique feature of synchrotron radiation is that the beam of photons is polarized. The polarization at an observation angle θ with respect to the magnetic field is

$$P(\theta) = \left\{ \left(\frac{dq}{dh\nu} \right)_{\parallel} - \left(\frac{dq}{dh\nu} \right)_{\perp} \right\} / \left\{ \left(\frac{dq}{dh\nu} \right)_{\parallel} + \left(\frac{dq}{dh\nu} \right)_{\perp} \right\} \quad (2.10)$$

Integrating over all frequencies, the intensities with polarization parallel and perpendicular to the orbital plane are (Jackson, 1965)

$$\left(\frac{dq}{dh\nu} \right) = k \quad (2.11)$$

and

$$\left(\frac{dq}{dh\nu} \right) = k \frac{5}{7} \frac{(\pi/2 - \theta)^2}{(1/\gamma)^2 + (\pi/2 - \theta)^2} \quad (2.12)$$

where k is a constant, such that

$$P(\theta) = \frac{1 + \frac{2}{7} \gamma^2 (\pi/2 - \theta)^2}{1 + \frac{12}{7} \gamma^2 (\pi/2 - \theta)^2} \quad (2.13)$$

Consequently, an observer perpendicular to the magnetic field will see 100% polarization.

2. Inverse Compton Scattering. A power law X-ray spectrum can also be produced by the inverse Compton process, in which ultrarelativistic electrons collide with low energy photons (typically the 3° blackbody photons) and impart energy to the photon. In the Thomson limit, where the initial photon energy is much smaller than the rest energy of the electron, the cross section for interaction is σ_0 . The mean energy $\langle h\nu_0 \rangle$ of photons is increased to

$$\langle h\nu_f \rangle = \frac{4}{3} \gamma^2 \langle h\nu_0 \rangle, \quad (2.14)$$

and the energy loss rate for the electrons is

$$-\frac{dE}{dt} = \langle h\nu_f \rangle \frac{dN}{dt} = \frac{4}{3} \gamma^2 \sigma_0 c \rho = 2.66 \times 10^{-14} \rho \gamma^2, \quad (2.15)$$

where

$$\begin{aligned} \rho &= \text{energy density of the target photon field,} \\ \frac{dN}{dt} &= \text{collision rate.} \end{aligned}$$

The characteristic lifetime here is

$$\tau = \frac{3mc}{4\sigma_0 \rho \gamma} = \frac{3.08 \times 10^7}{\rho \gamma} \quad (2.16)$$

Approximating the spectrum of a monoenergetic electron source by a δ function, as in Equation 2.5, and using the source function of Equation 2.6, a power law electron spectrum, the differential photon energy spectrum becomes

$$\frac{dq}{dh\nu} = \frac{2\sigma_0 A c \rho}{3(mc^2)^2} \left[\frac{4\langle h\nu_f \rangle}{3(mc^2)^2} \right]^{\frac{\Gamma-3}{2}} (h\nu)^{-\left(\frac{\Gamma+1}{2}\right)} \quad (2.17)$$

or

$$\frac{dq}{dh\nu} \propto (h\nu)^{-\left(\frac{\Gamma+1}{2}\right)}, \quad (2.18)$$

the same power law spectrum as observed from synchrotron radiation.

3. Nuclear Processes. Nuclear processes can account directly for gamma-ray production and only indirectly for X-ray production by the decay of radioisotopes in remnants of nuclear burning. In the astrophysical concept, supernovae are understood to be sites of the r- process type of nuclear burning discussed by Burbidge et al. (1957). The r- process (called the rapid process because high Z neutron rich elements are produced by adding neutrons more rapidly than the products can undergo beta decay) generates transbismuth elements of which Am^{241} is typical (Clayton and Craddock, 1965) and which produces the strongest low energy line at 60 keV. Hoyle and Fowler (1960) suggest that the Crab nebula was site of an r- process and Jacobson (1968) observed the Crab nebula and was able to set upper limits on line emission at 60 keV at a level of 1.4×10^{-3} photons/cm² sec, well within the sensitivity of the present experiments. To date, there has been no verification of the 60 keV line.

4. Non Thermal Bremsstrahlung. In the mechanism of non thermal bremsstrahlung or proton inner bremsstrahlung as discussed by Hayakawa and Matsuoka (1964) and more recently by Boldt and Serlemitsos (1969), a low energy cosmic ray proton scatters an ambient electron, either bound or free, such that in the rest frame of the proton, the interaction is simply that of an electron moving through and being deflected by the field of a proton. The radiation $h\nu$ due to the Coulomb scattering interaction between an electron and a cosmic ray nucleus of charge Z in the rest frame of the cosmic ray nucleus is given by the

Bethe-Heitler cross section (Heitler, 1954) as

$$h\nu \frac{d\sigma}{dh\nu} = \frac{\alpha}{\pi} \sigma_0 \left(\frac{mc^2}{T_0} \right) Z^2 \ln \left\{ \frac{1}{h\nu} \left[T_0^{\frac{1}{2}} + (T_0 - h\nu)^{\frac{1}{2}} \right]^2 \right\}, \quad (2.19)$$

where

α = fine structure constant = $1/137$,

T_0 = electron kinetic energy, in the nucleus rest system before the collision.

In transforming to the rest frame of the electron, and assuming non relativistic kinematics,

$$T_0 = \frac{m}{M} E, \quad (2.20)$$

where

M = nucleon mass,

E = cosmic ray particle energy/nucleon.

The differential cosmic ray bremsstrahlung energy spectrum (photons/cm³sec erg) may then be written as

$$\frac{dq}{dh\nu} = n_e \int_{\frac{Mh\nu}{m}}^{\infty} \frac{d\sigma}{dh\nu} \beta c N(E) dE \quad (2.21)$$

where

n_e = ambient electron number density

$N(E)$ = spectral number density of cosmic ray nuclei (protons/cm³erg) with velocity βc .

Assuming a power law spectrum for the energetic nuclei,

$$J(E) = A E^{-\ell} = \frac{1}{4\pi} \beta c N(E), \quad (2.22)$$

one obtains

$$\frac{dq}{dh\nu} = 8 n_e \alpha Z^2 \sigma_0 A \frac{Mc^2}{h\nu} \left(\frac{m}{M h\nu} \right)^{\ell} f(\ell), \quad (2.23)$$

in units of (photons/cm³sec keV), where $S(l) \approx l^{-1.6}$ for $0.5 \leq l \leq 5.0$.

The rate of energy loss given by Rossi (1952) for the Coulomb scattering is

$$-\frac{dE}{dx} = \frac{3}{4} \sigma_0 m_e m c^2 \left(\frac{M c^2}{E} \right) \frac{Z}{A} \left\{ \ln \frac{4 m E}{M V_0} - \frac{Z E}{M c^2} \right\}, \quad (2.24)$$

where

E = total kinetic energy of the cosmic ray nuclei,

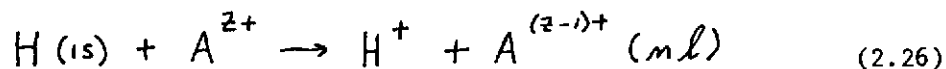
V_0 = ionization potential of target with atomic weight A .

The lifetime of energetic nuclei can be expressed as

$$T = \int_{E_0}^{\infty} \left(\frac{M}{2E} \right)^{1/2} \left(\frac{dE}{dx} \right)^{-1} dE \quad (2.25)$$

where E_0 is the initial energy. A 20MeV proton traversing the interstellar medium will thus have a lifetime of typically 4×10^{12} seconds.

5. Charge Exchange. The charge exchange process also makes use of low energy cosmic ray nuclei for the production of X-rays. Silk and Steigman (1969) propose that in the encounter with hydrogen atoms in HI regions, low energy cosmic ray nuclei can capture an electron by the charge-exchange process,



If the capture is into states of principle quantum number 2 or greater, the excited cosmic ray particle will decay to the ground state emitting characteristic photons. For capture into the 2p state, a characteristic Lyman α line will result; for the 3p state, Lyman β ; etc.

As the cross sections for electron capture fall off rapidly with energy, and since the line emission will be Doppler broadened due to

the isotropic distribution of the cosmic ray particles, this mechanism will allow a determination of the spectrum and low energy cutoff of the initial cosmic ray spectrum.

Silk and Steigman limited their calculations to the galactic plane where they predict appreciable line intensities. In the case of supernova remnants where large fractions of matter were ejected, the same mechanism will yield X-rays in the region where the expelled gas interacts with the interstellar medium. As fluxes are orders of magnitude greater for this case, strong line intensities are expected.

While previous models and the thermal processes take place at the site of the star, a point source, this mechanism could account for an X-ray halo around the central object which could be separated by great distances.

More details of this mechanism will be presented in Chapter V.

C. Thermal Processes

1. Blackbody Radiation. Bodies with any temperature with emit photons due to the thermal agitation within them, these photons being termed thermal radiation. The simplest case is that of a blackbody, where the photonic field is in equilibrium with matter, the differential photon density (photons/cm³) being given as (Aller, 1963)

$$\frac{dq}{dh\nu} = \frac{8\pi\nu^3}{c^3} (e^{h\nu/kT} - 1)^{-1}, \quad (2.27)$$

where

ν = photon frequency,

h = Planck constant = 4.135×10^{-15} eV-sec,

k = Boltzman constant = $.861 \times 10^{-4}$ eV/°K,

T = temperature of the gas.

This blackbody radiation expression is used to describe the 3° universal background radiation believed to represent a "ringing" of the universe in the proposed "big bang" theory, but has not yet been used to describe emission from X-ray stars, as in the latter case, the X-ray star is not in equilibrium with the "vacuum" which surrounds it. Only in cases where the thermal energy content is much larger than that emitted can an approximation to the blackbody idea be made.

2. Optically-Thin Thermal Bremsstrahlung. Unlike the opaque (optically infinitely thick) nature of blackbody sources, optically-thin source models contain the assumption that none of the generated photons interact with the thermal medium. In the case of thermal bremsstrahlung, the electrons required for X-ray production are of energies slightly greater than the photon energies, allowing consideration of non relativistic electron distributions.

Collisional losses are typically $\sim 10^4$ greater than radiative losses (Berger and Seltzer, 1964), but need not be considered as all collisional energy is returned to the plasma. Any initial electron energy spectrum is thus rapidly thermalized to a Maxwellian distribution.

Non relativistic electrons in Coulomb collisions will lose energy via radiation at a rate (Heitler, 1954)

$$-\frac{dE}{dt} = \frac{32\pi}{3} \frac{z^2 e^6}{hmc^2} \beta m_0 = 7.58 \times 10^{-23} z^2 \beta m_0, \quad (2.28)$$

where

m_0 = number of target nuclei,

Z = charge of target nuclei,

e = electronic charge = 1.6×10^{19} coul.

Assuming a power law distribution of electrons as in Equation 2.6, the differential photon energy spectrum again becomes a power law of the form

$$\frac{dq}{dh\nu} \propto (h\nu)^{-(T+1/2)}, \quad (2.29)$$

but this is not expected to be characteristic due to the thermalization of the initial electron population.

Assuming a Maxwellian distribution,

$$\frac{d}{dE} \left(\frac{dN}{dV} \right) = \frac{2 m_e}{(kT)^{3/2}} \sqrt{\frac{E}{\pi}} e^{-E/kT}, \quad (2.30)$$

where m_e is the total electron density, the differential photon energy spectrum (photons/cm³sec keV) becomes (Fucker and Gould, 1966)

$$\frac{dq}{dh\nu} = m_e m_Z \frac{64\pi Z^2 e^6}{3h(mc^2)^2} \left(\frac{\pi mc^2}{6kT} \right)^{1/2} \frac{g(\nu, T)}{h\nu} e^{-h\nu/kT} \quad (2.31)$$

where $g(\nu, T)$ is the averaged free-free Gaunt factor of Karzas and Latter (1961), where

m_Z = density of ions of charge Z ,

$$g(\nu, T) \approx \frac{\sqrt{3}}{\pi} \ln \frac{4kT}{T h\nu}, \quad h\nu \ll kT, \quad (2.32)$$

$$= 1, \quad h\nu \gg kT, \quad (2.33)$$

and $\ln T = 577$. To compute the total radiation, one must average over all values of Z . Bremsstrahlung is expected to dominate the emission above approximately 5×10^6 K.

3. Optically-Thin Radiative Recombination: The second component to the thermal radiation from a hot plasma is due to radiative recombination. In the hydrogenic approximation of Elwert (1954) and a Maxwellian distribution of electron velocities, the differential photon energy spectrum for captures of electrons into states of principle quantum number m of ion of charge Z is

$$\frac{dq}{dh\nu} = m_e m_z \frac{4A I_H^2 Z^4 c}{(mc^2)^2 m^3 \nu} \left(\frac{\bar{f}_m}{2m^2} \right)^2 \left(\frac{mc^2}{2\pi kT} \right)^{3/2} e^{(I_{zm} - h\nu)/kT} \quad (2.34)$$

where

$$\frac{\bar{f}_m}{2m^2} = \text{incompleted fraction of shell } m,$$

$$A = 2.11 \times 10^{-22} \text{ cm}^2$$

$$I_H = \text{ionization potential of the hydrogen state } m,$$

$$I_{zm} = \text{ionization potential of the } Z \text{ ion state } m.$$

At high temperatures, most of the recombinations will be captures by bare ions of $Z \geq 6$.

Dielectronic recombination will also occur, but requires capture into ions which have at least one or more orbital electrons, and will consequently contribute at lower temperatures.

4. Optically-Thin Line Emission: Thermal radiation from a hot plasma will also produce line emission, resulting from inelastic electron collisions in which discrete levels of ions are excited. Again using a Maxwellian electron velocity distribution, the number of photons (photons/cm³sec) in a particular line of energy $E_{mm'}$ corresponding to the n - n' transition is

$$\frac{dq}{dt dV} = m_e m_o 8\pi^2 e^4 f_{mm'} \langle \bar{g}_{mm'} \rangle (6\pi m kT)^{-1/2} \frac{1}{E_{mm'}} e^{-E_{mm'}/kT} \quad (2.35)$$

where

$f_{mm'}$ = dipole oscillator strength for the n - n' transition,
 $\langle \bar{g}_{mm'} \rangle$ = averaged constant Gaunt factor, values of which are
 given by van Reyemorter (1962),

Line emission will dominate for temperatures below approximately
 5×10^6 K but rapidly decreases and falls an order of magnitude below
 the Bremsstrahlung component at roughly 10^7 K (Tucker and Gould, 1966)

5. Power Emitted from Optically-Thin Sources: The total free-free (bremsstrahlung) power emitted in units (ergs/cm³sec) is

$$P = \int_0^{h\nu} h\nu \frac{d\epsilon}{dh\nu} dh\nu \quad (2.36)$$

Substituting Equation 2.31,

$$P_B = m_e m_z \frac{64\pi z^2 e^6}{3 h m c^2} \left(\frac{\pi kT}{6 m c^2} \right)^{1/2} = 1.21 \times 10^{-19} z^2 m_e m_z \sqrt{kT} \quad (2.37)$$

for $h\nu \gg kT$ and kT in ergs. The total power emitted in a particular line is

$$\begin{aligned} P_L &= m_e m_o \frac{8\pi^2 e^4 f_{mm'} \langle \bar{g}_{mm'} \rangle}{(6\pi m kT)^{1/2}} e^{-E_{mm'}/kT} \\ &= 3.21 \times 10^{-23} (kT)^{-1/2} m_e m_o f_{mm'} \langle \bar{g}_{mm'} \rangle e^{-E_{mm'}/kT}, \end{aligned} \quad (2.38)$$

where kT is in ergs. As the thermal energy density in the source is

$$u = m_e kT, \quad (2.39)$$

the ratios of Equation 2.39 to Equations 2.37 and 2.38 will give a measure of the thermal lifetime.

6. Optically-Thick Thermal Radiation: Between the two extremes of infinite optical depth (blackbody) and zero optical depth (optically-thin sources) lies reality. In optically-thick plasmas, characteristic lines are affected most severely. Photoionization in the clouds raises the states of ionization equilibrium adding more lines and reducing the strengths of the existing lines. Characteristic photons are also removed from the beam by Thomson scattering the resonance scattering. Felten et al. (1972) predict that for typical optical thicknesses of $\tau \approx 10$, reductions of line intensities of 1 to 2 orders of magnitude occur for temperatures in the range from 10^7 to 10^8 K, along with line broadenings by factors of 2 or more orders of magnitude.

CHAPTER III

DESCRIPTION OF THE INSTRUMENTS

A. Proportional Counters

Examination of the cross sections for X-rays interacting with matter shows that in the .1 to 100 keV band the dominant mechanism is the photoelectric effect. Consequently, observations of X-rays become observations of the photoelectron and photons generated in the decay to ground state of the excited atoms. Solid state detectors, proportional counters, and scintillator-photomultiplier counters are used to collect the charge due to ionization produced by the photoelectron and characteristic photons directly, by internal multiplication, or by converting the energy back into visible light, respectively.

In all cases, the energy resolution is strictly limited by the statistical uncertainty in the number of ion pairs created. For a proportional counter, if E is the energy of an electron, the number of ion pairs formed is typically

$$N_i(E) = E/30\text{eV} . \quad (3.1)$$

The inherent resolution of a detector can be represented by a standard deviation (Holt, 1970)

$$\sigma(E) = N_e(E)^{1/2} = [ME/30\text{eV}]^{1/2} , \quad (3.2)$$

where M is the multiplication factor, or inherent gain. The energy resolution (full width at half maximum divided by the energy) is then given by

$$R_{FWHM} = 2.35 \frac{\sigma(E)}{N_c(E)} = 2.35 [ME/30eV]^{-1/2} \quad (3.3)$$

For proportional counters, gains are typically of the order of 10^3 such that resolutions of 10^{-1} are possible. Solid state detectors operate at a few percent resolution while scintillation devices frequently have 30 to 40 percent resolution.

Proportional counters are just one class of gaseous radiation detectors, these devices usually being configured as a grounded cylinder with an anode through the center. In ionization chambers, the voltage on the anode is high enough to just collect all the ion pairs without producing any multiplication; in Geiger-Müller counters, the voltage is so high that after a few ion pairs have been formed, complete breakdown occurs generating a large and easily detectable signal (Melissinos, 1966). In the medium between these two, the voltage is such that the number of collected ion pairs is proportional to the initial number generated.

Detector geometry plays an important role in proportional counters as the charge must be collected before it recombines and also within the integration time of the associated electronics. To eliminate this factor, proportional counters are seldom more than 1 to 2 cm in diameter. Furthermore, for observations of low energy photons, the gas container cannot be more than .002 gms/cm² before a prohibitive amount of absorption occurs. Also, large areas are required to observe statistically significant amounts of photons in times consistent with flight durations. This problem has been solved by the X-Ray Group of NASA Goddard Space Flight Center by the construction of multilayer

multianode proportional counters, where a cell is defined as an anode typically 30 to 50 cm long surrounded by ground plane wires in a square array, each wire being approximately .3 cm from the next. Figure 3.1 shows such an array of cells, typical of the rocket borne detectors. The gas is confined in the detector by a thin window supported under the collimator. Figure 3.2 displays the balloon borne detector, with the line of sight parallel to the wires.

A problem unique to the proportional counters is that of resonance escape, the departure of a characteristic photon from the detector. Consequently, observed spectra from a monochromatic X-ray beam will show a peak for the energy of the photon, plus a peak for this energy less the energy of the characteristic line. Compton interactions will contribute insignificantly to the spectrum and are considered as part of the background.

B. Detector Description

1. Detector Logic. To eliminate the background due to charged particles, the side and bottom cells of the detectors have their anodes wired in parallel and in anticoincidence with the remainder of the detector. Alternate cells of each layer are also wired in parallel, as shown in Figure 3.2 for the balloon detector. The two signals from each layer are broken up into an analog pulse and two logic pulses (to identify which of the alternate cells fired) via pulse transformers, as sketched in Figure 3.3 for one of the rocket detectors. Simultaneous logic pulses cause a flag to be set in the data word describing the event. Simultaneous pulses in any two layers result in the rejection of the event. A block diagram of the electronics system used in

both the rocket and balloon experiments is presented in Figure 3.4. Further details are described in the manual of Birsa et al. (1972).

2. Rocket Borne Detectors. The rocket experiment consisted of 2 detectors of 4 layers, each layer having 16 cells, each cell being $1/2'' \times 1/2'' \times 18.1/2''$ in size. The "A" ($1/2^\circ$ circular collimation) detector had a 1 mil kapton window on both sides of layer 1 which was filled with .55 atm of helium and .55 atm propane. Thus, layer 1 would act as an anticoincidence shield to low energy electrons passed through or generated in the collimator while at the same time being considerably more transparent than a full layer of xenon gas. The collimator over $1/6$ th of its area was blocked and the 2 cells in each xenon layer beneath this dead area were wired as a separate layer allowing simultaneous source and detector background observations. The remainder of the detector (filled with 1 atm xenon and .1 atm methane) was wired for anticoincidence similar to the balloon detector, as sketched in Figure 3.2.

The "B" (3° circular collimation) detector had a single 1 mil kapton window in front of the first layer, a fill of 1 atm xenon and .1 atm methane, and was wired in the standard manner, also sketched in Figures 3.3 and 3.2.

3. Balloon Borne Detector. The balloon multianode multilayer proportional counter (Figure 3.2) consisted of 8 layers, each layer having 17 cells, each cell being $.75'' \times .75'' \times 12.75''$ in size. The fill gas was 1 atm xenon and .1 atm methane. Beneath the 12 mil aluminum window, the first layer was wired such that coincident pulses in adjacent cells

would be immediately rejected. For layers 2 through 7, coincident pulses in adjacent cells are accepted but flagged in the mark bit of the data word.

C. Energy Calibration

1. Photoelectric Interaction. A photon of energy E incident on the detector will interact via the photoelectric effect, contributions from incoherent and coherent scattering being more than an order of magnitude less even at high energies. The emitted photoelectron will come from the K, L, M, ... shells with probabilities $\alpha_K, \alpha_L, \alpha_M, \dots$. The residual excited atom will relax by fluorescence with probabilities β_K, β_L, \dots , where the energy of the photon is $E_K - E_L, E_L - E_M, \dots$ (Evans, 1955). The remainder of the time, relaxation will be via the Auger effect with probabilities $1 - \beta_K, 1 - \beta_L, \dots$, and with electrons emitted of energy $E_K - 2E_L, E_L - 2E_M, \dots$. The remainder of the energy in the atom is dissipated into the gas via soft X-rays, UV photons, and low energy electrons.

Contributions from the quench gas methane can be ignored as the effective cross sections are at least 4 orders of magnitude less than those for xenon. Grodstein (1957) quotes approximate values for the relative probabilities for absorption in the K, L_I, M_I, ... shells as $\alpha_K = 1/1^3$; $\alpha_{L_I} = 1/2^3$; $\alpha_{M_I} = 1/3^3, \dots$. By observing jumps in the cross sections at the individual shell edges, Storm and Israel (1967), using a combination of the best theoretical and experimental results, give parameters useful in calculating values of α . These computed values are listed in Table 3.1.

Fluorescence yields for xenon are given by Storm and Israel (1967) as $\beta_K = .875$ and $\beta_L = .140$. For the M shell and beyond, fluorescence can be neglected as cross sections are high enough to immediately absorb any characteristic photons.

If a photon interacts via the K shell in xenon, four distinct possibilities exist (Table 3.2). Transition probabilities for decay from the L and M shells to the K shell have been computed by Storm and Israel (1967). In this interaction, the initial photoelectron will have an energy of $E - 34.561$ keV.

If a photon interacts via the L shell in xenon, there are 3 possible states in the L shell where the interaction could occur, with either fluorescence or Auger electron, and with innumerable decay modes. Table 3.3 lists these various possibilities where only the most probable decay modes have been selected. Further listing would be beyond the resolution of the detectors. The initial photoelectron will have an energy of $E - 5.445$ keV, $E - 5.102$ keV, or $E - 4.782$ keV, depending on where the interaction occurred.

Finally, if an interaction occurs via the M shell, the problem is greatly simplified as the energy of the photoelectron will greatly exceed the energy of the Auger electron or the characteristic photon. If any anticoincidence occurs, it will be generated by the photoelectron, which will have an average energy of $E - 1.045$ keV.

2. Balloon Experiment Resonance Escape/Photoelectron Anticoincidence. The built in anticoincidence system has a troublesome drawback. Characteristic photons could leave the cell of the initial reaction (resonance escape) and interact in a neighboring cell, thus

causing the event to be rejected. Furthermore, in the case of high photoelectron energies, the photoelectron could also leave one cell and penetrate into another. For the balloon system, 3 keV is needed to trigger anticoincidence.

To more fully understand these effects, Monte Carlo calculations were carried out for detectors filled with 1 atm xenon and methane quench gas. Figure 3.5 shows the results of these calculations for the resonance escape problem, for both the K- and L- shell, where the initial photoelectric effects were allowed to occur over the entire volume of the detector. During balloon borne observations, the residual atmosphere absorbs all photons with energy less than approximately 15 keV. Above 15 keV, photons interact uniformly with respect to depth in the detector. This allows a simple tabulation of the results. Table 3.4 lists the fractions of characteristic photons which leave the detector (resonance escape) and which remain in the cell of the initial interaction.

For the photoelectrons, Berger and Seltzer (1964) give electron ranges based on the continuous-slowing-down-approximation, or Bethe's differential electron energy loss expression. In the 10-80 keV range, these data can be fit very well with an $E^{+5/3}$ expression, in good agreement with the power laws of Katz and Penfold (1952) and Cosslett and Thomas (1964). The range defined by Berger and Seltzer (1964), however, is a path length and not a start to finish distance, where multiple scattering into or out of the beam has not been considered. Evans (1955) reports that the actual path length might be from 1.2 to 4 times the thickness of material traversed, depending on the energy of electrons and the Z of the material. Interpolation of the data of

Cosslett and Thomas (1964) suggests a factor of 1.75 for xenon at the Cd^{109} line.

Monte Carlo calculations show that for the energy range of this balloon experiment, the fractions of electrons to reach neighboring cells and either generate anticoincidence or mark bit are linear as a function of range and are $.345f$ for layer 1 and $.468f$ for layers 2 through 7, where f is the ratio of electron range to cell width. Direct measurements of the anticoincidence due to electrons are possible, but difficult to interpret as one needs to consider the effects of resonance escape photons which cannot be independently observed. Accepting the correction factor of Cosslett and Thomas (1964), and recalling that an energy deposition of 3 keV is required for anticoincidence, the fraction of events lost is given by

$$A_{\text{LAYER 1}} = .000417 \left[E^{5/3} - 3^{5/3} \right], \quad (3.4)$$

$$A_{\text{LAYER 2-7}} = .000566 \left[E^{5/3} - 3^{5/3} \right]. \quad (3.5)$$

Comparison of the theoretical response of the detector with actual observations of laboratory calibration sources as in Figure 3.6 shows the good agreement achieved by using the computed detector response parameters. The only serious differences between computed and observed values are on the low energy side of the strong lines, where an excess of counts is observed. The primary contributions to this excess are Compton absorption in the gas as opposed to photoelectric absorption, a factor of approximately 1%, and gas contamination by electron affinity gasses like oxygen which reduce the effective charge deposited on the anode. A smaller contribution, due to electrons which leave one

cell but do not carry enough energy to cause anticoincidence, exists, and has been neglected in the computation of the parameters. Figure 3.6 also shows the intensity of the K-shell resonance escape lines and their relative importance. This effect manifests itself in generating a spectrum with a component below 15 keV, a region where atmospheric absorption prevents a direct contribution. The small line at Channel 32 of the Am^{241} spectrum is due to Cd^{109} contamination in the source.

3. Rocket Experiment Resonance Escape/Photoelectron Anticoincidence. The primary difference between the rocket experiment and the balloon experiment was the ability of the rocket detectors to observe below 15 keV. Consequently, M-shell interactions play a very important role. The problem is greatly simplified however because the characteristic photons from the M-shell (typically of energy of 1 keV or less) have a $1/e$ range of less than .018 cm and consequently resonance escape effects can be completely ignored. Also, the range of the Auger electrons is so short as to not travel from one cell to the next, and their energy so small (≤ 1.5 keV) so as not to trigger anticoincidence should they escape one cell. Thus, only the anticoincidence due to the photoelectrons need be considered.

Above the K-shell, the quantum efficiency is low enough to allow one to assume that events occur uniformly throughout the depth of the detector, and Monte Carlo calculations similar to those for the balloon detector were used to calculate fractions for resonance escape photons (Table 3.5) and electron ranges. The same $E^{+5/3}$ range-energy relation is used, and 1.5 keV is needed to cause the logic of the rocket system to fire. As for the balloon detector, the end point to end point

electron distance is taken to be a factor of 1.75 less than the actual path length computed from the range-energy relation.

Between the K- and M-shells, a uniform absorption of X-rays throughout the depth of the detector cannot be assumed, especially at lower energies. Consequently, the interaction depth was considered in the Monte Carlo calculations, and the resonance escape and electron anticoincidence parameters are considered a function of energy between the L_I and K edge and M and L_{III} edge. Figures 3.7 and 3.8 are a plot of the fractions of resonance escape photons remaining in the same cell and leaving the detector and the relationship between electron range and anticoincidence as a function of energy. The flattening of the range-anticoincidence curve in the 15 to 35 keV band justifies the assumption of allowing photons to interact uniformly throughout the depth of the detectors in the Monte Carlo calculations for energies above 34.561 keV. Resonance escape photon parameters for the energy band between the L_I and L_{II} edge and L_{II} and L_{III} edge are also listed in Table 3.5.

Comparison of the theoretical rocket detector response with observation as in Figure 3.6 shows excellent agreement.

As another point in proof of the validity of the schemes for determining the detector parameters, one of the new OSO-I X-ray proportional counters, identical in principle of the balloon and rocket borne detectors, was exposed to the same continuous X-ray beam as a lithium drifted silicon crystal. Folding of the beam model through the detector response functions in the 2 to 20 keV band showed no disagreement, within statistics.

4. Linearity. To verify the proportionality of the detectors, they were exposed to radioactive sources with characteristic lines. Table 3.6 lists some of these sources typically used in the laboratory, with their characteristic energies. Additional information on line energies and intensities can be found in Nuclear Data Sheets (1966), Strominger et al. (1958), and Storm and Israel (1967). Figure 3.6 shows typical responses to these sources, and Figure 3.9 points out the energy-channel relationship for layer 2 of the balloon experiment.

If an event follows closely behind another, the energy of the second event will appear to be slightly lower than it should due to a baseline shift. The entire electronics system is capacitance coupled and does not return to a zero baseline instantly. Figure 3.10 shows this effect for a Cd^{109} line where the count rate was increased by moving a Co^{60} source closer to the balloon detector. Defining E_0 as the energy of the line at zero count rate, the observed energy E at some count rate λ is found to be approximately

$$E = E_0 (1 - .0115 \lambda) , \quad (3.6)$$

where λ is the number of events per data word for the balloon system. For the rocket experiment,

$$E = E_0 (1 - .115 \lambda) , \quad (3.7)$$

where λ again is the number of events per data word. Using Equation 3.6, the true energy of a line will then become

$$E = E_0 (1 - .0115 \lambda) / (1 - .0115 \lambda_0) , \quad (3.8)$$

where λ_0 corresponds to the data rate with the calibration source and λ' the data rate during flight observations. Neglecting this effect

during analysis of flight data will result in less than 1% error in the position of a line feature.

5. Resolution. Figure 3.6 also points out the validity of the assumption that the broadening of a line from a calibration source can be represented by a normal distribution, where the resolution is defined as the full width at half maximum per energy of the line. Line width as a function of energy shown is in Figure 3.11 for layer 2 of the balloon experiment and it can be approximated by an expression of the form

$$\Delta E = aE + b\sqrt{E}, \quad (3.9)$$

where a and b are constants experimentally determined. In Equation 3.9, the square root term comes from the definition of the resolution standard deviation while the linear term is strictly empirical. The resolution for the higher energy lines appears to be broadened considerably more than expected. This is due to multiple lines in the sources at these energies which make it impossible to observe only a single line, and measure a single resolution.

D. Electronics and Timing

The electronics used for both the rocket and balloon experiments was essentially identical. In the detector, X-rays interact primarily via the photoelectric effect; the resulting avalanche of electrons on the anode deposits typically 10^{-14} coulombs, which is converted to a negative output pulse by a high gain linear charge sensitive amplifier

(Figures 3.3 and 3.4). Circuit diagrams and further details have been presented by Birsa et al. (1972).

The event is immediately pulse height analyzed and coded into a continuous data stream, one word of 16 bits every 320 μ sec for the rocket experiment, and every 3200 μ sec for the balloon experiments. Each data word contains 3 bits of layer ID, 7 bits of pulse height analysis (127 channels), 1 bit for horizontal coincidence, and 5 bits for an event scalar. As it is possible to have more than one event per data word, only the first event is pulse height analyzed while all events are counted in the scalar.

The data stream is organized into frames of 64 words, the first word being a sync word and containing no data. Word 33 contains house-keeping information on the electronics like anticoincidence rates from the various layers and the sums of all bad events. Word 2 and 34 remain blank except for the scalar, which accumulated events during words 1 and 2 and words 33 and 34, respectively.

The logic of the encoder (Cancro et al., 1968) inhibits the scalar from accumulating events during the first 1/16th of each data word while data registers are transferred and cleared. Pulse height analysis, however, can be initiated during this time. If an event occurred during a previous word, a 5 μ sec reset follows the transfer and clear, during which time the pulse height analysis is inhibited while event accumulation continues. Table 3.7 lists the fractional times for these inhibit periods, plus the electronics dead time and anticoincidence time. Included in Table 3.7 is the effect of the 1.5 μ sec wide pulses which signal an event.

In addition to the pulse height analysis and event temporal analysis, the distributions of events can be studied to verify the proper functioning of the electronics. Due to the complex nature of the system, Poisson statistics

$$P(m, t) = \frac{1}{m!} (\lambda t)^m e^{-\lambda t} \quad (3.10)$$

must be modified. In Equation 3.10, m is the number of events, λ the rate of events per data word, and t the fractional time of a data word.

Assuming zero dead time and no anticoincidence, the probability $p(m)$ of observing m events in the scalar for each associated pulse height analysis is given by

$$\begin{aligned} p(0) &= (1 - R_p) P(0, a) \sum_{m=1}^{\infty} P(m, x) \\ &= (1 - R_p) (e^{-a\lambda} - e^{-\lambda}) \quad , \end{aligned} \quad (3.11)$$

$$\begin{aligned} p(m) &= (1 - R_p) P(m, a) + R_p P(m, a - y) \\ &= \frac{1}{m!} \lambda^m e^{-\lambda a} \left[(1 - R_p) a^m + R_p (a - y)^m e^{\lambda y} \right], m=1, 2, \dots \end{aligned} \quad (3.12)$$

where

R_p = observed number of pulse height analysis in the sample,
per data word,

X = fractional scalar inhibit time,

$a = 1 - X$,

y = fractional PHA inhibit time.

Just as it was possible to have pulse height analysis without an event recorded in the scalar, the probability $p_N(m)$ of observing m

events in a scalar without an associated pulse height analysis is

$$p_N(0) = 0, \quad (3.13)$$

$$\begin{aligned} p_N(m) &= R_p P(0, a-y) P(m, y) \\ &= R_p e^{-a\lambda} \frac{1}{m!} (y\lambda)^m, \quad m=1, 2, \dots \end{aligned} \quad (3.14)$$

The probability $p_g(m)$ of observing m events in the scalar of word 2 and 34 is

$$\begin{aligned} p_g(m) &= P(m, 2a) \\ &= \frac{1}{m!} (2a\lambda)^m e^{-2a\lambda}, \quad m=1, 2, \dots \end{aligned} \quad (3.15)$$

The probability p_z of observing no words which have associated pulse height analysis and scalars is

$$\begin{aligned} p_z &= P(0, 1) + R_p P(0, a) \sum_{m=1}^{\infty} P(m, x) \\ &= e^{-\lambda} + R_p (e^{-a\lambda} - e^{-\lambda}) \end{aligned} \quad (3.16)$$

In spite of the fact that Equation 3.16 is a transcendental equation, it can be used to define λ . λ can also be defined on the basis of Equation 3.15 as

$$\lambda = \frac{-1}{2a} \ln(1 - R_g) \quad (3.17)$$

where R_g is the observed number of non zero word 2 and word 34, per total number of word 2 and word 34. It should be clear that for samples of data where the data rate λ changes, this analysis breaks down.

The addition of dead time does not seriously affect the above analysis. During typical rocket flights, one experiences values of λ from .03 to .07, and for typical balloon experiments, .18 to .25. The dead time corrected value of λ is λ_d , where

$$\lambda_d = \frac{\lambda}{1 + d\lambda} \quad , \quad (3.18)$$

where d is the fractional dead time. In the worst case for the rocket experiment, this gives a .07 percent error, while for the worst balloon case, a .03 percent error.

Considering the anticoincidence time, the corrected value of λ becomes λ_a , where

$$\lambda_a = \lambda (1 - q) \quad (3.19)$$

where q is the fractional anticoincidence time. Worst errors for the rocket and balloon experiments are typically .7 and .07 percent, respectively.

Substituting both the anticoincidence effect and dead time, the corrected λ becomes λ_c , where

$$\lambda_c \cong \frac{\lambda (1 - q)}{1 + d\lambda} \quad (3.20)$$

where the worst errors for the rocket and balloon experiments are .8 and .1 percent. Consequently, no significant error is introduced by neglecting these effects.

E. Collimation

Both of the detectors on the rocket experiment and the balloon experiment had circular collimators. For each tube, the effective transmission $\epsilon(\theta)$ as a function of incident angle θ with respect to maximum transmission is

$$\epsilon(\theta) = \frac{1}{\pi} \cos \theta \left(\phi - \sin \phi \right) \quad , \quad (3.21)$$

where

$$\phi = 2 \cos^{-1} \left[\frac{\ell}{d} \tan \theta \right] \quad (3.22)$$

and

$$0 \leq \theta \leq \tan^{-1} \frac{d}{\ell} \quad (3.23)$$

In these expressions, d is the diameter of the collimator tube and ℓ is its length. Table 3.8 lists various parameters for each of the collimators.

The disparity in the response of the $1/2^\circ$ collimator as compared to a single $1/2^\circ$ tube arises from the manufacturing technique. Typically 50 of the titanium collimator tubes would be cemented together, side-by-side, on a smooth surface with Eastman 910. These slabs were then stacked and cemented with epoxy, approximately 40 layers high, to form collimator modules, which in turn were cemented into the collimator frame. Even though every effort was made to keep the tubes and modules parallel, the questions of how much misalignment was built in and how much could the collimator bend in a vacuum, arose.

To answer these questions, the $1/2^\circ$ detector was placed in a vacuum and turned in front of an Fe^{55} radioisotope 150 feet away. Three sections of the collimator were thus studied, with a beam aperture of 6" diameter on the surface of the collimator. Table 3.9 summarizes the results of this experiment, where the detector was turned first on one axis, and then on the other. The resultant data were analyzed by χ^2 techniques and Table 3.9 lists the parameters which best fit the data. It is readily apparent that the collimator did not bend, as the bowing angle is the amount the edge of the 6" diameter aperture is away from being parallel with the center.

The misalignment of collimator tubes could be best represented by a gaussian distribution such that the total collimator response $\epsilon_{coll}(\theta)$ is

$$\epsilon_{coll}(\theta) = k \int_{-\pi/2}^{\pi/2} e^{-\frac{1}{2}\left(\frac{\theta-\theta'}{\sigma}\right)^2} \epsilon_{tube}(\theta') d\theta', \quad (3.24)$$

where k is a constant, σ is defined by Table 3.9, and $\epsilon_{tube}(\theta')$ is defined by Equation 3.21. Figure 3.12 presents the total collimator response for each of the three detectors.

A careful response study was not conducted on the 3° collimator and the balloon experiment collimator as these collimators are both more rugged in construction, and a small effect as noted on the 1/2° detector would be insignificant in the 3° and 4° detector.

Graded shielding consisting of 1/16" lead, 1/16" tin, 1/16" copper and the 1/2" aluminum walls of the balloon detector reduce transmission of 110 keV (upper limit of dynamic range plus energy of K escape photon) photons through the sides and front of the detector not covered by the collimator by a factor of 10^3 . Approximately 3/32" tin, 1/16" copper, and 1/2" aluminum reduce transmission through the back of the balloon detector by a factor of 800.

The various thicknesses of tin and copper on the rocket experiment reduce transmission of 70 keV photons through the walls and back in all cases by more than a factor of 100.

F. Comparison of Balloon Experiment

Several research groups throughout the world are actively engaged in balloon borne X-ray astronomy experiments. With each group, there

is a different type of experiment; yet all experiments fall into 2 categories, proportional counters and scintillation crystals. Proportional counters can be built to very large sizes, usually an order of magnitude larger than crystals, while the detection efficiency of crystals in the region where proportional counters can be used (15 to 80 keV) is almost 100% compared to the rapidly decreasing efficiency with respect to energy in proportional counters. Crystals can be effectively used up to an energy of typically 500 keV. The resolution of proportional counters is approximately 4 times better than that for crystals and their background levels usually 4 times less.

Table 3.10 lists some of the latest balloon experiments in X-ray astronomy, listing important detector characteristics. The experiments tabulated here are those of Smathers (1972) of NRL, Matteson (1971) of UCSD, Harnden (1971) of Rice, and Agrawal (1972) of the Tata Institute.

CHAPTER IV

OBSERVATIONAL PROGRAM

A. Summary of Flights

The observational program for the data presented in this thesis consisted of one sounding rocket flight and four balloon flights, each of which is discussed separately below. Table 4.1 summarizes the results of this flight program.

B. Rocket Flight 13.009

The rocket experiment was launched from White Sands Missile Range aboard an Aerobee 170 sounding rocket at 9h 0m 0.54s UT on May 19, 1972. Table 4.2 summarizes important times during this flight. After the rocket shut down, the experiment high voltage was turned on and a Fe^{55} source on both of the doors over the detectors provided an inflight calibration; this same calibration was repeated after the doors closed following the source observation.

Guidance during this flight was provided by rate gyroscopes which were aligned by a startracker on two stars, α Cyg and β Cas. The startracker axis was mounted parallel to the axes of the detectors. Preflight tests showed this alignment to be maintained even after heavy vibration in all axes, both harmonic and random. After setting of the gyroscopes by the star tracker, the gyroscopes maneuvered the experiments to observe Cas A and Tycho. Figure 4.1 shows the path of the experiment axes in the celestial sphere.

Aspect information on the experiment axes came from 2 Nikon F cameras hard mounted to the detector bodies and aligned with a Cd^{109} X-ray source prior to the flight. Figure 4.2 shows the results of the star field analysis (see the Appendix) applied to the photographs from both cameras, where the offset is defined as the angular separation between the intended and computed positions of the detector axes. The error bars shown in Figure 4.2 correspond to inaccuracies in the star field aspect solution only. In addition, there remains a systematic error of ± 6.1 arc minutes for the 3° detector and ± 3.2 arc minutes for the $1/2^\circ$ detector due to uncertainties in the location of the X-ray center of the detectors. Table 4.3 summarizes the effective observing times for each source and detector, where the effective observation is the product of the observing time and collimator transmission efficiency.

Figure 4.3 shows the observed count rate in the 1.5 to 20 keV band, as a function of time for the rocket flight. The top trace represents the data from the first layer of the 3° detector (layer B1) in which most of the counts were accumulated. The pre and post observation calibrations by the Fe^{55} source in the door over the detector are clearly shown here by a count rate of approximately 170 cts/sec. The small increase in count rate prior to the Cas A observation represents the sweep past Cas A ($< .5^\circ$) while the rocket was maneuvering from α Cyg to β Cas. The second trace represents the observed counts in the propane/helium first layer of the double gas $1/2^\circ$ detector (layer A1). This layer was designed to act as an anticoincidence to all ionizing particles while being transparent to photons. No increase in count rate was expected and observed as the sources came into the field

of view. The last trace represents the counts observed in the first xenon layer of the $1/2^\circ$ detector (layer A2). Due to the narrow collimator and relatively large offset from Cas A and Tycho, the observed count rate from these targets is significantly lower than that in layer B1. Spectral analysis was performed on the data from layers B1, B2 and B3 and layers A2 and A3. Layers B2, B3 and A3 contributed data at high energies only.

C. Balloon Program

1. Gondola System. All of the balloon lights were conducted with the same balloon gondola and guidance system, an "alt-azimuth" system as sketched in Figure 4.4, designed and operated by the Stabilization and Control Branch of the Earth Observations Systems and Systems Engineering Division of NASA Goddard Space Flight Center. The earth's gravitational field defined the vertical direction, where pendulum motion of the gondola under the balloon was considered negligible. The earth's magnetic field defined directions in the horizontal plane.

An on-board analog computer determined the proper pointing direction of the detector, based on (a.) the declination of the star, δ ; (b.) the latitude of the gondola, β ; (c.) the elevation of the detector axis above the horizontal plane, ϵ ; (d.) the orientation of the gondola with respect to the earth's magnetic field, γ ; and (e.) the hour angle of the star with respect to the gondola, α . Error signals which drove the elevation, V_{el} , and the azimuth, V_{az} , are given by

$$V_{az} = \cos \delta \sin \alpha \cos \gamma - \cos \delta \cos \alpha \sin \beta \sin \gamma - \sin \delta \cos \beta \sin \gamma \quad (4.1)$$

$$V_{el} = \sin \delta \sin \beta \cos \epsilon - \cos \delta \cos \alpha \cos \beta \cos \epsilon + \cos \delta \sin \alpha \sin \gamma \sin \epsilon \\ + \cos \delta \cos \alpha \sin \beta \cos \gamma \sin \epsilon + \sin \delta \cos \beta \cos \gamma \sin \epsilon \quad (4.2)$$

The elevation drive consisted of a simple lead screw and lever arm while the azimuth drive required an inertia wheel for small azimuth adjustments and a momentum unloader (coupling between the gondola and balloon) for large adjustments, activated when the inertia wheel turned faster than a predetermined rate.

The operational characteristics of the guidance system required the computer to be set before launch without any possibility for update should the winds at ceiling be other than expected. Deviations of 1 degree in latitude and longitude are typical, but are also within the field of view of the collimator.

Two inches of polystyrene foam insulated the front of the detector from cold and one to two inches of polyurethane foam provided protection for the sides and back of the detector. In addition, 140 watts of power under the command of a pair of thermal sensors kept the detector at room temperature throughout the flights. Similar insulation and heating was provided for the experiment camera and experiment electronics.

Several levels of redundancy provided aspect information. A guidance magnetometer and the elevation angle readout provided inputs to the computer to define the proper azimuth and elevation of the detector. A second magnetometer with fine readout capability, accurate to better than .1 degree, provided azimuth information independent of the guidance magnetometer. A gondola system camera with an approximately

20 degree field of view and hard mounted to the detector but pointed 30° lower in elevation than detector axis took star field pictures every 15 seconds, each exposure being approximately 3 seconds long. The experiment camera, a Nikon F with a 50 mm lens (approximately 40° field of view), was also hard mounted to the experiment and took one 3 second exposure every 78.6 seconds. The larger field of view required a smaller offset of approximately 10 degrees to prevent obscuration of the entire field of view by the expanded balloon and at the same time allowed the target star and the alignment target to be within the field of view. Longitude and latitude information were obtained from radar observations (out to a distance of approximately 55 miles), tracking of a Rawinsonde signal, and an Omega System (based on Loran navigational radio transmissions) and were accurate to better than ± 1 mile. Altitude information came from a barotransmitter (accurate to ± 200 feet) and a Rosemount pressure transducer (accurate to ± 1000 feet).

With the exception of the film in the cameras, all data was telemetered to the ground and recorded on magnetic tape. Several of the balloon control and status units had their own telemetry. All of the experiment and gondola information was transmitted on a single L-Band transmitter at 1485.5 MHz. Detector data in PCM format modulated the highest frequency subcarrier. The second subcarrier carried the output of a 45 segment commutator sampling at 20 Hz, containing all of the detector temperatures, pressures, and voltages and the camera shutter position. The remaining subcarriers were used for gondola magnetometers, elevation, unloader, inertia wheel speed, etc. During the flight, the gondola analog functions were recorded on a strip chart in addition to being recorded on magnetic tape.

2. Balloon Flight 646-P. The first attempt to observe Cyg X-1, on October 27, 1971, ended in failure. The 10.6 million cubic foot balloon was launched from the National Center for Atmospheric Research (NCAR) Scientific Balloon Facility at Palestine, Texas at 1240 CST. At 99,500 feet, the barotransmitter and beacon failed, making altitude and position determinations (except visual) impossible. At ceiling, estimated to be approximately 134,000 feet, the pointing system was activated but immediately malfunctioned and pointed the detector permanently at an angle of approximately 60 degrees off the vertical while still holding the proper azimuth position. Termination occurred after one hour at ceiling as the FAA requires a beacon for determining the position of the balloon after sunset. No X-ray sources were observed.

3. Balloon Flight 683-P. A second attempt to observe Cyg X-1 on June 19, 1972 resulted in marginal success. The 10.6 million cubic foot balloon was launched from the NCAR Scientific Balloon Facility at Palestine, Texas at 2052 CDT and rose to an altitude of 133,100 feet at 0018 CDT, June 20, 1972, where the guidance system was activated. Figure 4.5 shows the altitude, latitude, longitude and experiment elevation angle as a function of time. In the process of orienting the gondola to the proper azimuth, the inertia wheel failed. As the momentum unloader will only turn the gondola when the inertia wheel attains high speeds, no further control over the azimuth orientation was possible. The elevation drive, however, did function properly and consequently, the balloon was allowed to continue to remain at ceiling in the hope that some transits of Cyg X-1 would occur.

Figure 4.6 shows the angular position of the detector axis in the celestial sphere, where each dot or dash represents a position as determined from the experiment camera, the numbers indicating sequential photos. It should be noticed that shear winds at ceiling caused the balloon to reach angular speeds of up to 1 degree/second and also, at other times, change its direction. Due to the instability which resulted in an unsuccessful attempt to control the gondola, there remained an oscillation in the azimuth plane of ± 13 degrees which was damped to approximately ± 1 degree at the end of the 6 hour flight. The period of the oscillation was approximately 41 seconds.

From Figure 4.6 it is also apparent that Cyg X-1 was crossed several times, as well as Cyg X-2 and Cyg X-3. Furthermore, a number of weak UHURU X-ray sources were passed but none of these resulted in an increased count rate. Figure 4.7 presents the number of photons observed in the 15 to 30 keV band, as a function of time. In spite of the fact that the data points of Figure 4.7 are integrations over 1 minute of observation (1.5 times the oscillation period of the gondola), an unprecedented signal to background of approximately unity was observed; had the detector been on target, this ratio would have been 1.2:1.

To obtain estimates of the fluxes from Cyg X-1, Cyg X-2, and Cyg X-3, the question of angular separation between source and detector axis must be resolved. Since the fine readout magnetometer and the elevation readout functioned properly, it is possible to obtain exact pointing information. Defining the right ascension and declination of the source as α and δ , the right ascension and latitude of the detector as α_0 and β where α_0 will be considered an unknown due to

variable wind drift (changes in the latitude β are slow compared to changes in the longitude α_o), and the detector elevation angle as ϵ , each star field picture can be used to define α_o , where

$$\alpha_o = \alpha - \cos^{-1} \left[\frac{\sin \epsilon - \sin \beta \sin \delta}{\cos \beta \cos \delta} \right] \quad (4.3)$$

Values of α_o for times between photographs are determined by interpolation. Also from each star field photograph, defining γ as the angle between an arbitrary gondola axis in the azimuth plane (as determined by the fine readout magnetometer) and the earth's magnetic field, a reference angle γ_o can be defined as

$$\gamma_o = \gamma - \sin^{-1} \left[\frac{\cos \delta \sin (\alpha - \alpha_o)}{\cos \epsilon} \right] \quad (4.4)$$

or by

$$\gamma_o = \gamma - \cos^{-1} \left[\frac{\sin \delta - \sin \epsilon \sin \beta}{\cos \epsilon \cos \beta} \right] \quad (4.5)$$

where again, γ_o between two successive photographs is determined by interpolation.

To determine the right ascension and declination of the detector axis, all that is now needed are the values of γ_o and α_o , and the output of the fine readout magnetometer, γ , shown schematically in Figure 4.8. For simplicity, only the values of γ at the extremes of each oscillation were measured, the values in between being determined by fitting a curve of the form

$$\gamma = A \cos (Bt - c) + D \quad (4.6)$$

the sinusoidal term taking account of the oscillation and the linear term the random rotational motion, assumed to be constant for each half period. With γ known at every second, and γ_0 and α_0 determined by interpolation, the declination δ_s and right ascension α_s of the detector axis are

$$\delta_s = \sin^{-1} \left[\sin \epsilon \sin \beta + \cos \epsilon \cos \beta \cos (\gamma - \gamma_0) \right] \quad (4.7)$$

and

$$\alpha_s = \alpha_0 + \cos^{-1} \left[\frac{\cos \epsilon - \sin \delta_s \sin \beta}{\cos \delta_s \cos \beta} \right] \quad (4.8)$$

where ϵ and β are also interpolated between photographs even though instantaneous, but not rapidly varying values exist.

Table 4.4 summarizes the results of this analysis, listing the product of the time of observation and the efficiency of the collimator as the effective exposure. It should be noted that the gondola system camera was not used in this analysis. In the calibration of this camera, several steps were taken, each step being accurate to only $\pm .5$ degrees. The same is true about the position of the fine read-out magnetometer axis, but this could be compensated for by the definition of a reference angle γ_0 . The experiment camera was aligned with respect to the detector axis in a one step process. The X-ray center of detector was determined to within $\pm .1$ degree by moving a Cd^{109} source in front of the detector at a precisely measured distance, and then taking a photograph of this center with the flight film. Corrections for parallax thus define a point on each photograph which corresponds to the detector axis, the stars being used to define a right ascension and declination of this point, as discussed later.

Termination occurred at 6:16 CDT on June 20 over western Texas.

4. Balloon Flight 695-P. The first attempt to observe Cyg X-3 on August 29, 1972 ended in failure as the balloon burst on the launch pad. The experiment never left the launch vehicle.

5. Balloon Flight 696-P. A second attempt to observe Cyg X-3 was made the following day, August 30, 1972, again from the NCAR Scientific Balloon Facility at Palestine, Texas. Launch occurred at 16:41 CDT and due to a slightly larger balloon (11.6 million cubic feet) an altitude of 129,200 feet was reached very rapidly at 18:31 CDT. Figure 4.9 presents the latitude, longitude, elevation angle, and altitude for the experiment. As on previous flights, the detector was pointing toward zenith during ascent. Figure 4.9 shows that the altitude information as determined from the barotransmitter and Rosemount pressure transducer are in slight disagreement. The data from the barotransmitter are probably more accurate inasmuch as the sudden increase in altitude at 0200 UT as registered by the barotransmitter corresponded with a sudden increase in wind drift, typical for higher altitudes.

Activation of the command system occurred at 19:30 CDT, and the system performed properly with the exception of several instances where the momentum unloader froze for several minutes and where the shear winds tried to rotate the balloon faster than the azimuth control system could correct for. Also small instabilities lasting for approximately 2 minutes followed the commands to move the detector off the source and back on. These movements consisted of 12-degree offsets in

the azimuth plane. Throughout times of stability, there were still continuous excursions from proper azimuth which were at most $\pm .7$ degrees, and since the pointing error goes as the product of the cosine of the elevation angle and the azimuth error, this residual effect is of little consequence.

Figure 4.10 shows the count rate in the 20 to 30 keV band as a function of time, plus two independent versions of the aspect solution. The individual vertical lines every 78.6 seconds are the results of the star field analysis with the experiment camera film, the probable errors being indicated by the length of the lines. The horizontal bars are 3 minute averages of the pointing solution based on the output of the fine readout magnetometer and the elevation angle readout. Statistical errors on these 3 minute averages are typically $\pm .2$ degrees. Any slight misalignment in the guidance system of the gondola can result in the observed systematic disagreement in aspect. Inasmuch as the experiment camera was aligned in a single step procedure as compared to the multistep procedure needed for the guidance system, each step being accurate to only $\pm .5^\circ$, confidence is placed in the experiment camera aspect solution.

Termination occurred at 1:35 CDT, August 31 over western Texas, and the experiment was recovered and returned to Palestine, Texas within a day. Immediate exposure to a Cd^{109} X-ray calibration source showed the detector to be functioning properly. During the flight, the pressures inside the detector and high voltage area remained constant and all temperatures remained at approximately room temperature.

CHAPTER V

RESULTS AND DISCUSSION

A. Data Analysis Procedure

1. Spectral Analysis. Ideally, the response of a detector to radiation should be linear, i.e.

$$N(E) = k S(E) \quad (5.1)$$

where $S(E)$ is the source function and $N(E)$ the observed spectrum, both as a function of energy. In the case of proportional counters, the quantum efficiency of the gas decreases rapidly as a function of energy, there is a non zero energy resolution, and some characteristic radiation escapes the detector, reducing k not only to a non linear function of energy, but more properly to the kernel of an integral equation,

$$N(E) = \int_0^{\infty} R(E, E') S(E') dE' \quad (5.2)$$

where $R(E, E')$ is defined as the response function.

Analytic solutions of Equation 5.2 are impossible except for cases where the source function can be expressed by a delta function. Numerical solutions reduce Equation 5.2 to matrix algebra, where $S(E')$ and $N(E)$ become vectors

$$S(E') \rightarrow S = \begin{pmatrix} S_1 \\ S_2 \\ S_3 \\ \vdots \\ S_j \end{pmatrix} \quad (5.3)$$

$$N(E) \rightarrow N = (N_1 \ N_2 \ N_3 \ \dots \ N_i) \quad (5.4)$$

and the response function becomes a response matrix

$$R(E, E') \rightarrow R = \begin{pmatrix} R_{11} & R_{12} & R_{13} & \cdots & R_{1j} \\ R_{21} & R_{22} & R_{23} & & R_{2j} \\ R_{31} & R_{32} & R_{33} & & R_{3j} \\ \vdots & & & & \\ R_{i1} & R_{i2} & R_{i3} & \cdots & R_{ij} \end{pmatrix} \quad (5.5)$$

Once the response matrix is generated for a particular detector, various spectra S^α can be folded through the response function and the result compared with the observed spectrum, via χ^2 analysis. The computed values of χ^2 take the form

$$\chi^2_\alpha = \sum_{i=1}^m \left(\frac{N_i - \sum_{j=1}^m R_{ij} S_j^\alpha}{\sigma_i} \right)^2 \quad (5.6)$$

where σ_i^2 is the variance in the observed value of N_i .

With the addition of small cells and vertical and horizontal anti-coincidence in the detectors, the response matrix is a complex array. Considering first the region below the 4.782 keV L_{III} edge, the response matrix elements for the ℓ th layer can be approximated by

$$R_{ij}^\ell = {}^m R_{ij}^\ell = Q_j^\ell A_{j-Em}^\ell G_{ij} \quad (5.7)$$

where

$$Q_j^\ell = T_j^w (\sigma_j)^{\ell-1} (1-\sigma_j) \quad (5.8)$$

= the quantum efficiency of the ℓ th layer in which

$$T_j^w = e^{-\mu_j^w d_w} \quad (5.9)$$

= transmission through detector window of thickness

d_w (μ_j^w is absorption cross section for energy corresponding to index j),

$$\sigma_j = e^{-\mu_j^{\text{gas}} d_{\text{gas}}} \quad (5.10)$$

= transmission through one layer of detector gas of thickness d_{gas} (μ_j^{gas} is gas absorption cross section),

$$A_{jE_M}^{\ell} = A_k^{\ell} = \tau_k^{\ell} C (E_k^{5/3} - E_0^{5/3}) \quad (5.11)$$

= the fractional anticoincidence of the ℓ th layer for the energy corresponding to index k , (E_k), for which

τ_k^{ℓ} = anticoincidence - range parameter for energy E_k ,

C = range-energy constant (i.e., range = $C E^{5/3}$),

E_M = index corresponding to the energy of the M-shell of the gas,

E_0 = energy required to trigger anticoincidence in adjacent cells,

$$G_{ij} = \frac{1}{w_j \sqrt{2\pi}} e^{-\frac{1}{2} \left(\frac{i-j}{w_j} \right)^2} \quad (5.12)$$

= the gaussian distribution of width w_j which is assumed to describe the non zero energy resolution of the detector.

Advancing to the L_{II} edge, the response matrix becomes

$$R_{ij}^{\ell} = \left[\alpha_M^M R_{ij}^{\ell} + \alpha_{L_{III}}^{L_{III}} R_{ij}^{\ell} \right] (\alpha_M + \alpha_{L_{III}})^{-1} \quad (5.13)$$

where the α represent the relative absorption into the various shells and $^{L_{III}}R_{ij}$ is the appropriately modified version of Equation 5.7.

The expressions for the response matrix for the region between the L_I and K shells and above the K shell are exactly the same, where in

each case the atom can relax principally via 4 photons, the L_{β} and L_{α} and K_{α} and K_{β} , respectively. For the region between the L_{II} and L_I shells, the atom decays to the ground state primarily via only one photon, the L_{β} .

The total response matrix can finally be written for any energy region by just adding the appropriate additional "shell" response functions with the corresponding relative absorption to Equation 5.13. Due to the existence of resonance escape where large portions of the source function are observed typically 4 or 30 keV lower in the energy spectrum, this response matrix cannot be inverted and applied to the observed spectrum to deduce a unique source spectrum.

In computing the χ^2 for various source functions, the data from the 128 channels of the pulse height analysis are grouped into bins consistent with the resolution of the detectors (i.e., the first several bins contain only 1 channel each, the next few contain 2 channels, and the last bins contain typically 10 to 30 channels).

As the response function is representative of the detector only, galactic absorption and atmospheric absorption are considered as part of the source function, and thus any amount can be folded in on trial source spectra.

For the interpretation of the results of the χ^2 analysis, Evans (1955) and the Handbook of Chemistry and Physics (1963) provide graphs and tables relating the value of χ^2 with the number of degrees of freedom f and the probability P that another test under the same circumstances will have a larger value of χ^2 . The number of degrees of freedom are defined as the number of samples less the number of

constraints and parameters on the trial function. For χ^2 greater than 30, the probability is given by

$$P \cong \frac{1}{2\sqrt{2\pi}} e^{-\frac{1}{2}(\sqrt{2\chi^2} - \sqrt{25-1})^2} \quad (5.14)$$

Error limits on parameters describing a trial function are frequently defined in one of two ways. First, the limits on the parameters are those values for which the χ^2 yields a probability P of 10 percent, corresponding to a 90 percent confidence level. Second, limits on the parameter are defined at values of χ^2 for which

$$\chi^2 = \frac{1}{2} \left[\sqrt{2\chi^2_{MIN}} + 1 \right]^2 \quad (5.15)$$

where χ^2_{MIN} is the minimum value of χ^2 observed for all variations in the parameter

In the analysis of the data, response matrices were generated with rows and columns corresponding to the energy width of a single channel of pulse height analysis, for each layer of the experiment. In the response matrix for the balloon experiment, this amounted to 116 rows (for the 116 channels which provided useful data) and 200 columns (for the 80 keV energy band of the detector plus an additional 30 keV to take account of the resonance escape). Trial spectra with a resolution corresponding to 1 PHA channel were then multiplied by the response matrix, and the computed response grouped into bins and compared to the observed data via χ^2 analysis.

2. Temporal Analysis. Acceptable events in the detectors are coded into 320 μ sec data words in the rocket system and 3.2 msec data words in the balloon system; no knowledge is retained of where in the data word it occurred. This, however, has an advantage in that the

temporal history of the experiments exists in digitized form.

For a contiguous stream of data, two independent methods of searching for periodicities are a pulse fold method and harmonic analysis. In the pulse fold method, if the data is folded upon itself into P temporal bins, an approximate expression for the statistical significance of a disturbance in terms of the fraction f of events in the pulsed component is given by Boldt et al. (1971) as

$$\left(\frac{f}{1+f} \right)^2 \cong \left(\frac{\beta}{1-\beta} \right) \frac{m (2P)^{1/2}}{N_T} \quad (5.16)$$

where

β = duty cycle, or fractional pulse width,

m = number of standard deviations from the $f = 0$ value.

N_T = total number of events in the data sample.

For Equation 5.16 to be valid, the number of temporal bins P must be large (≥ 40). This technique is particularly useful when the approximate periodicity is known. Without this information, this method is costly and time consuming on the computer.

Cooley-Tukey harmonic analysis is a fast Fourier analysis in which N amplitudes are computed in approximately $N \log N$ operations instead of N^2 operations as required by standard Fourier analyses. (Cooley et al, 1967). The probability of white noise exceeding any Fourier amplitude A is

$$\text{Prob} \left\{ (a_m^2 + b_m^2) > A^2 \right\} = e^{-\left(\frac{A^2 k^2}{4N} \right)} \quad (5.17)$$

where k is the number of data points and N is the number of photons observed. Defining α as the increase in counting rate during the disturbance, and using a single amplitude corresponding to the primary

frequency component,

$$\begin{aligned} \xi &= \alpha \beta k / N \\ &= \pi A \beta k / N (2 - 2 \cos 2\pi \beta)^{-1/2} \end{aligned} \quad (5.18)$$

To obtain a simple expression for the upper limit on ξ , one can assume the approximation

$$\pi \beta \cong (1 - \cos 2\pi \beta)^{1/2} \quad (5.19)$$

and Equation (5.18) becomes

$$\xi \cong \frac{Ak}{N\sqrt{2}} \quad (5.20)$$

and the probability of obtaining an amplitude A corresponding to a pulsed fraction ξ for a N events is

$$p \approx e^{-N\xi^2/2} \quad (5.21)$$

Thus, as an upper limit, requiring 99% confidence that there is no true periodicity in the data stream at a specific frequency implies

$$\xi^2 \leq \frac{9.2}{N} \quad (5.22)$$

For $\frac{k}{2}$ independent Fourier amplitudes, the 99% confidence upper limit that there is no periodicity at any frequency implies

$$\xi^2 \leq -\frac{2}{N} \ln \left(\frac{2 \times 10^{-2}}{k} \right) \quad (5.23)$$

if no significant power is observed.

For non periodic variations, the data stream can be broken up into many sections, and each section into bins such that Equation 5.16 applies. Due to the need not to fold the data in this study, these upper limits are very insensitive to small short bursts of data.

A second independent means of noticing sudden disturbances in the data stream is to examine the distribution of events in the event scalar.

The modified Poisson distribution of Equation 3.12 very accurately prescribes the number of events expected per data word for a particular data rate.

3. Background Subtraction. As there can be more than one event per data word and since the first event only will be pulse height analyzed, background cannot be removed by simply subtracting data for equal amounts of time. The proper background subtraction will be

$$N_S = N_{BS} - f N_B \quad (5.24)$$

where

N_S = number of events due to the source,

N_{BS} = total number of events observed (background plus source),

N_B = number of background events.

To determine f , one notes that the probability of seeing a word with pulse height analysis is

$$\begin{aligned} P_{PHA} = R_P = & \left[1 - \sum_{m=1}^{\infty} P(m, 1) \right] \left[\sum_{j=1}^{\infty} P(j, 1) \right] \\ & + \left[\sum_{m=1}^{\infty} P(m, 1) \right] \left[\sum_{j=1}^{\infty} P(m, 1-\gamma) \right] \end{aligned} \quad (5.25)$$

where second order effects have been neglected. Then,

$$\begin{aligned} P_{PHA} &= 1 + e^{-2\lambda} (e^{\gamma\lambda} - 1) - e^{-\lambda} e^{\gamma\lambda} \\ &\approx 1 - e^{-\lambda}, \end{aligned} \quad (5.26)$$

with at most a .04 percent error in the rocket system and .002 in the balloon system. Consequently,

$$N_S = k (1 - e^{-\lambda_S}) \quad (5.27)$$

$$N_B = k (1 - e^{-\lambda_B}) \quad (5.28)$$

$$N_{BS} = k (1 - e^{-\lambda_{BS}}) = k (1 - e^{-\lambda_B - \lambda_S}) \quad (5.29)$$

and it follows that

$$f = e^{-\lambda_s} \quad (5.30)$$

assuming source plus background and background data were taken for the same amount of time. For differing times, then,

$$N_s = N_{BS} - \frac{t_{BS}}{t_B} e^{-\lambda_s} N_B, \quad (5.31)$$

where t_{BS} and t_B are the source plus background and background observation times, respectively,

In Equation 5.27, k represents the total number of data words available and N_s the number of pulse height analyses due to the source data alone. The actual number of events N'_s giving rise to these pulse height analyses is given by

$$N'_s = -k \ln \left(1 - \frac{N_s}{k}\right) \quad (5.32)$$

For $N_s \ll k$, one observes that $N'_s \approx N_s$, while for $N_s \rightarrow k$, $N'_s \rightarrow \infty$, or, the higher the observed count rate, the greater the probability of multiple events per data word.

4. Interstellar Absorption. Inasmuch as X-rays carry no charge, they are unaffected by the random magnetic fields of space and travel in a straight line from source to observer. Yet, the intervening interstellar matter (in the case of balloon borne experiments, the residual atmosphere of the earth) acts to absorb or scatter low energy X-rays out of the beam, as has been observed long ago by Grader et al. (1966) for Sco X-1, and recently by Bleach et al. (1972) for Cyg X-3 and Burginyon et al. (1973) for Puppis A. The interaction responsible for this absorption is primarily the photoelectric effect, with coherent and incoherent scattering playing an important role only at energies

greater than 10 keV.

Estimates for the magnitude of this absorption depend on the composition and density of interstellar gas. Early abundance tables based on chondritic meteorites reflected universal abundances (Cameron, 1959); later estimates (Brown and Gould, 1970) were based on the interstellar gas but failed to give the abundance of iron. Table 5.1 lists the values adopted for this work where the iron abundances for Seyfert galaxies (Nussbaumer and Osterbrock, 1970) and quasi-stellar objects (MacAlpine, 1972) have been assumed.

In rocket borne experiments, one needs only consider attenuation by the interstellar medium. Using cross sections from the semiempirical tables Storm and Israel (1967), a 1/e absorption at 1.5 keV corresponds to 9×10^{22} H atoms/cm² in the line of sight. Assuming a uniform distribution of gas in the galaxy, and .7 H atoms/cm³ (Burton, 1970), this corresponds to a distance of 4.2 kpc. In balloon experiments, a residual atmosphere of 2 gm/cm² has a 1/e absorption at 25 keV. Equivalent absorption by the interstellar gas corresponds to 1.3×10^{24} H atoms/cm² or a distance of .62 Mpc (approximately 20 times the galactic diameter).

B. Cas A Observations

1. Temporal Analysis. The first part of the sounding rocket experiment was devoted to an observation of Cas A. In the 60 second exposure, there are 6428 non zero events which were analyzed for temporal variations, 80% of these are attributable to the source itself.

Unfortunately, a malfunction in the telemetry coding resulted in the loss of words 1, 2, 33 and 34 out of every 64-word frame, but this artifact in the data record did not seriously affect the temporal analysis as the artificially induced periodicities are extremely narrow band and completely deterministic.

The fast-fold algorithm used a maximum of 10^5 data intervals per pass compared with a total of 1.92×10^5 320 μ sec intervals in this exposure and all periods between 12.8 msec and 13.1 sec were run with $40 \leq P \leq 80$, where P is defined as in Equation 5.16. There were no $\geq 5\sigma$ results which could not be directly attributed to the telemetry coding malfunction in the above period range. The upper limit to any periodic modulation of the data is then given by Equation 5.16, with $m = 4.8$, and graphically displayed in Figure 5.1 with the correction to Equation 5.16 being made in recognition of the fact that only 80% of N can be attributed to Cas A. As the number of independent Fourier periodic components in the entire record is $\sim 10^5$, and as the folding routine tests only the lowest 5% of these frequency components (i.e., $P \geq 40$), the 4.8σ stipulation on any individual component is, in effect, equivalent to an upper limit at the 99% confidence level for any periods in the range of 12.8 msec to 13.1 sec.

Using the Fourier-decomposition approach, the data were broken into six separate 10.49 sec samples (with .095 Hz resolution) and examined individually for any disturbances with a probability (Equation 5.17) of 10^{-6} , as the number of independent components in each sample is 1.6×10^4 . The only such periodicity thus encountered was at the systematically induced telemetry disturbance and its harmonics. Tests were also run with simulated periodicities inserted with Poisson

counting statistics to assure the validity of the upper limits.

As the probability thresholds in Table 5.2 were actually obtained directly from the variance of the Fourier amplitudes in each trial, a further consistency check was the equivalence of the distribution with that calculated from Equation 5.17, i.e. the total number of events N calculated from the amplitude variance with the assumption of random data is in agreement with that actually observed. The artifact periodicity at 10.24 msec was not subtracted from the Table 5.2 data, which accounts for the slight excess in peaks for $p < .01$.

As each of the six Cas A Fourier decompositions are completely independent, they can be investigated for coincidences at probabilities much greater than 10^{-6} . The net probability ϕ for the number of successes S in a number of trials t is

$$\phi(s,t) = \frac{t!}{s!(t-s)!} p^s (1-p)^{t-s} \quad (5.33)$$

The overall probability distribution in each trial was consistent with that expected, but there was one period value for which ϕ was found to be statistically significant. At a frequency of $851.82 \pm .05$ Hz, a three-fold coincidence was obtained in the six trials at a probability threshold of 5×10^{-3} , yielding a net probability ϕ of 2.5×10^{-6} , which then corresponds to an overall probability of only .04 that the effect is a random artifact (as there are 1.6×10^4 such frequency components). In checking the phase consistency by beginning 4 seconds later, none of the five resultant 10.49 sec trials yielded any significant power (i.e. $p < .04$) at this frequency, suggesting that the apparent periodicity at 1.17 msec was accidental.

2. Spectral Analysis - First Order. From the 60 second observation of Cas A, 2450 background corrected events were observed in layer 1 of the 3° detector in the 2 to 12 keV band, and 193 background corrected events in the first xenon layer of the $1/2^\circ$ detector. The observed spectra are plotted in Figure 5.3, where the data from the 128 channels have been grouped into bins consistent with the detector resolution. Particular features to be observed in the spectra from both detectors are strong low-energy absorption and an enhancement in the intensity at 7 keV. Most of the low energy absorption in the $1/2^\circ$ detector is due to the helium/propane first layer. As the statistics of the $1/2^\circ$ detector are poor compared to those of the 3° detector, only the results from the latter will be presented.

Assuming a synchrotron source mechanism with a power law X-ray spectrum and folding it through the detector response function did not yield an acceptable fit, as noted in Table 5.3 as a function of χ^2 per degree of freedom. The primary reason for the rejection of a power law X-ray spectrum over the entire energy band was the enhancement in the spectrum at 7 keV. Restricting the fit to above and below this feature did give an acceptable fit. In all cases, Monte Carlo techniques are used to determine the power law indices; the computed spectra are then normalized to the observed spectra over the region of interest.

Assuming a thermal bremsstrahlung model with an exponential spectrum and folding it through the response function also yielded an acceptable fit only when the region of the spectrum around 7 keV was omitted. For both the synchrotron and thermal models, a constant interstellar absorption due to the composition of elements in Table 5.1 and an atomic

hydrogen abundance of $1 \times 10^{22}/\text{cm}^2$ was used. This estimate is consistent with the distance to Cas A and an interstellar density of $\sim 1 \text{ H atom}/\text{cm}^3$.

Attempts to explain the entire spectrum with various combinations of synchrotron and thermal models were also unsuccessful.

Interpolating the best fit power law and thermal spectra through the region of enhancement, one observes an excess centered at 6.5 keV, as shown in Figure 5.3, where both the thermal and power law model leave essentially the same residual. It is significant that this residual is centered near 6.5 keV, a region where the dominant K-shell transitions from Fe^{+25} and Fe^{+24} would be expected. Assuming that the residual is due to iron lines, the observed broadening is not likely to have resulted from electron scattering of the radiation in a compact thermal source as the magnitude of the emission feature in relation to the continuum is prohibitively high (Felten et al., 1972) for a thermal spectrum. Furthermore, no part of the observed spectrum could be fit with a thermal continuum with the high temperatures needed to account for the presence of iron lines (Tucker and Gould, 1966). This residual is probably due to electron cascades to the ground state in fast iron nuclei following charge exchange with neutral matter, as proposed by Silk and Steigman (1969).

If the interstellar region surrounding the remnant of Cas A is permeated with low energy cosmic rays of a few MeV/nucleon ejected by the supernova (Ramaty et al., 1971), high Z nuclei can be expected to acquire electrons from the medium via charge exchange with ambient neutral atoms. A substantial number of transitions to the ground state from higher excited states will result in 2p-1s transitions at

approximately 7.0 keV and 6.7 keV from H-type and He-type Fe, respectively. These lines will subsequently be Doppler shifted to a degree depending on the velocity of the emitting ion. The final distribution will be a composite of all contributing lines. Although the contribution from lower Z elements could be comparable, the main effect will occur below about 3 keV where the total intensity is approximately an order of magnitude greater than at 7 keV.

To test this model, the data were fit with a spectrum of the form

$$\frac{dN}{dE} = C_1 \left\{ E^{-\alpha} + C_2 \frac{1}{\sigma\sqrt{2\pi}} e^{-\frac{(E-6.9)^2}{2\sigma^2}} \right\} e^{-\chi\sigma_g} \quad (5.34)$$

where

$$\chi = \text{interstellar distance} = 1.4 \times 10^{22} \text{ H atoms/cm}^2,$$

$$\sigma_g = \text{interstellar absorption coefficient.}$$

Acceptable fits were obtained for $\sigma = 1.23 \pm .09$ keV, where the errors are those that cause χ^2 to increase by unity when the corresponding parameter alone is allowed to change. Setting

$$\sigma^2 = \sigma^2_{\text{intrinsic}} + \sigma^2_{\text{instrument}} \quad (5.35)$$

and substituting the measured detector resolution of $\sigma_{\text{instrument}} = .54$ keV, one obtains $\sigma_{\text{intrinsic}} = 1.1$ keV. Assuming that the 6.7 and 7.0 keV lines contribute equally, single lines at the source are broadened by about 33%, corresponding to a particle energy of 13 MeV/nucleon.

3. Spectral Analysis - Charge Exchange. It appears from Equation 5.34 that the idea of charge exchange proposed by Silk and Steigman (1969) has merit, but also, great complication. Not only must the remaining components of the supernova ejecta be considered, but also

non thermal bremsstrahlung. In non thermal bremsstrahlung, the non relativistic nuclei disturb the ambient electrons, such that in the rest frame of the nucleus, the problem is simply that of an electron moving through and being deflected by the electrostatic field of the nucleus.

Assuming that the nuclei expelled from the remnant have undergone multiple collisions with the intergalactic medium, one can assume a model where the nuclei have taken on an equilibrium charge distribution. Pierce and Blaun (1968) and Betz (1972) give an expression for the effective charge of this equilibrium charge distribution

$$Z_{eff} = Z \left(1 - e^{-1.25 \beta Z^{-2/3}} \right), \quad (5.36)$$

and point out that this expression is valid for all ions interacting with all absorbers, within the errors of experiments.

Individual equilibrium charge distributions consistent with Equation 5.36 are presented by Allison (1958) for H and He ions, by Nikolaev et al. (1961) for light ions with $2 \leq Z \leq 18$, and by Heckman et al. (1963) for C, N, O, Ne, and A. Defining ϕ_i as the fraction of the total ion beam in a particular charge state, Heckman et al. (1963) point out that the ratios of these fractions, ϕ_Z / ϕ_{Z-1} , ϕ_{Z-1} / ϕ_{Z-2} , ϕ_{Z-2} / ϕ_{Z-3} , etc. for all of their data follow universal curves, one curve for each particular ratio, when plotted as a function of

$$137 \beta (Z - .62)^{.70} \quad \text{which is essentially the same as Equation 5.36.}$$

Using these same "universal curves" and computing the charge distribution for the higher Z elements (i.e., iron and nickel), these computed distributions are consistent to within approximately 1 percent

with the effective equilibrium charge of Equation 5.36, and consequently, these "universal curves" are used to define the equilibrium charge distribution for all elements discussed here.

As the charge exchange process allows capture into all m states of the ion, decays from different states to the ground state will yield different energy lines of various intensities depending on the capture state and decay mode of the excited ion. Bates and Dalgarno (1953) and Hiskes (1965) have computed cross sections for hydrogen atom-hydrogen ion charge exchange and found that for high energies ($E \gtrsim 1 \text{ MeV/nucleon}$) for a given m the low angular momentum states predominate and for lower energies the high angular momentum states predominate, particularly for low values of m . To simplify calculations, it is assumed that charge exchange cross sections are independent of angular momentum state, and are as presented by Nikolaev et al (1961). The difference between the assumption that charge exchange takes place with equal probability in all angular momentum states and the assumption that charge exchange takes place only in the S states is not expected to be significant for determination of line energies and intensities.

In the decay of the excited ions, only transitions down to the 1s state for ions with $Z \geq 12$ are expected to contribute photons above 1.5 keV. For hydrogen-like ions, Bethe and Salpeter (1957) present tables for transition probabilities from the excited states to the ground state. Assuming charge exchange to be independent of the capture angular momentum state, application of the transition probabilities results in approximately 60 percent of the decays going through the 2p-1s transition, for all m , the remainder of the decays going through

np-1s transitions and some ending up in the metastable 2s state. In the calculation, probabilities for decay through various modes were calculated separately for up to the $m = 5$ state. For $m \geq 6$, the results for $m = 5$ were used, and are not expected to contribute more than 4% inaccuracy in energy, and a small fraction of this in intensity.

For the helium-like ions, oscillator strengths computed by Chapman (1969) were used to determine transition probabilities for states up to $m = 4$. For $m \geq 5$, the results for the $m = 4$ state were used.

Accurate decay energies for high Z hydrogen-like ions can be computed from the expressions of Penny (1930) and are presented in tabular form by Garcia and Mack (1965). Decay energies for some helium-like ions are presented by Chapman (1969), Ermolaev et al. (1972) and Felten et al. (1972) and can also be computed with great accuracy using the Hartree-Fock parameters of Froese (1966).

The problem of charge exchange was extensively studied by Schiff (1954) for the case of alpha particles and singly ionized helium passing through hydrogen and helium. The electron capture cross section in the first Born approximation for capture into a state of principle quantum number m is

$$\sigma_m = \frac{m^2 2^{18} (zz'/m)^5 \pi a_0^2 S^8}{5 [S^2 + (z - z'/m)^2]^5 [S^2 + (z + z'/m)^2]^5} \quad (5.37)$$

where

$$S = v/v_0,$$

v = velocity of ion in frame of atom,

v_0 = characteristic velocity of an electron in the first

Bohr orbit of hydrogen,

a_0 = radius of the first Bohr orbit of hydrogen,

Z = atomic number of atom giving up the electron,

Z' = atomic number of ion capturing the electron.

Nikolaev (1965) studied the similar problem of heavier ion gasses and noted that Equation 5.37 holds also for the heavier ions provided $v \gtrsim Z v_0$. Experiments by Reynolds et al. (1955), Nikolaev et al. (1961) and MacDonald and Martin (1971) show agreement with the observations of Nikolaev (1965). The computed cross sections fall significantly below experimental values in cases of high Z ions charge exchanging with even higher Z atoms, for low velocities but velocities still above $Z v_0$. Due to the small relative concentration of these ions and atoms, this difference is not expected to affect the calculations.

It is assumed that the atoms in the interstellar gas which are ionized by charge exchange have the same relative abundances listed in Table 5.1. For the composition of the cosmic ray nuclei leaving the remnants, it is assumed that relative abundances of low energy galactic cosmic rays are a good representation. Utilizing the results of the Comstock et al. (1969), Shapiro and Silverberg (1970), Price (1971), and Cartwright et al. (1971), the distribution of low energy cosmic rays used in the present calculation are shown in Table 5.5.

The line emission from the excited ions after charge exchange has taken place will be Doppler broadened. Assuming the excited ions to have an isotropic direction distribution, the differential energy spectrum due to a single line will be

$$\frac{dN}{dE} = \frac{E_0}{2\gamma\beta E^2} \quad (5.38)$$

where

$$E_0 \sqrt{\frac{1-\beta}{1+\beta}} \leq E \leq E_0 \sqrt{\frac{1+\beta}{1-\beta}} \quad (5.39)$$

and where

E_0 = the energy of the line ,

$\beta = v/c$ where v is the velocity of the excited ion
after charge exchange ,

$$\gamma = (1 - \beta^2)^{-1/2}$$

Due to the discontinuous nature of the Doppler broadening, the differential photon energy spectrum for charge exchange cannot be written directly. Defining Q as the number of photons emitted per capturing ion of charge Z' in a line corresponding to the t transition in an i electron atom for ions of energy E to $E + \Delta E$,

$$\frac{\Delta Q(E, Z', t, i)}{\Delta E} = \sum_{Z=1}^{\infty} m_Z \sum_{m=Z}^{\infty} p_t(m) \tilde{p}_{i-1}(E) \sigma_m(E, Z', Z) \beta c N(E), \quad (5.40)$$

in units of (photons/cm²sec MeV/nucleon), where

$\sigma_m(E, Z', Z)$ = cross section of Equation 5.37,

$p_t(m)$ = probability that a particular transition t will take
take place after capture into the m state,

$\tilde{p}_{i-1}(E)$ = probability that the ion about to capture the electron
will have $i-1$ electrons,

βc = velocity of capturing ion,

$N(E)$ = spectral number density of capturing ions (ions/cm³ MeV/
nucleon),

Z = charge of atoms of interstellar medium,

m_Z = density of atoms Z in interstellar medium.

Defining an isotropic spectral number intensity of the capturing ions as

$$J(E) = \beta c N(E) / 4\pi = A E^{-\ell} \quad (5.41)$$

in units (ions/cm²sec ster MeV/nucleon),

$$Q(E) = \frac{\Delta Q}{\Delta E} \Delta E = 4\pi A E^{-\ell} \tilde{\rho}_{i-1}(E) \sum_{z=1}^{\infty} m_z \sum_{m=2}^{\infty} p_t(m) \sigma_m(E, z', z) \quad (5.42)$$

with units (photons/cm³sec). Applying Doppler broadening, the differential photon energy spectrum in units (photons/cm³sec keV) is

$$\frac{dN'}{dE'}(E, z', t, \ell) = \frac{E_0}{2\gamma\beta E'^2} Q(E) \quad (5.43)$$

where the relativistic functions β and γ refer to the ion and E_0 is the energy of the line corresponding to the t transition, in keV.

Expanding the charge exchange concept to the other elements requires the addition of cosmic ray (non thermal) bremsstrahlung (discussed in Chapter II) since this contribution can be orders of magnitude stronger than emission from the charge exchange process under certain conditions. The charge exchange-non thermal bremsstrahlung model will be referred to as the CXB model.

Assuming a power law cosmic ray energy spectrum (as power law spectra are frequently observed in nature), and a low energy cut off consistent with collisional stopping in the form

$$N(E) = k E^{-\ell} \quad , \quad E > E_0 \frac{Z^2}{A} \\ = 0 \quad , \quad E < E_0 \frac{Z^2}{A} \quad (5.44)$$

(where E_0 is the same for all nuclei), did not yield acceptable fits over the entire band. However, a wide range of acceptable fits

resulted if only the data above 4 keV were considered, as sketched in Figure 5.4 (cosmic ray power law index vs. spectral cut off, in keV, for iron), where the surface encloses the region of acceptable fits and the line represents values of minimum χ^2 . The same sketch for the data from the 1/2° detector points out the inability of this data to discriminate between models.

In a model where reimplosion of a small mass fraction occurs following a supernova, Ramaty et al. (1971) suggest a number spectrum of nuclei of mass number A as

$$\begin{aligned} N(E) &= \frac{k}{A} \sqrt{\frac{E}{E_0^3}} \quad , E < E_0 \\ &= \frac{k}{A} \frac{E_0^2}{E^3} \quad , E_0 < E \end{aligned} \quad (5.45)$$

where

k = constant,

E_0 = transition energy, assumed to be the same for all nuclei.

Folding this model through the response function over various energy bands yielded no acceptable fits.

Assuming a monochromatic cosmic ray distribution also provided unacceptable fits.

The prime reason for the failure of the CXB model with a power law cosmic ray distribution was the fact that low energy predictions were significantly less than those observed. It is not unrealistic to assume low energy contributions, possibly from the core or perhaps even the knots in the nebula and thus, to combine the CXB model with steep synchrotron or low temperature thermal models. As a representative case, taking the CXB model with a cosmic ray power law distribution of $E^{-2.6}$

and a cutoff for iron at 17 MeV/nucleon and combining it with synchrotron and low temperature thermal models yielded acceptable fits, as tabulated in Table 5.3. The X-ray power law continuum gives a lower bound on the index. The low temperature thermal continuum model does specify a temperature of $kT = .48^{+.16}_{-.08}$ keV, with an interstellar absorption of $(1.7^{+.5}_{-.7} \times 10^{22} \text{ H atoms/cm}^2)$. Furthermore, repeated fits showed the low energy iron cut off to be bounded, at a value of 17^{+5}_{-3} MeV/nucleon, for the $E^{-2.6}$ cosmic ray power law. This fit is sketched through the data in Figure 5.2, for both the 3° detector and $1/2^\circ$ detector (with renormalization).

From Figure 5.4 it is clear that many values of a cosmic ray power law index in the CXB model exist for which an acceptable fit is likely, as this model fit the data above 4 keV for a wide range of index and iron cut off energy. A two component model, however, is necessary to describe the Cas A data. Single power law or thermal continuum models, or combinations of these will not adequately describe the spectrum.

As the results from Cas A and Tycho exhibit commonality, they will be discussed together.

C. Tycho Observation

1. Temporal Analysis. The temporal analyses for Tycho were conducted in the same manner as those for Cas A. For Tycho, there were 3684 non zero events in the 100 second exposure, approximately 50% from the source. Upper limits to any periodic modulation in the data are shown in Figure 5.1.

2. Spectral Analysis. The 100 second observation of Tycho yielded 967 background corrected events in the 3° detector and a scant 50 background corrected events in the $1/2^\circ$ detector. The observed spectra appear in Figure 5.5 where again the data have been grouped into bins consistent with the detector resolution. The particular characteristics of these spectra are an extremely steep low energy continuum, with an enhancement at approximately 7 keV. As this feature appeared in the same place as in the Cas A data, it is necessary to point out here that this is not instrumental; this has been verified by detailed instrument calibrations. Furthermore, identical counters flown on previous rocket flights did not observe the feature. Due to the poor statistics in the $1/2^\circ$ detector, only the results from the 3° detector will be presented and discussed.

Following the identical procedure as for Cas A, synchrotron and thermal models were folded through the response function of the detector, with 1×10^{22} H atoms/cm² interstellar absorption. As there does not appear to be a contribution from the continuum above 7 keV, separate trial fits were made for the data below the feature. No acceptable single component power law or exponential continuum model was obtained, as listed in Table 5.4. Combinations of power laws and exponentials failed as for Cas A.

The sharp feature in this data will result in acceptable fits from the CXB model above 4 keV for cosmic ray distributions as power law, monochromatic, and reimplosion; no acceptable fits are obtainable over the entire energy range. Figure 5.6 shows the contours of acceptable fits as a function of cosmic ray power law index and iron cut off energy.

Considering a combination of the CXB model with a cosmic ray power law distribution of $E^{-2.6}$, an iron cut off at 7.3 MeV/nucleon, and a synchrotron continuum resulted in no acceptable fits for synchrotron power law indices less than 9.6. With a thermal continuum, not only is the temperature once again bounded but also the iron cut off, as shown in Table 5.4. The fits in Figure 5.5 represent the model with the thermal continuum.

Again it should be pointed out that a wide range of acceptable fits as a function of cosmic ray power law index are possible, where here only the index of 2.6 was tested.

D. Discussion of Cas A and Tycho

As Cas A and Tycho are both supernova remnants and exhibit similar characteristics, they will be discussed together. The upper limits displayed in Figure 5.1 for the X-ray periodicity from Cas A and Tycho are considerably lower than those previously reported. Gorenstein et al. (1970) placed upper limits of 15% and 19% on Cas A and Tycho, respectively, but only in the period range 8-35 msec and for $\beta = 0.1$ (the present limits for $\beta = 0.1$ at 99% confidence are 3.9% and 8.4%). Over the range 1 msec-10 sec, the 99% confidence limits are 8.9% and 19.5% for $\beta > 0.35$, and appropriately lower for smaller β .

Considering a specific pulsar emission model, such as the one proposed by Bertotti et al. (1969), rotating neutron stars within the remnants are not denied by the above upper limits. Even if the earth is within the hypothesized pulsar "beam", the X-ray pulsed fraction could easily be less than 1%, particularly if the rotation period is

longer than that of the Crab pulsar (Holt and Ramaty, 1970; Pacini, 1971).

The observed spectra from Cas A and Tycho exclude simple one component models, requiring at least 2 components, as shown. The previous observation of Cas A and Tycho by Gorenstein et al. (1970) also suggests this complex spectral nature, while Burginyon et al. (1973) do not have the resolution or statistics to observe the feature. Indeed, for Cas A, where good statistics were available, Gorenstein et al. (1970) found that acceptable χ^2 fits based on a single component power law or thermal model plus interstellar absorption were not possible.

In order to demonstrate the relative agreement between the results of this experiment and those of Gorenstein et al. (1970), it is necessary to compute inferred incident spectra, in the form

$$S(E) = N_{\text{OBS}}(E) \frac{S'(E)}{N_{\text{CALC}}(E)} \quad (5.46)$$

where

N_{OBS} = observed spectrum,

S' = best fit model spectrum,



N_{CALC} = spectrum of best fit model folded through the detector response function.

It must be understood here that this expression is only valid when the inverse of the response function is unique, which it usually is not, particularly when the detector is a complex proportional counter as in this experiment. The results however may still be accurate to within a few percent and Figure 5.7 presents the inferred incident spectrum of Cas A as observed by this experiment and that of Gorenstein et al.

(1970). It is immediately apparent that both experiments observed the steep continuum plus the feature at 7 keV, as the data points track each other above 2 keV. Less satisfactory agreement is observed in the spectrum from Tycho, shown in Figure 5.8, where the data of Gorenstein et al. (1970) shows no evidence for a dip in the spectrum at 4.5 keV. The observed flux in the 2 to 10 keV band is in agreement, in both experiments and for both sources, with the results quoted in the Uhuru catalogue (Giacconi et al., 1973).

Observed cosmic ray abundances were used in the calculation of the radiation due to charge exchange and non thermal bremsstrahlung, the contribution from each of these elements being tabulated in Table 5.5 for the fit to the Cas A data, where a cosmic ray power law of $E^{-2.6}$ and an iron cut off energy of 17 MeV/nucleon were used. Interstellar absorption must still be added to this data before folding it through the detector response function. The spectra generated by each of these components are plotted in Figure 5.9 where the numbers refer to the atomic numbers of the contributing elements.

It is to be noted from Figure 5.9 that the non thermal bremsstrahlung (represented by the power laws) is primarily due to hydrogen and helium. As the breaks in these spectra will exceed 2 keV at an iron cut off of 45 MeV/nucleon, the non thermal bremsstrahlung is essentially independent of the iron cut off. The strengths of the Doppler broadened lines decrease slightly with an increase in the cosmic ray power law index and decrease rapidly with an increase in the cut off energy. The width of these lines also increase with cut off energy as high intensity low energy cosmic rays are required for narrow lines.



Many of the elements contribute negligible amounts to the spectrum, typically elements with $Z > 26$, and the odd Z elements with $13 \leq Z \leq 25$, and thus these elements can be neglected in further analyses. The relative amounts of hydrogen, helium, iron, silicon, magnesium, titanium, calcium and chromium are important. Removing titanium from the spectrum, for example, will produce a deeper trough which will give the iron line a sharper appearance.

There exists considerable question as to which set of relative abundances to use to describe the corpuscular radiation from Cas A and Tycho. The computed primordial cosmic ray spectrum of Shapiro et al. (1971) has hydrogen, helium, carbon and oxygen abundances similar to the observed cosmic ray abundances, approximately twice as much silicon and iron, and no chromium. These abundances are also listed in Table 5.5. In the supernova model of Colgate (1971), the explosion is believed to take place in matter that is either carbon or oxygen, or the products of carbon and oxygen burning. The detonation or sudden shock heating of this material is described as quasi-equilibrium silicon burning, the final composition being one third iron and two thirds silicon, with various elements from helium to iron providing small fractions. Hydrogen is produced only as a result of all spallation processes. Optical studies by Peimbert and van der Bergh (1971) reveal unusually large abundances of medium and heavy elements and infer that the quasi-stationary flocculi were formed by material ejected from the outer layers before the supernova. Casse (1973) proposes that the principle nucleus resulting from explosive silicon burning is Ni^{56} which, when completely ionized, is believed to have a half life of 10^5 to 10^6 years.

If one requires the primordial cosmic ray spectrum to describe the ejecta from Cas A and Tycho, the non thermal bremsstrahlung spectrum will not change. Absence of elements with $21 \leq Z \leq 25$ and the increased intensity of iron generate an intense line feature as sketched by a dashed line in Figure 5.9. Folding this composition through the detector response functions as before yielded no acceptable fits; the iron line feature is too strong.

Several possible mechanisms exist for the collisional cut off of the cosmic ray power law at low energies. A power law distribution of $E^{-2.6}$ of iron nuclei passing through typically $.3 \text{ gm/cm}^2$ will be sharply reduced such that the resultant spectrum can be approximated by the same power law above approximately 17 MeV/nucleon and a flat spectrum below. In this amount of matter, the iron nuclei will have typically 3000 charge exchange collisions, more than adequate to develop an equilibrium charge distribution. Furthermore, in the reimplosion model of Ramaty et al. (1971), the ejecta particles are already steeply cut off at low energies, as shown in Equation 5.45.

In comparing the best models of Cas A and Tycho with radio observations as summarized by Woltjer (1972), those with a synchrotron continuum can be eliminated. Assuming the power law photon spectra to be due to a distribution of electrons emitting by synchrotron radiation in the vicinity of the core, Tucker (1971) expects a break in the electromagnetic spectrum by a factor of 1/2 in the vicinity of 0.1 eV. The observed spectral breaks are typically 2.6 and 6.0 for Cas A and Tycho, respectively. Also, the breaks in the spectra occur at 1000 eV instead of the predicted 0.1 eV. Furthermore, the intensity of Cas A and Tycho at 1.5 keV exceeds the extrapolated radio intensities, as

shown in Figure 5.10.

A possible explanation of the continuum emission from Cas A is thermal bremsstrahlung. From Equation 2.31, the power radiated in units of keV/sec from a plasma where $h\nu \gg kT$ (valid since $kT \approx .5$ keV) in the 2 to 12 keV band is

$$\begin{aligned} E &= \int_2^{12} h\nu \frac{dq}{dh\nu} dh\nu \\ &= 3.93 \times 10^{-17} m_o m_e V, \end{aligned} \quad (5.47)$$

where

V = volume of emission region in cm^3 ,

m_o = density of protons in cm^{-3} (contributions from other ions are considered negligible)

m_e = electron density in cm^{-3} .

The observed thermal emission was estimated to be $.694 \text{ keV/cm}^2\text{sec}$.

Assuming a distance to Cas A of 2.8 kpc (van den Bergh, 1971), one finds that

$$m_e m_o V = 2.3 \times 10^{58} \quad (5.48)$$

Assuming charge equilibrium and the cosmic ray abundances, $m_e \approx 1.18 m_o$, one finds that

$$m_e^2 V = 2 \times 10^{58} \quad (5.49)$$

The diameter of the HII region around Cas A is observed to be 6 pc, while the nebular region extends only as far as 1.7 pc. Fabian et al. (1973) find from observations by the OAO-C satellite that the emission region can best be approximated by an annulus with outer and inner diameters of 5.5 and 2 pc, respectively. Assuming the thermal continuum to be due to the annulus (essentially the HII region) or the nebular

region, one finds electron densities of $1.4/\text{cm}^3$ and $5.7/\text{cm}^3$. The electron density for the HII region is about an order of magnitude less than that estimated by van den Bergh (1971).

Assuming for the best Cas A model that the iron in the supernova ejecta can be represented by a monochromatic line at 17 MeV/nucleon, Table 5.6 presents the charge exchange cross sections for the iron impinging on interstellar matter. The total cross section of $1.71 \times 10^{-21} \text{ cm}^2/\text{H atom}$ suggests a time for a single collision of $4800/m_H$ years, where m_H is the density in cm^{-3} of hydrogen in the interstellar medium. From the data, iron line emission of 2.83×10^{43} photons/sec is inferred. Assuming one photon to be generated per iron nucleus, the total number of iron nuclei is $N_{Fe} = 4.29 \times 10^{54}/m_H$, and assuming the observed cosmic ray abundances, the number of protons in the ejecta is $N_H = 8.94 \times 10^{57}/m_H$. The total mass of the ejecta then becomes $\sim 7.5 M_\odot/m_H$ with a total energy of $2.44 \times 10^{53}/m_H$ ergs. A lower limit to the energy emitted during the supernova explosion in the UV region of 10^{50} ergs has been estimated by Peimbert and van den Bergh (1971).

Protons are primarily responsible for the cosmic ray produced ionization in the HII region. The energy loss rate of a proton of energy E in MeV/nucleon in neutral hydrogen is given by Ramaty et al. (1971) as

$$-\frac{dE}{dt} \approx 1.46 \times 10^{-12} m_H E^{-.3} \text{ MeV/sec.} \quad (5.50)$$

For an iron cut off energy at 17 MeV/nucleon, the cut off energy of protons will be 1.4 MeV/nucleon. Assuming the collisional cut off estimated from the model fits to represent the energy of initial ejecta

particles which have been completely removed from the beam and using the time of 9.6×10^9 seconds for the age of Cas A, one finds that the necessary neutral hydrogen density is $n_H \approx 136/\text{cm}^2$ and $n_e \approx 161/\text{cm}^2$.

The average electron density may also be written as

$$n_e = \frac{N_H \frac{dE}{dt} T}{E_p V} \quad (5.51)$$

where

T = age of Cas A,

E_p = 36 eV, the energy needed for the creation of an ion pair

V = volume of HII region.

Substituting Equation 5.50 and again using 1.4 MeV/nucleon for hydrogen, the electron density becomes $n_e \approx 290/\text{cm}^3$.

This discrepancy in the electron density is primarily due to a lack of knowledge of the composition and energy spectrum of particles leaving the supernova. The possibility of protons of energy less than 10 MeV/nucleon in cosmic rays has not yet been refuted (Urch and Gleeson, 1972). Information on the spectra of cosmic ray particles below 80 to 160 MeV/nucleon is unavailable due to the effects of solar modulation.

It does appear though, that the necessary thermal continuum for this model of Cas A does not arise from the HII region or the nebular region as the electron densities are too large by a approximately an order of magnitude. The large values of electron density inferred for the HII region suggest that much of the energy is going into expansion and heating rather than ionization.

For the data from Tycho, contributions to the spectrum from a thermal continuum, non thermal bremsstrahlung, and charge exchange

are .194, .00686, and .269, respectively, in units of $\text{keV}/\text{cm}^2\text{sec}$ for the 2 to 12 keV band. Here the charge exchange completely dominates the model, even at low energies, where now the elements $12 \leq Z \leq 20$ provide for most of the "continuum" radiation.

There is no HII region or nebulosity associated with Tycho, although filaments are observed and these have proper motions of typically .22"/year (van den Bergh, 1971). Assuming, (1) the expansion to have been constant since the supernova explosion in 1572, (2) the shell to be completely circular (Baldwin, 1967), and (3) a distance of 3 kpc (Minkowski, 1964; Woltjer, 1964), the radius of expansion is approximately 1.3 pc. The observed thermal continuum then requires an electron density of $n_e \approx 5.0/\text{cm}^3$, in agreement with the theoretical estimates of Shklovsky (1972). Shklovsky (1972) however, points out that this is inconsistent as the supernova explosion took place in a region of low density, typically $n_e \leq 0.1 \text{ cm}^{-3}$. Perhaps the observed thermal continuum is due to the dissipation of the rotational energy of a neutron star in the core of the remnant. Failure to detect periodic modulation in the X-ray flux does not rule this out.

The total cross section of 7 MeV/nucleon iron is $5.0 \times 10^{-21} \text{ cm}^2/\text{H atom}$, suggesting a time for a single collision of $1740/m_H$ years. The observation infers the generation of 5.43×10^{43} photons/sec in the iron line from which the numbers of iron nuclei and protons become $N_{\text{Fe}} = 2.98 \times 10^{54}/m_H$ and $N_H = 6.21 \times 10^{57}/m_H$. The total mass ejected becomes $\sim 5.2 M_\odot/m_H$ with a total energy of $6.9 \times 10^{52}/m_H$ ergs. Assuming an age of 400 years for Tycho, the electron density from Equation 5.51 then becomes $13900/\text{cm}^3$, roughly 5 orders of magnitude larger than expected based on optical studies. This excess can only

be accounted for by severely limiting the amount of hydrogen expelled from Tycho, and would thus support the theory of Colgate (1971) where all the hydrogen nuclei are the results of spallation, and only high Z materials make up the ejecta. In the model of a monochromatic cosmic ray composition for the ejecta, eliminating hydrogen and helium will have the effect of enhancing the line features, making lesser amounts of iron necessary. Assuming just iron and rewriting Equation 5.50 as

$$-\frac{dE}{dt} \cong 1.46 \times 10^{-12} M_H \frac{Z^2}{A} E^{-.3} \text{ MeV/sec.} \quad (5.52)$$

the resulting required electron density in the region in the remnant of Tycho is $n_e \approx 38/\text{cm}^3$. Reducing the hydrogen content allows a reduction in this value of n_e such that realistic densities are obtainable.

The Crab Nebula is roughly 3 times as old as Cas A and Tycho so that it too should be source of broad iron lines, if the three supernovae were similar events. The Crab X-ray spectrum has been extensively studied and, in the range of interest, shows no evidence of spectral features (Boldt et al., 1969). The line flux that has been inferred for Cas A would at most amount to 2% over the strong and flat Crab continuum, and should not be easily detectable.

E. Cyg X-1

1. Temporal Analysis. Only the three transits of Cyg X-1 during balloon flight 683-P at 0614, 0830 and 0925 UT provided sufficient data on which to do temporal analysis. Using the Cooley-Tukey harmonic analysis approach, the data were broken in 104.9 second samples (with .0095 HZ resolution) and examined individually for

disturbances with a probability of 10^{-6} , as was the case for Cas A and Tycho. There was no frequency which persisted with probability P of less than .01 from one sample to the next. Furthermore, the individual samples are consistent with random data as shown in Table 5.7, where the observed probabilities are for frequencies from .1 HZ to 156.25 HZ. The only significant periodicity observed occurred at a frequency of .025 HZ, the resonant frequency of the azimuthal motion of the gondola. Reanalysis of the data with 26.2 second samples also failed to show any Fourier amplitudes inconsistent with random data.

Each 104.9 second sample in this analysis contained approximately 5000 background events and up to approximately 2000 events from Cyg X-1, with a mean of roughly 1300 events. Consequently, an upper limit to the pulsed fraction at any specific frequency in the .1 to 156 HZ band is 18%, or for a true periodicity at any frequency whatsoever, 33%.

While good estimates on the aspect of the detector exist, the rapid changes in count rate as the detector crosses back and forth over the source prevent a meaningful study of non periodic variations. Figure 5.11 shows the number of observed counts per effective exposure in the 13 to 33 keV band, and the large fluctuations late in the flight, even though of questionable statistical significance, may be characteristic of aspect solution errors.

2. Spectral Analysis. The same three passes of Cyg X-1 which were examined for periodicities contain sufficient data for spectral analysis. In each of these cases, 1.5 units of background data were taken before and after each transit, for each unit of source data.

The only exception to this is the 521 second observation where a transit of Cyg X-3 followed closely behind. In this case, more background data was taken from before transit.

In all cases, the background data rate was approximately .178 events per data word, and the average due to Cyg X-1 came to about .045 events per data word. This average value is sufficient to provide a good estimate on the amount of background data to subtract.

As was the case for the data from Cas A and Tycho, the data were grouped into bins consistent with the resolution of the detector, and data in the 5 to 60 keV band were compared to a model folded through the response function of the detector via the chi-square technique. It is to be noted here that even though the atmosphere absorbs all photons with energies less than approximately 15 keV, a strong contribution is obtained in the 5 to 15 keV band due to K-shell resonance escape resulting from incident photons of energy greater than 35 keV. In all cases, the data from all 7 layers of the detector were used.

Assuming a power law model and considering atmospheric absorption, acceptable χ^2 fits were obtained for all three transits, and are listed in Equations 5.53, 5.54 and 5.55, where the energy E is in keV and the differential energy spectrum has units of photons/cm²sec keV.

$$\frac{dN}{dE} = .229 \pm .011 E^{-1.30^{+0.66}_{-.62}}, \quad (5.53)$$

$$\frac{dN}{dE} = .0419 \pm .0020 E^{-0.84^{+0.41}_{-.37}}, \quad (5.54)$$

$$\frac{dN}{dE} = .207 \pm .009 E^{-1.22^{+0.06}_{-.05}}, \quad (5.55)$$

In all cases, the error bars on the power index correspond to a 90 percent confidence level. Error bars on the intensity correspond only to the uncertainty in the exposure as the computed spectrum was normalized to the observed data. The relatively small error bars on the power law index in Equation 5.55 do not suggest a good fit but merely point out that the minimum value of χ^2 was just barely acceptable. If one defines the error bars on the basis of a one sigma increase in χ^2 , new error bars of $\pm .25$ and $\pm .26$ are obtained.

Combining the data of all three passes into one, the resultant spectrum from Cyg X-1 is found to be

$$\frac{dN}{dE} = .169 \pm .010 E^{-1.15^{+.18}_{-.16}} \quad (5.56)$$

where the errors are as before. Figure 5.12 shows this combined data, all layers and all transits, and the best fit power law of Equation 5.56.

No thermal bremsstrahlung model with $kT < 500$ keV could be satisfactorily fit to the Cyg X-1 data. Due to the relatively flat spectrum observed using a power law model, it is expected that an exponential model will fit, but the necessary relativistic corrections void the simple exponential model.

3. Discussion. From initial observations, Cyg X-1 appeared very much like the Crab Nebula exhibiting a spectrum which appeared flat with a power law index of approximately 1.7. Several representative observations in the rocket and balloon observation range are presented in Figure 5.13. Recently however, the fluctuations observed by the different experimenters have become more obvious and

Dolan (1970) attempted to explain this variation using a binary model with a 2.8 day period. Analysis of Uhuru data over several source transits showed a periodicity of .073 seconds (Oda et al, 1971). Holt et al. (1971) found a double periodicity in the low energy X-ray at 0.290 and 1.1 seconds while Shulman et al. (1971) found no evidence for periodicity. A dynamic spectrum analysis by Oda et al. (1972) found that oscillations last typically for several seconds with the frequency drifting. No random periodicity has been observed in the hard X-ray band and this experiment proved to be no exception.

In studying the temporal variation of the X-ray data from the Uhuru satellite and comparing it to radio observations, Tananbaum (1972) noted a simultaneous change in the radio and X-ray intensity, supporting the identification of a variable radio source with the X-ray object. A previous correlation of a B0 supergiant which is a spectroscopic binary with a 5.6 day period had been made by Webster and Murdin (1972) and Bolton (1972). No 5.6 day periodicity is observed in the X-ray region.

The problem of variability of Cyg X-1 has been discussed in detail by Matteson (1971) who suggests a model where electron acceleration and heating is occurring and then stopping. This could typically happen at random times for matter infalling onto the neutron star or black hole partner of the binary pair. Matter infalling will first go into unstable orbits, thus yielding the short duration periodicities and a synchrotron type spectrum.

An additional observation of the Uhuru satellite was the steepening of the spectrum from what had been previously observed by other experimenters. At the other extreme, one has the flat spectrum of Matteson

(1971). The present observed spectrum is thus seen to be in agreement with previous results.

F. Cyg X-2

The accidental transit of Cyg X-2 during balloon flight 683-P for an effective exposure of 73.4 seconds yielded questionable evidence for hard X-ray emission. There is such an extremely small contribution above background that a spectrum cannot be constructed. In fact, in the 13.7 to 32.5 keV band, only 15.2 ± 24.7 counts are observed. Background observations for this pass come from immediately before to immediately after this transit and amount to approximately 3 times the source data. The present observation of Cyg X-2 sets a 3σ upper limit at 5×10^{-2} keV/cm²sec keV in the 14 to 33 keV band, roughly consistent with the 4.5σ upper limit at $\sim 3.6 \times 10^{-2}$ keV/cm²sec keV in the 25 to 50 keV due to Webber and Reinert (1970), an upper limit of $\sim 2.1 \times 10^{-3}$ keV/cm²sec keV in the 18 to 52 keV band by Rocchia et al. (1969), and a value of 1.8×10^{-2} keV/cm²sec keV in the 22 to 50 keV band from Matteson (1971). In the low energy X-ray band, Cyg X-2 is observed to be a thermal source with $kT \approx 3.5$ keV.

G. Cyg X-3

1. Observation. During balloon flight 683-P, there was a total of 76.5 seconds effective exposure to Cyg X-3, made up of three separate transits. Insufficient data existed for a meaningful spectrum but an excess over background of 82.4 ± 30.3 counts in the 13.7 to 32.5 keV

band was observed. Assuming a power law energy spectrum with normalization at 10 keV to .01 photons/cm²sec keV, this observation implies emission in the form $31.6 E^{-3.5^{+.5}_{-.4}}$ photons/cm²sec keV for an upper limit of 8.5×10^{-4} photons/cm²sec keV. A thermal spectrum normalized to the same point would require $kT = 6.7^{+1.3}_{-1.4}$. Background observations for each transit were taken for proportionally equal amounts of time before and after the transit. As these transits were all so swift and due to the oscillations in the guidance system, no temporal analysis could be conducted.

Figure 4.10 shows the results of balloon flight 696-P on August 31, 1973. From the figure, it is immediately apparent that there was no detectable emission from Cyg X-3 during this exposure. This is particularly obvious at those times where the detector was moved onto and off the source, with no observed change in intensity in the most sensitive energy band of the detector. To reduce systematic errors, source data during 6 regions of the flight were selected (labeled S1 through S6 on Fig. 4.10) along with equal amounts of background data (B1 through B6), the only criterion for corresponding source-background data being that they come from times of roughly the same latitude, altitude, and elevation angle. The results of this analysis are listed in Table 5.8, where source and background data correspond to the 13.7 to 32.5 keV energy band. The column of data under Δ is the number of sigma difference between source and background data. The columns E^{-4} and $E^{-2.3}$ correspond to power laws $100 E^{-4}$ and $2 E^{-2.3}$, the numbers indicating the number of events expected in the 13.7 to 32.5 keV energy band for each sample, after the power laws have been folded through the atmosphere and the detector. Lastly, the

σ column refers to the number of σ the E^{-4} data should be above background. An E^{-4} power law with 3.5×10^{-10} ergs/cm²sec in the 13.7 to 32.5 keV band is seen to be a 10 σ upper limit on the emission from Cyg X-3.

Limits can be put on the possibility of sudden high intensity flaring. Figure 4.10 presents the observed count rate in 5 minute bins. Requiring a 3 sigma effect, Figure 5.14 shows the pulse duration necessary for a single pulse with count rate λ , where λ_0 is the count rate of the non pulsed component.

A slightly less stringent upper limit can be set by studying the distribution of times between events. If one observes an event at some data word, the probability of seeing the next event after m data words is

$$\Delta P(m) = e^{-m\lambda} \lambda \Delta t \quad (5.57)$$

where Δt is the length of a data word. Figure 5.15 is a plot of the event spacing distribution for all of the Cyg X-3 source data (marked by the -) and all of the background data (corrected for different exposure times). Both the source and background data follow the same slope indicating the consistency of the source data with no evidence for hard X-ray emission from Cyg X-3.

Another dramatic demonstration of the consistency of the source data with background data is a study of the number of events occurring per frame of data, as plotted in Figure 5.16, for the data of the 6 source-background segments in the 15.6 to 40.4 keV band. For a data rate λ , one expects a distribution as

$$P(m) = \frac{60!}{(60-m)!m!} e^{-\lambda(1-m/60)} (1 - e^{-\lambda/60})^m \quad (5.58)$$

where m is the number of event words (non zero data words) per frame.

A significantly improved upper limit comes from a study of the distribution of the number of events per data word, as recorded by Scalar II in the telemetry frame. The distribution of events per data word for a particular data rate λ are given by Equations 3.11 and 3.12, and Figure 5.17 is a plot of this distribution showing that the source and background data overlap and are in excellent agreement with theory. The slight disagreement in the higher values of the scalar is due to noise in the telemetry.

Finally, using the expression for determining the pulsed fraction ξ for a disturbance of duration β (Equation 5.16) and assuming the data can be broken up into groups of 40 bins ($P = 40$), assuming the least sensitive case ($\beta = .5$) and requiring a 3σ effect, Equation 5.16 becomes

$$\frac{\xi}{\xi + 1} = \sqrt{\frac{27}{N}} \quad (5.59)$$

where N is the number of photons in the group. Relating this to an increase in count rate, from λ_0 to λ , one obtains

$$\frac{\lambda}{\lambda_0} = \frac{2}{\sqrt{N/27} - 1} + 1 \quad (5.60)$$

and considering the observed 10 cts/sec in the 15 to 30 keV band, no lower upper limit can be set, as shown in Figure 5.14. The results of all these analyses are also plotted in Figure 5.14.

2. Discussion. Cyg X-3 has been observed by several experimenters, and has shown considerable variation in the hard X-ray region (Rocchia et al., 1968; Matteson, 1971) while appearing relatively stable in the low energy X-rays (Gorenstein et al., 1967; MacGregor et

al. 1970; Bleach et al., 1971; Peterson et al., 1972). Figure 5.18 is a compilation of several of these results. The non detection on 30 August, 1972 is not due to observing Cyg X-3 during a null in its periodicity of 4.8 hours as observed in low energy X-rays by the Uhuru satellite (Parsignault et al., 1972), the Copernicus satellite (Sanford and Hawkins, 1972), and the OSO-7 satellite (Canizares et al. 1973) since Cyg X-3 was observed continuously for a period of 6 hours. Prior to this observation, the Uhuru satellite observed Cyg X-3 and found the intensity in the 2-6 keV band to be reduced by a factor of 5, four times the typical error (Parsignault et al., 1972).

Repeated radio observations by Hjellming et al. (1972) of a variable star within the Cyg X-3 location error box as determined by Uhuru show repeated fluctuations at 8085 MHz and 2695 MHz typical of variable thermal radio sources. The fact that this radio candidate for Cyg X-3 is strongest at high frequencies coupled with observed flare-like increases suggests that its source mechanism may be similar to radio binary stars.

During the August 30 observation, Hjellming (1972) provided simultaneous radio coverage and found that the radio candidate for Cyg X-3 was at the lowest level ever observed, .012 f.u., compared to the ambient 200 f.u. level previously reported. From 3 hours to 6 hours UT, the radio intensity at 3.7 cm rose to .040 f.u; approximately one hour later, the intensity at 11.1 cm also increased, to approximately .025 f.u., typical of the many small flares of the past. There was no evidence of emission from Cyg X-3 during this time in the hard X-ray band.

In a model of solar radio and X-ray flares discussed by Holt and Ramaty (1969), hard X-rays and high frequency radio waves have the same temporal profile, typically on the time scales of tens of minutes. Low energy X-rays and low frequency radio emission increase in intensity slowly and correspondingly decay at a slower rate. The small flare on August 31 did not bring the radio candidate to its normal level and consequently at this low intensity, it is not surprising that the X-ray emission did not increase. The fact that the Uhuru satellite did not observe a sharp increase on September 2, 1972 during the giant radio outburst in the Cyg X-3 area (Gregory et al., 1972) does not exclude this model because of the satellite's rotational and orbital dynamics. The origin of these flares is understood to be an accretion model in which matter falls onto the small member of the binary pair at random intervals.

CHAPTER VI

SUMMARY

A sounding rocket observation of the supernova remnants Cas A and Tycho with multilayer multianode proportional counters on May 19, 1972 observed no 2 to 10 keV periodic emission from Cas A or Tycho in the period range of .0064 to 13.1 seconds. 99% confidence upper limits to the pulsed fraction of 8.9 and 19.5 percent are deduced for Cas A and Tycho, respectively, with considerably lower limits for pulse duty cycles of less than 35 percent.

The spectra of Cas A and Tycho exhibited the complex nature previously observed, allowing no acceptable single component synchrotron or thermal bremsstrahlung models, nor combinations of these. The spectra were found to be extremely steep with a broad emission feature at 6.5 to 7 keV, the region where one would expect the Fe^{+25} and Fe^{+24} characteristic lines. Limiting the spectral fits to regions above and below this feature required the elimination of the synchrotron model as the power law indices would be more than .5 greater than the power law indices observed in the radio band and also, the absolute intensity of Cas A and Tycho exceed the extrapolated radio intensities. Models for thermal bremsstrahlung over this same limited region of data suggest temperatures inadequate to produce the emission feature observed.

In an effort to explain this emission feature in the Cas A and Tycho spectra, a model was developed in which it was assumed that (1) the supernovae ejecta are similar to cosmic rays with a power law number

distribution, (2) the relative abundances of the ejecta components are the same as those for the observed cosmic rays, (3) the ejecta number distributions are cut off at low energies by a collisional process, the cut off energy going as Z^2/A , (4) the ejecta nuclei interact with the interstellar medium via charge exchange and non thermal bremsstrahlung.

For Cas A, this charge-exchange and non thermal bremsstrahlung model provided acceptable fits to the data for an iron low energy cut off at 17 MeV/nucleon, and an additional thermal continuum at $kT = .5$ keV. The low energy component of the spectrum could also be explained by an extremely steep power law spectrum and high interstellar absorption, but this synchrotron model must be rejected for the same reasons previously mentioned. The inferred thermal bremsstrahlung is inadequate to produce the observed HII region necessitating the charge exchange/non thermal bremsstrahlung component to be the source of the ionization.

An identical model was also found to fit the data from Tycho, where an iron low energy cut off of 7 MeV/nucleon and a low energy thermal continuum at $kT = .38$ keV provide the best acceptable fit. An inferred excess electron density can be accounted for by a model with little or no proton component in the ejecta.

Hard X-ray observations of Cyg X-1, Cyg X-2 and Cyg X-3 were made in a series of 4 balloon flights with a 600 cm^2 multilayer-multianode xenon filled proportional counter, identical in principle to the rocket borne experiments. On June 19, 1972, Cyg X-1 was observed for short periods of time during a 6 hour flight for a total exposure of approximately 1000 seconds. Cyg X-1 was found to exhibit no periodicities in the 15 to 60 keV energy band for frequencies from 1 to 156 Hz with 99% confidence upper limits to the pulsed fraction of 18%. Spectral analysis

performed on the three longest duration exposures suggest power law spectra consistent with the expression $.17E^{-1.15}$ photons/cm²sec keV deduced from all of the data combined. Exponential spectra (thermal bremsstrahlung model) can be rejected on the basis of these data. The observed flux is roughly consistent with the results of previous experiments. Rapid transits of Cyg X-2 and Cyg X-3 on June 19, 1972 suggested an emission consistent with previous observations.

An experiment to observe Cyg X-3 on August 31, 1972 found no detectable emission from Cyg X-3 with 10σ upper limits in the 14 to 33 keV band placing the intensity a factor of 20 below previous observations at a level of 3.5×10^{-10} ergs/cm²sec. Detailed analysis of the detector response as a function of time during this flight provided no evidence for a sudden short duration X-ray bursts. Simultaneous radio observations of Cyg X-3 at 3.7 cm did notice a small flare rising from .012 to .040 flux units during the middle of this flight, with no corresponding increase in the X-ray intensity, which was entirely consistent with background data.

APPENDIX

STAR FIELD ANALYSIS

Aspect information on the orientation of the balloon and rocket detectors was obtained by hard mounting Nikon F cameras with 50 mm f1.4 lenses to the experiment and shooting pictures of the night sky. In the rocket experiment, two cameras alternated taking 2.62 second exposures with a single 2.62 second pause in the cycle (Birsa et al., 1972). The single camera on the balloon experiment took one 3 second exposure every 78.64 seconds. The open-closed state of the shutter was telemetered to the ground and recorded on magnetic tape with the PCM data and time code.

Alignment of a camera with respect to the X-ray axis of a detector was accomplished by placing a screen in front of the detector, perpendicular to the mechanical axis of the collimator, and moving a Cd 109 X-ray source on the screen to locate the X-ray center. Exposing the first frame of the flight film to the screen, and making corrections for parallax, defines the position of the X-ray axis in the celestial sphere on the remaining frames.

Two approaches are possible for determining the X-ray center of the experiment. The first consists of searching for maximum count rate in the detector by scanning with the X-ray source in the vicinity of the X-ray axis. Even though only a few data points are required here, long duration observations have to be made as one is looking for a small effect in a region of large signal. This problem is analogous to

trying to determine the center of a gaussian distribution by examining only data points whose values are 90% of maximum, or larger.

The second method involves scanning in the region of .25 to .75 percent transmission where the X-ray transmission as a function of off-set angle can be represented by a straight line. Counting statistics of 1% yield least squares fits with errors of typically .5 arc min., allowing the X-ray axis to be determined to better than 1 arc min.

In addition to the systematic error suffered in using the first photo to define the position of the detector axis, the fact that the night sky is black forces one to use the sprocket holes on the film edge to determine the location of the film in the camera. Irregular positioning of the film with respect to the film guides amounts to an error of approximately 3 arc min. Shrinkage of the emulsions of the films has been measured and found not to contribute a significant error.

To determine the right ascension and declination of the detector axis, a rectangular coordinate system can be defined for all photographs as shown in Figure A1 (b). The coordinate system defines the center of the photo (X_c, Y_c) and the detector axis (X_x, Y_x) is defined from the first frame. From subsequent photos, the only remaining measurement is the position of any two stars (X_1, Y_1) and (X_2, Y_2).

If the detector axis and the center of the photograph are coincident, and stars near the center are used, plane trigonometry produces sufficiently accurate results. However, if the detector axis is off-center, errors as large as 6° are easily incurred, thus requiring spherical trigonometry for arc minute accuracy.

Given x , c , 1 , and 2 as positions of the detector axis, photo center, star 1 and star 2, angles δ_{12} , δ_{1x} , and δ_{2x} shown in Figure A1 (b) are readily computed. These angles are the same in both the photo plane and the celestial sphere since at the center, the photograph is a plane parallel to the celestial sphere. Defining R as the radius of curvature of the celestial sphere (as seen in the photograph) in the same units used in the rectangular coordinate system of the photos, the arcs from the center to the detector axis and two stars are, as shown in Figure A1 (a),

$$\eta_1 = \left[(x_c - x_1)^2 + (y_c - y_1)^2 \right]^{1/2} / R, \quad (A1)$$

$$\eta_2 = \left[(x_c - x_2)^2 + (y_c - y_2)^2 \right]^{1/2} / R, \quad (A2)$$

$$\eta_x = \left[(x_c - x_x)^2 + (y_c - y_x)^2 \right]^{1/2} / R, \quad (A3)$$

and spherical trigonometry (Smart, 1962) yields

$$\cos \epsilon_{12} = \cos \eta_1 \cos \eta_2 + \sin \eta_1 \sin \eta_2 \cos \delta_{12}, \quad (A4)$$

$$\cos \epsilon_{1x} = \cos \eta_1 \cos \eta_x + \sin \eta_1 \sin \eta_x \cos \delta_{1x}, \quad (A5)$$

$$\cos \epsilon_{2x} = \cos \eta_2 \cos \eta_x + \sin \eta_2 \sin \eta_x \cos \delta_{2x}, \quad (A6)$$

where all η 's and ϵ 's are between 0 and $\pi/2$ due to the size of the photos.

The angle ϕ , between arc ϵ_{12} and a line of longitude α_1 , requires two expressions to fully define it, since it can be in any quadrant. Specifically,

$$\sin \phi = \frac{\cos \delta_2 \sin (\alpha_2 - \alpha_1)}{\sin \epsilon_{12}} \quad (A7)$$

$$\cos \phi = \frac{\sin \delta_2 - \sin \delta_1 \cos \epsilon_{12}}{\cos \delta_1 \sin \epsilon_{12}} \quad (\text{A8})$$

where α_1 , δ_1 , and α_2 , δ_2 , are the right ascension and declination of stars 1 and 2.

The angle between arcs ϵ_{12} and ϵ_{1x} is

$$\cos \beta = \frac{\cos \epsilon_{2x} - \cos \epsilon_{1x} \cos \epsilon_{12}}{\sin \epsilon_{1x} \sin \epsilon_{12}} \quad (\text{A9})$$

where $0 \leq \beta \leq \pi$. Finally, the declination and right ascension of the detector axis is

$$\delta_x = \sin^{-1} \left[\sin \delta_1 \cos \epsilon_{1x} + \cos \delta_1 \sin \epsilon_{1x} \cos (\beta + \phi) \right], \quad (\text{A10})$$

and

$$\alpha_x = \alpha_1 + \sin^{-1} \left[\frac{-\sin \epsilon_{1x} \sin (\beta + \phi)}{\cos \delta_x} \right], \quad (\text{A11})$$

where β and ϕ are positive in the direction as defined by Figure A1 (a).

REFERENCES

- Agrawal, P. G., 1972, Study of Cosmic X-Ray Sources Using Balloon Borne Detectors, Ph.D. Thesis, University of Bombay.
- Aller, L. H., 1963, The Atmospheres of the Sun and Stars, 2nd ed., (The Ronald Press Co., New York).
- Allison, S., 1958, R.M.P., 30, 1137.
- Baldwin, J. E., 1967, Radio Astronomy and the Galactic System, IAU Symposium No. 31, 337.
- Bates, D. R. and Dalgarno, A., 1953, Proc. Phys. Soc. (London), A66 972.
- Berger, M. J., and Seltzer, S. M., 1964, Tables of Energy Losses and Ranges of Electrons and Positrons, NASA Document SP-3012.
- Bertotti, B., Cavaliere, A., and Pacini, F., 1969, Nature, 223, 1351.
- Bethe, H. A. and Salpeter, E. E., 1957, Quantum Mechanics of One and Two Electron Atoms, (Academic Press, Inc., New York).
- Betz, H. D., 1972, IEEE Trans. Nucl. Sci., 19, 249.
- Birsa, F. B., Glasser, C. A., Ziegler, M. M., 1972, 1.5 to 38 keV X-ray Experiment System for High Altitude Sounding Rockets, NASA-GSFC Document X-661-72-80.
- Bleach, R. D., Boldt, E. A., Holt, S. S., Schwartz, D. A., and Serlemitsos, P. J., 1972, Ap.J. 171, 51.
- Blumenthal, G. R. and Gould, R. J., 1970, Rev. Mod. Phys., 42, 237.
- Boldt, E. A., Desai, U. D., and Holt, S. S., 1969, Ap.J., 156, 427.
- Boldt, E. A., Doong, H., Serlemitsos, P., and Reigler, G. R., 1968, Canad. J. Phys., 46, S444.
- Boldt, E. A., Holt, S. S., and Serlemitsos, P. J., 1971, Ap.J. Lett., 164, L9.
- Boldt, E. A. and Serlemitsos, P. J., 1969, Ap.J., 157, 557.
- Bolton, C. T., 1972, Nature, 235, 271.

- Bradt, H., Garmire, G., Oda, M., Spada, G., Sreekantan, B. V., Gorenstein, P., and Gursky, H., 1968, Space Sci. Rev., 8, 471.
- Braes, L. L. E., and Miley, G. K., 1972, Nature, 237, 506
- Brandt, J. C., Maran, S. P., Williamson, R., Harrington, R. S., Cochran, C., Kennedy, M., Kennedy, W. J., and Chamberlin, V. D., 1973, Paper presented at the AAS Symposium on Science and Man, Mexico City, June 18.
- Brown, R. L. and Gould, R. J., 1970, Phys. Rev. D., 1, 2252.
- Burbidge, E. M., Burbidge, G. R., Fowler, W. A., and Hoyle, F., 1957, Rev. Mod. Phys., 29, 547.
- Burginyon, G., Hill, R., Seward, F., Tarter, B., and Toor, A., 1973, Ap.J. Lett., 180, L75.
- Burton, W. B., 1970, Astro. Astrophys. Suppl., 2, 261
- Cameron, A. G. W., 1959, Ap. J., 129, 676.
- Cancro, C. A., Crockett, W. R., Garrahan, N. M., and McGowan, R. G., 1968, X-Ray Experiment Electronics for High Altitude Balloon and Rocket Flights, NASA-GSFC Document X-711-68-74
- Canizares, C. R., McClintock, J. E., Clark, G. W., Lewin, W. H. G., Schnopper, H. W., and Sprott, G. F., 1973, Nature, 241, 28.
- Cartwright, B. G., Garcia-Munoz, M., and Simpson, J. A., 1971, Paper presented at the 12th International Conference on Cosmic Rays, August, 16, Hobart, Tasmania, Australia.
- Casse, M., 1973, Service d'Electronique Physique, CEN-Saclay, Preprint 482.
- Chapman, R. D., 1969, Ap. J., 156, 87.
- Clayton, D. D. and Craddock, W. L., 1965, Ap. J., 142, 189.
- Colgate, S. A., 1971, The Velocity and Composition of Supernova Ejecta, Proceedings of Conference at the NASA Goddard Space Flight Center on May 18, 1971, ed. S. P. Maran, J. C. Brandt, and T. P. Stecher, NASA-GSFC Document X-683-71-375.
- Comstock, G. M., Fan, C. Y., and Simpson, J. A., 1969, Ap. J., 155, 609.

- Cooley, J. W., Lewis, P. A. W., and Welch, P. D., 1967, IBM Watson Research Center, (Yorktown Heights, New York), Preprint TC-1743.
- Cosslett, V. E. and Thomas, R. N., 1964, Brit. J. Appl. Phys., 15, 1283.
- Dolan, J. F., Space Sci. Rev., 10, 830.
- Elwert, G., 1954, Z. Naturforsch., 9a, 637.
- Ermolaev, A. M., Jones, M., and Phillips, K. J. H., 1972, Ap. J. Lett., 12, L53.
- Evans, R. D., 1955, The Atomic Nucleus, (McGraw-Hill Book Co., Inc., New York).
- Fabian, A. C., Zarnecki, J. C., and Culhane, J. L., 1973, Nature Physical Science, 242, 18.
- Felten, J. E., Rees, M. J., and Adams, T. F., 1972, Astron. Astrophys., 21, 139.
- Friedman, H., 1973, Astro. Aero., 11, 30.
- Friedman, H., Bowyer, S., Byram, E. T., and Chubb, T. A., 1953, Space Research, V, 833.
- Friedman, H., Byram, E. T., and Chubb, T. A., 1967, Science, 156, 374.
- Fromme, C., 1966, J. of Chem. Phys., 45, 1417.
- Garcia, J. D., and Mack, J. E., 1965, J. Opt. Soc. Am., 55, 654.
- Giacconi, R., Gursky, H., and Paolini, F. R., 1962, Phys. Rev. Lett., 9, 439.
- Giacconi, R., Kellogg, E., Gorenstein, P., Gursky, H., and Tananbaum, H., 1971, Ap. J. Lett., 165, L27.
- Giacconi, R., Murray, S., Gursky, H., Kellogg, E., Schreier, E., Matilsky, T., Koch, D., and Tananbaum, H., 1973, The Uhuru Catalogue of X-Ray Sources, Preprint ASE-3249.
- Ginzburg, V. L. and Syrovatskii, S. I., 1964, The Origin of Cosmic Rays, (The Macmillan Co., New York).
- Glass, I. S., 1969, Ap. J., 157, 215.

- Gorenstein, P., Giaconni, R., and Gursky, H., 1967, Ap.J.Lett., 150, 185.
- Gorenstein, P., Gursky, H., Kellogg, E. M., and Giaconni, R., 1970, Ap.J., 160, 947.
- Gorenstein, P., Kellogg, E. M., and Gursky, H., 1970, Ap.J., 160, 199.
- Grader, R. J., Hill, R. W., Seward, F. D., and Toor, A., 1966, Science, 152, 1499.
- Gregory, P. C., Kronberg, P. P., Seaquist, E. R., Hughes, V. A., Woodsworth, A., Viner, M. R., Retallack, D., Hjellming, R. M., and Balick, B., 1972, Nature Physical Science, 239, 114.
- Grodstein, G. W., 1957, X-Ray Attenuation Coefficients from 10 keV to 100 MeV, NBS Circular 583.
- Handbook of Chemistry and Physics, 1963, 44th ed., C. D. Hodgman ed., (The Chemical Rubber Publishing Co., Cleveland).
- Harnden, F. R., 1971, Hard X-Ray Pulses, Ph.D. Thesis, Rice University.
- Haymes, R. C., Ellis, D. V., Fishman, G. J., Glenn, S. W., and Kurfess, J. D., 1968, Ap.J.Lett., 151, L125.
- Haymes, R. C. and Harnden, F. R., 1970, Ap.J., 159, 1111.
- Hayakawa, S. and Matsuoka, M., 1964, Suppl. Prog. Theoretical Physics (Kyoto), 30, 204.
- Heckman, H. A., Hubbard, E. L., and Simon, W. G., 1963, Phys. Rev., 129, 1240.
- Heitler, W., 1954, The Quantum Theory of Radiation, (The Clarendon Press, Oxford).
- Hiskes, D. R., 1965, Phys. Rev., 137, A361.
- Hjellming, R.M., 1972, private communication.
- Hjellming, R. M., Hermann, M., and Webster, E., 1972, Nature, 237, 507.
- Holt, S. S., 1972, private communication.
- Holt, S.S., 1970, X-Ray Detectors, ed. by H. Ogelman and J. R. Wayland, "Introduction to Experimental Techniques of High Energy Astrophysics", NASA Document SP-243.

- Holt, S. S., Boldt, E. A., Schwartz, D., Serlemitsos, P., and Bleach, R., 1971, Ap. J. Lett., 166, 155.
- Holt, S.S. and Ramaty, R., 1969, Solar Physics, 8, 119.
- Holt, S.S., and Ramaty, R., 1970, Ap. J. Lett., 5, 88.
- Hoyle, F., 1962, Astronomy, (Rathbone Books, Limited, London).
- Hoyle, F. and Fowler, W. A., 1960, Ap. J., 132, 565.
- Hudson, H. S., Peterson, L. E., and Schwartz, D. A., 1970, Ap. J. Lett., 159, L51.
- Jacobson, A. S., 1968, A Search for Gamma-Ray Line Emissions from the Crab Nebula, Ph. D. Thesis, University of California, San Diego.
- Jackson, J. D., 1965, Classical Electrodynamics, (John Wiley and Sons, Inc., New York).
- Katz, L. and Penfold, A. S., 1952, Rev. Mod. Phys., 24, 28.
- Karzas, W. J. and Latter, R., 1961, Ap. J. Suppl., 6, 167.
- Lewin, W. H. G., Clark, G. W., and Smith, W. B., 1968, Ap. J. Lett., 152, L55.
- MacAlpine, C. N., 1972, Ap. J., 175, 11.
- MacDonald, J. R. and Martin, F. W., 1971, Phys. Rev. A., 4, 1965.
- MacGregor, A., Seward, F., and Turiel, I., 1970, Ap. J., 161, 979.
- Matilsky, T., Gursky, H., Kellogg, E., Tananbaum, H., Murray, S., Giaconni, R., 1973, Ap. J., 181, 753.
- Matteson, J. L., 1971, An X-Ray Survey of the Cygnus Region in the 20 to 300 keV Energy Range, Ph.D. Thesis, University of California San Diego.
- McClintock, J. E., Lewin, W. A. G., Sullivan, R. J., and Clark, G. W., 1971, Nature, 223, 162.
- Meekins, J. F., Henry, R. C., Fritz, G., Friedman, H., and Byram, E. T., 1969, Ap. J., 157, 197.
- Melissinos, A. C., 1966, Experiments in Modern Physics, (Academic Press, New York).

- Minkowski, R., 1964, Ann. Rev. Astron. Astrophys., 2, 247.
- Nikolaev, V. S., 1965, Usp. Fiz. Nauk., 85, 679.
- Nikolaev, V. S., Dimitriev, I. S., Fateeva, L. N., and Teplova, Ya. A., 1961, Soviet Physics JETP, 12, 627.
- Nikolaev, V. S., Dimitriev, I. S., Fateeva, L. N., and Teplova, Ya. A., 1961, JETP, 40, 989.
- Novick, R., Weisskopf, M. C., Berthelsdorf, R., Linke, R., and Wolff, R. S., 1972, Ap. J. Lett., 174, L1.
- Nuclear Data Sheets, 1966, (Academic Press, Inc., New York).
- Nussbaumer, H. and Osterbrock, D. E., 1970, Ap. J., 161, 811.
- Oda, M., Gorenstein, P., Gursky, H., Kellogg, E., Schreier, E., Tananbaum, F., and Giacconi, R., 1971, Ap. J. Lett., 166, L1.
- Oda, M., Wada, M., Matsuoka, M., Miyamoto, S., Muranaka, N., and Ogawara, Y., 1972, Ap. J. Lett., L13.
- Oppenheimer, J. R. and Volkoff, G. M., 1939, Phys. Rev., 55, 374.
- Overbeck, J. W. and Tananbaum, H. D., 1968, Ap. J., 153, 899.
- Pacini, F., 1971, Ap. J. Lett., 163, L17.
- Parsignault, D. R., Gursky, H., Kellogg, E. M., Matilsky, T., Murray, S., Schreier, E., Tananbaum, H., Giacconi, R., and Brinckman, A. C., 1972, Nature Physical Science, 239, 123.
- Peimbert, M. and van den Bergh, S., 1971, Ap. J., 167, 223.
- Penny, W. G., 1930, Phil. Mag., 9, 661.
- Peterson, L. E., 1970, Non Solar X- and Gamma Ray Astronomy, IAU Symposium No. 37, ed. L. Gratton, (D. Reidel, Dordrecht), 57.
- Peterson, L. E., 1972, Hard Cosmic X-Ray Sources, IAU Symposium No. 55, May 11, Madrid, Spain.
- Peterson, L. E., 1973, private communication.
- Pierce, T. E. and Blaun, M., 1968, Phys. Rev., 173, 390.
- Pounds, K. A., 1970, Science J., 6, 61.

- Price, P. B., 1971, Paper presented at the 12th International Conference on Cosmic Rays, August 16, Hobart, Tasmania, Australia.
- Ramaty, R., Boldt, E. A., Colgate, S. A., and Silk, J., 1971, Ap. J., 169, 87.
- Reinert, C. P., 1969, Ph.D. Thesis, University of Minnesota, Technical Report CR-132.
- Reynolds, H. L., Wyly, L. D., and Zucker, A., 1955, Phys. Rev., 98, 1825.
- Rocchia, R., Rothenflug, R., Boclet, D., and Durouchoux, Ph., 1969, Astron. Astrophys., 1, 48.
- Rossi, B., 1952, High Energy Particles, (Prentice-Hall Inc., New York).
- Sanford, P. W. and Hawkins, F. H., 1972, Nature Physical Science., 239, 135.
- Schiff, H., 1954, Canad. J. Phys., 32, 393.
- Schwartz, D. A., Hudson, H. S., and Peterson, L. E., 1970, Ap. J., 162, 431.
- Searle, L., 1971, Ap. J., 168, 41.
- Shapiro, M. M. and Silberberg, R., 1970, Ann. Rev. Nucl. Sci., 20, 323.
- Shapiro, M. M., Silberberg, R., Tsao, C. H., 1971, Revised Source Composition of Cosmic Rays from Hydrogen to Nickel, Paper presented at the 12th International Conference on Cosmic Rays, August 16, Hobart, Tasmania, Australia.
- Shklovsky, I. S., 1972, Nature, 238, 144.
- Shulman, S., Fritz, G., Meekins, J. F., and Friedman, H., 1971, Ap. J. Lett., 168, L49.
- Silk, J. and Steigman, G., 1969, Phys. Rev. Lett., 23, 597.
- Smart, W. M., 1962, Spherical Astronomy, (The University Press, Cambridge).
- Smathers, A., 1972, private communication.
- Storm, E., and Israel, H. I., 1967, Photon Cross Sections from .001 to 100 MeV, for Elements 1 through 100, LASL Document LA-3753.

- Strominger, D., Hollander, J. M., and Seaborg, G. T., 1958, Rev. Mod. Phys., 30, 585.
- Tananbaum, H., Gursky, H., Kellogg, E., Levinson, R., Schreier, E., and Giacconi, R., 1972, Ap. J. Lett. 174, L143.
- Tucker, W. H., 1967, Ap. J., 148, 745.
- Tucker, W. H., 1971, Science, 172, 372.
- Tucker, W. H. and Gould, R. J., 1966, Ap. J., 144, 244.
- Urch, I. H. and Gleeson, L. J., 1972, Astroph. Sp. Sci., 17, 426.
- Van den Bergh, S., 1971, Ap. J., 165, 457.
- Van den Bergh, S. and Dodd, W. W., 1970, Ap. J., 162, 485.
- Van Reyemorter, M. H., 1962, Ap. J., 136, 906.
- Webber, W. R. and Reinert, C. P., 1970, Ap. J., 162, 883.
- Webster, B. L. and Mordin, P., 1972, Nature, 235, 37.
- Woltjer, L., 1964, Ap. J., 140, 1309.
- Woltjer, L., 1972, Supernova Remnants, Preprint, Columbia Astrophysics Laboratory Contribution no. 59.

Table 3.1

Relative Probabilities, α , for Photoelectric
Absorption into Various Shells

<u>Shell</u>	<u>α</u>
K	1.000
L _I	.0877
L _{II}	.0443
L _{III}	.0249
M _I	.00398
M _{II}	.00174
M _{III}	.000782
M _{IV}	.000361
M _V	.000242
N _V	.000042

Table 3.2

Interaction Probabilities for an X-Ray with
the K-Shell of Xenon

Effect	Effect Probability	Transition Probability	Most Energetic Particle Emitted*	Particle Energy (keV)	Total Probability
Auger K_{α}	.125	.7999	electron	24.777	.1000
" K_{β}	.125	.2001	"	32.993	.0250
Fluor. K_{α}	.875	.7999	photon	29.669	.6999
" K_{β}	.875	.2001	"	33.777	.1751

* This is in addition to a photoelectron whose energy is 34.561 keV less than the photon energy.

Table 3.3

Interaction Probabilities for an X-Ray with
the L-Shell of Xenon

Effect	Effect Probability	Transition Probability	Most Energetic Particle Emitted*	Particle Energy (keV)	Total Probability
(A) L_I Shell					
Auger L_β	.860	.8098	electron	3.521	.6964
" L_γ	.860	.1902	"	5.121	.1636
Fluor. L_β	.140	.8098	photon	4.483	.1134
" L_γ	.140	.1902	"	5.298	.0266
(B) L_{II} Shell					
Auger L_β	.860	1.0000	electron	3.728	.8600
Fluor. L_β	.140	1.0000	photon	4.415	.1400
(C) L_{III} Shell					
Auger L_α	.860	.8427	electron	3.410	.7247
" L_β	.860	.1573	"	4.634	.1353
Fluor. L_α	.140	.8427	photon	4.096	.1180
" L_β	.140	.1573	"	4.708	.0220

* This is in addition to a photoelectron whose energy is 5.445 keV less than the photon energy for the L_I shell, 5.102 keV for the L_{II} shell and 4.782 keV for the L_{III} shell.

Table 3.4

Fractions of Fluorescence Photons Leaving
the Balloon Detector (Resonance Escape)
and Remaining in the Same Cell, for Initial
Photon Energies ≥ 15 keV.

Layer	K-Shell Interactions		L-Shell Interactions	
	Fraction Leaving Detector	Fraction Remaining in Cell	Fraction Leaving Detector	Fraction Remaining in Cell
1	.71290	.07282	.08065	.74207
2	.65310	"	.01107	"
3	.62763	"	.00997	"
4	.61568	"	.00899	"
5	.61568	"	.00899	"
6	.62763	"	.00997	"
7	.65310	"	.01107	"

Table 3.5

Fractions of Fluorescence Photons Leaving the Rocket
Detectors (Resonance Escape) and Remaining in the Same
Cell

Layer (Number) Detector (Letter)	K-Shell Interactions		L-Shell Interactions	
	Fraction Remaining in Cell	Fraction Leaving Detector	Fraction Remaining in Cell	Fraction Leaving Detector
(A) Above K-Shell1, $E \geq 34.561$ keV				
1B	.05386	.80370	.63456	.11338
2B	"	.77916	"	.00726
3B	"	.77916	"	.00726
2A	"	.82440	"	.11386
3A	"	.80770	"	.01226
(B) Between L_I and L_{II} Shell, $5.102 \leq E \leq 5.445$ keV				
1B			.58907	.26037
2B			"	.00987
3B			"	.00250
2A			"	.25138
3A			"	.01186
(C) Between L_{II} and L_{III} Shell, $4.782 \leq E \leq 5.102$ keV				
1B			.61990	.23707
2B			"	.00677
3B			"	.00167
2A			"	.22554
3A			"	.00744

Table 3.6

X-Ray Lines from Laboratory Calibration Sources.
(Line Intensities from Various Groups are Unrelated
Unless Noted.)

Source	Decay Mode	Half Life	Energy (keV)	Line	Relative Intensity	Comment
$_{26}\text{Fe}^{55}$	EC	2.7 yrs.	5.899	$K\alpha_1\text{Mn}$	100.	
			5.888	$K\alpha_2\text{Mn}$	52.	
			6.492	$K\beta_1\text{Mn}$	12.1	
			6.492	$K\beta_3\text{Mn}$	6.0	
			5.895	$K\alpha$		
			5.959	All K		
$_{27}\text{Co}^{57}$	EC	270 days	14.37	$\gamma_1\text{Fe}^{57}$	1.0	
			121.94	$\gamma_2\text{Fe}^{57}$	1.0	
			136.31	$\gamma_3\text{Fe}^{57}$.07	
			6.404	$K\alpha_1\text{Fe}$	100.	
			6.391	$K\alpha_2\text{Fe}$	52.	
			7.059	$K\beta_1\text{Fe}$	12.5	
			7.059	$K\beta_3\text{Fe}$	6.2	
			6.400	$K\alpha$		
			6.472	All K		
$_{27}\text{Co}^{60}$	β^-	5.23 yrs.	1172.8	$\gamma_1\text{Ni}^{60}$	100.	
			1332.5	$\gamma_2\text{Ni}^{60}$.99	
			2158.0	$\gamma_3\text{Ni}^{60}$.0012	
$_{48}\text{Cd}^{109}$	EC	470 days	87.5	γAg^{109}		
			22.163	$K\alpha_1\text{Ag}$	100.	K/L \approx 5.0
			21.990	$K\alpha_2\text{Ag}$	52.	
			24.942	$K\beta_1\text{Ag}$	18.4	
			24.912	$K\beta_3\text{Ag}$	9.2	
			25.455	$K\beta_2\text{Ag}$	2.94	
			2.984	$L\alpha_1\text{Ag.}$	100.	
			3.151	$L\beta_1\text{Ag}$	55.	
			3.346	$L\beta_2\text{Ag}$	20.	
			2.978	$L\alpha_2\text{Ag}$	12.0	
			3.235	$L\beta_3\text{Ag}$	8.5	
			3.204	$L\beta_4\text{Ag}$	6.4	
			22.104	$K\alpha$	152.0	
			24.982	$K\beta$	30.54	
			3.083	All L		

Table 3.6 (Continued)

Source	Decay Mode	Half Life	Energy (keV)	Line	Relative Intensity	Comment
$_{56}\text{Ba}^{133}$	EC	7.2 yrs.	53.	$\gamma_1 \text{Cs}^{133}$.015-.073	
			79.	$\gamma_2 \text{Cs}^{133}$.07 -.09	
			81.	$\gamma_3 \text{Cs}^{133}$.32 -.55	
			160.	$\gamma_4 \text{Cs}^{133}$.004-.02	
			30.973	$K\alpha_1 \text{Cs}$	100.	K/L \approx 20.
			30.625	$K\alpha_2 \text{Cs}$	52.	
			34.987	$K\beta_1 \text{Cs}$	20.5	
			34.920	$K\beta_3 \text{Cs}$	10.3	
			35.896	$K\beta_2 \text{Cs}$	7.4	
			4.286	$L\alpha_1 \text{Cs}$	100.	
			4.620	$L\beta_1 \text{Cs}$	55.	
			4.933	$L\beta_2 \text{Cs}$	20.	
			4.272	$L\alpha_2 \text{Cs}$	12.	
			4.715	$L\alpha_3 \text{Cs}$	8.5	
			30.854	$K\alpha$	152.0	
			35.145	$K\beta$	38.2	
			4.464	All L		
$_{61}\text{Pm}^{145}$	EC	18 yrs.	67.	$\gamma_1 \text{Nd}^{145}$	9	
			72.	$\gamma_2 \text{Nd}^{145}$	12	
			37.361	$K\alpha_1 \text{Nd}$	100.	
			36.847	$K\alpha_2 \text{Nd}$	52.	
			42.271	$K\beta_1 \text{Nd}$	21.6	
			42.166	$K\beta_3 \text{Nd}$	10.8	
			43.441	$K\beta_2 \text{Nd}$	8.2	
			37.185	$K\alpha$	152.	
			42.484	$K\beta$	40.6	
$_{78}\text{Pt}^{193}$	EC	500 yrs.	9.175	$L\alpha_1 \text{Ir}$	100.	
			10.708	$L\beta_1 \text{Ir}$	55.	
			10.922	$L\beta_2 \text{Ir}$	20.	
			9.099	$L\alpha_2 \text{Ir}$	12.	
			10.868	$L\beta_3 \text{Ir}$	8.5	
			10.511	$L\beta_4 \text{Ir}$	6.4	
			9.167	$L\alpha$	112.	
			10.757	$L\beta$	89.9	

Table 3.6 (Continued)

Source	Decay Mode	Half Life	Energy (keV)	Line	Relative Intensity	Comment
^{241}Am	α	458 yrs.	26.36	$\gamma_1 \text{Np}^{237}$	3.3	
			33.20	$\gamma_2 \text{Np}^{237}$.2	
			43.46	$\gamma_3 \text{Np}^{237}$.24	
			59.57	$\gamma_4 \text{Np}^{237}$	40.	
			103.	$\gamma_5 \text{Np}^{237}$.04	
			29.6	$\gamma_1 \text{Pa}^{233}$	12.	Pa^{233} decays with several low energy gammas.
			87.	$\gamma_2 \text{Pa}^{233}$	18.	
			143.	$\gamma_3 \text{Pa}^{233}$	1.	
			198.	$\gamma_4 \text{Pa}^{233}$	1.	
			13.949	$L\alpha_1 \text{Np}$	100.	
			17.750	$L\beta_1 \text{Np}$	55.	
			16.841	$L\beta_2 \text{Np}$	20.	
			13.763	$L\alpha_2 \text{Np}$	12.	
			17.992	$L\beta_3 \text{Np}$	8.5	
			17.061	$L\beta_4 \text{Np}$	6.4	
			13.929	$L\alpha$	112.0	
			17.522	$L\beta$	89.9	

Table 3.7

Fractional Inhibit and Dead Times in
Balloon and Rocket Electronics Systems

	Symbol	Rocket Experiment	Balloon Experiment
Scalar Inhibit	τ	17/320	197/3200
PHA Inhibit	y	2/320	2/3200
Dead Time	d	3.5/320	3.5/3200
Anticoincidence Time	g	2.25/320	2.25/3200

Table 3.8

Collimator Parameters for the Balloon and
Rocket Detectors

Tube diameter ("), d	0.1815	0.026	0.250
Tube length ("), ℓ	3.4375	3.000	2.890
Number of tubes	4317	142700 \pm 500	1903
Area (cm ²)	720.600	488.796 \pm 1.713	602.665
FWHM ($^{\circ}$)	2.4436	6483	4
		(.401198 for single tube)	
Solid angle (ster.)	.0014284	.00010052	.0038264
Max. opening angle ($^{\circ}$), θ_{MAX}	3.0224	(.49655 for single tube) 4.944	

Table 3.9

Results of Study to Determine the Amount of
Bowling of the $1/2^\circ$ Collimator in a Vacuum
(All Units are in Arc Minutes).

	Section 1		Section 2		Section 3		Average
	X	Y	X	Y	X	Y	
Center	(-3.49, 1.27)		(-1.06, -.65)		(4.54, -.63)		$(0 \pm 4.12, 0 \pm 1.10)$
Bowing Angle	2.34	-2.15	1.85	1.26	1.47	1.63	1.07 ± 1.62
	12.76	9.17	10.39	6.99	24.13	8.97	12.07 ± 6.21

Table 3.10

Typical Balloon Borne Experiments in X-Ray Astronomy

Group	Guidance Mount	Area (cm ²)	Collimation FWHM(°)	Type	Energy Range (keV)	Background (photons/cm ² sec keV)	Resolution (%)
Goddard Space Flight Center	Alt-Azimuth	602	4	Proportional Counter	3-80	10 ⁻⁴ /Layer	10
Naval Research Laboratory	Alt-Azimuth	1000	8	Proportional Counter	~10-70	~1.5x10 ⁻³	
U. of California San Diego	Equatorial Mount	34	6	Scintillator	10-400	6x10 ⁻⁴	35
Rice University	Equatorial Mount	81	24	Scintillator	30-500	10 ⁻³	
Tata Institute, India	Equatorial Mount	97	18.6	Scintillator	15-150	2.5x10 ⁻³	~40

Table 4.1

Summary of the Observational Program

Flight	Date	Launch Site	Maximum Altitude	Time at Altitude	Discrete Sources Observed	Comments
Balloon 646-P	Oct. 27, 1971	Palestine, Texas	134,000 ft.	1 hr.	none	guidance failure
Rocket 13.009	May 19, 1972	White Sands, New Mexico	480,300 ft.	3.4 min.	Cas A Tycho	60 second observa- tion 100 second obser- vation
Balloon 683-P	June 19, 1972	Palestine, Texas	133,000 ft.	6 hrs.	Cyg X-1 Cyg X-2 Cyg X-3	multiple transits, high signal to noise single transit, low flux multiple transits, low flux
Balloon 695-P	Aug. 29, 1972	Palestine, Texas	0	0	-	ground abort
Balloon 696-P	Aug. 30, 1972	Palestine, Texas	132,000 ft.	7 hrs.	Cyg X-3	accurate pointing, Cyg X-3 below threshold

Table 4.2

Temporal History of Rocket Flight 13.009

Universal Time (h m s)	Elapsed Time (Seconds)	Function
9 0 00.54	0	Launch
	48.96	End of powered flight Altitude = 39300 m Velocity = 1448 m/sec
	55.00	High voltage on in experiments
	102.31	Star Tracker on α Cyg
	103.35	Cameras on
	112.90	Doors open Altitude = 111000 m Velocity = 858 m/sec
	123.37	Star Tracker on β Cas
	137.46	Hold on Cas A
	197.49	Leave Cas A
	206.69	Hold on Tycho
	306.75	Leave Tycho
	317.00	Doors close Altitude = 83873 m Velocity = 1114 m/sec
Maximum altitude = 147332 m at 200.97 seconds.		

Table 4.3

Summary of Rocket Observation Times

	Detector	Offset	Observing Time (Seconds)	Effective Observation (Seconds)
CasA	A	$.217 \pm .054^\circ$	61.440	27.5 ± 4.2
	B	$.663 \pm .102^\circ$	61.440	44.6 ± 2.6
Tycho	A	$.274 \pm .054^\circ$	99.738	37.2 ± 7.2
	B	$.689 \pm .102^\circ$	99.738	71.3 ± 4.2

Table 4.4

Effective Exposure to Sources, Balloon Flight 683-P

TIME (UT)	Effective Exposure (Seconds)	Source
0530	29.1 \pm 1.2	Cyg X-1
0614	186.9 \pm 7.5	Cyg X-1
0650	9.34 \pm .37	Cyg X-1
0658	19.05 \pm .76	Cyg X-1
0830	197.2 \pm 7.9	Cyg X-1
0925	521. \pm 21.	Cyg X-1
0933	35.9 \pm 1.4	Cyg X-3
0943	40.9 \pm 1.6	Cyg X-1
0945	30.4 \pm 1.2	Cyg X-3
0947	73.4 \pm 2.9	Cyg X-2
1013	7.85 \pm .32	Cyg X-1
1021	10.58 \pm .42	Cyg X-3
1024	62.8 \pm 2.5	Cyg X-1
1035	61.9 \pm 2.5 *	Cyg X-1

* Accurate pointing information available only for this time.

Table 5.1

Relative Abundances of Elements in the Interstellar Gas

Element	Log_{10}^N
H	12.00
He	10.92
C	8.60
N	8.05
O	8.95
Ne	8.00
Mg	7.40
Si	7.50
S	7.35
A	6.88
Fe	7.15
Ni	5.94

Table 5.2

Comparison of Observed Probability Distributions in 10.49 sec
Fourier Analyses of Cas A with That Expected from Random Data

		$p < .04$	$p < .02$	$p < .01$	$p < .001$	$p < .0001$
Expected		656	328	164	16.4	1.6
Trial	1	682	361	193	21	2
	2	654	338	172	17	1
	3	673	364	191	21	2
	4	637	318	165	22	2
	5	645	332	168	17	3
	6	663	336	175	22	1

Table 5.3

Summary of Models Tested on the Cas A Spectrum
as a Function of Chi-Square per
Degrees of Freedom (χ^2/f).

Model	Energy Range (keV)	χ^2/f	Acceptable Fit	Comment *
1. Power Law	2.0-16.1	9.5	No	Best fit $4.45E^{-3.58}$
	2.0- 4.2, 10.3-16.1	1.0	Yes	$(10.3 \pm .5) E^{-4.35 \pm .10}$
2. Exponential	2.0-16.1	27.2	No	Best fit $3.7/E e^{-E/1.21}$
	2.0- 4.2, 10.3-16.1	1.7	Yes	$(4.5 \pm .6)/E e^{-E/(.83 \pm .06)}$
3. Combinations of power law and exponential	2.0-16.1		No	
4. Iron charge exchange	2.0-16.1	1.4	Yes	Absorption = 1.4×10^{22} H atoms/cm ³ . $C_1 = 8.49 \pm 1.29$ $C_2 = .000412 \pm .000030$ $\sigma = 1.23 \pm .09$ keV
5. CXB, cosmic ray power law distribution	2.0-13.7		No	
	3.9-16.1	~ 1.24	Yes	See Figure 5.4
6. CXB, cosmic ray $\sim E^{-2.6}$, X-ray power law con- tinuum.	2.0-16.1		Yes	For iron cut off at 17 MeV/nucleon, X-ray power law index ≥ 6.5 , and ab- sorption $\geq 2 \times 10^{22}$ H atoms/cm ² .
7. CXB, cosmic ray $\sim E^{-2.6}$, X-ray exponential continuum	2.0-16.1	1.2	Yes	For iron cut off at 17 MeV/nucleon, $kT = .48 \pm .16$ keV absorption = $(1.7 \pm .5)$ $\times 10^{22}$ H atoms/cm ² .

Table 5.3 (Continued)

Model	Energy Range (keV)	χ^2/f	Acceptable Fit	Comment *
8. Primordial, same as 7.	2.0-16.1		No	

* All units are photons/cm²sec keV, where applicable.

Table 5.4

Summary of Models Tested on the Tycho Spectrum
as a Function of Chi-Square per
Degrees of Freedom (χ^2/f).

Model	Energy Range (keV)	χ^2/f	Acceptable Fit	Comment *
1. Power Law	2.0-16.1	3.4	No	Best fit $9.17 E^{-5.75}$
	2.0- 5.2	2.3	No	Best fit $18.5 E^{-6.65}$
2. Exponential	2.0-16.1	3.4	No	Best fit $21.9/E e^{-E/4.9}$
	2.0- 5.2	.73	Yes	$(30.8 \pm 1.8)/E e^{-E/45 \pm .05}$
3. Combinations of power law and exponential	2.0-16.1		No	
4. CXB, cosmic ray $\sim E^{-2.6}$, X-ray power law con- tinuum.	2.0-16.1		No	For iron cut off at 7.3 MeV/nucleon, X-ray power law index ≥ 2.6 , 3.8×10^{22} H atoms/ cm^2
5. CXB, cosmic ray $\sim E^{-2.6}$, X-ray thermal con- tinuum.	2.0-16.1	1.5	Yes	For iron cut off $7.3^{+7.1}_{-4.3}$ MeV/nucleon, $kT = .38^{+.06}_{-.08}$ keV, absorption = $1.7^{+1.1}_{-.6}$ $\times 10^{22}$ H atoms/ cm^2 .

* All units are photons/ $\text{cm}^2\text{sec keV}$, where applicable.

Table 5.5

Thermal Bremsstrahlung, Charge Exchange, and
Non Thermal Bremsstrahlung components of the
Cas A Spectrum (less interstellar absorption)

Element	Z	Obs. Cosmic Ray Abund.	Non Thermal Brems- strahlung (keV/cm ² sec)	Charge Exchange (keV/cm ² sec)	Mean Energy of Charge Exchange Line (keV)	Primordial Cosmic Ray Abund.
H	1	20000.	.22	-	-	20000
He	2	4000.	.18	-	-	2700
Li	3	17.	.0017	-	-	0
Be	4	9.2	.0016	-	-	0
B	5	29.	.0081	-	-	0
C	6	100.	.036	-	-	100
N	7	27.	.012	-	-	12
O	8	91.	.046	-	-	102
F	9	1.8	.0011	-	-	0
Ne	10	19.	.012	-	-	20
Na	11	3.4	.0029	-	-	1
Mg	12	23.	.016	.00076	1.5	27
Al	13	3.	.0023	.022	1.7	1
Si	14	17.	.013	.23	2.0	23
P	15	1.	.00083	.020	2.3	0
S	16	2.5	.0021	.041	2.6	4
Cl	17	.31	.00028	.0069	3.0	0
A	18	1.5	.0015	.048	3.4	2
K	19	.92	.00083	.018	3.7	0
Ca	20	1.5	.0013	.025	4.1	2
Sc	21	.6	.00060	.014	4.6	0
Ti	22	2.	.0021	.052	5.0	0
V	23	.5	.00054	.014	5.5	0
Cr	24	2.5	.0026	.061	6.0	0
Mn	25	1.9	.0021	.049	6.5	0
Fe	26	9.6	.0103	.21	7.0	23
Co	27	.02	.000022	.00033	7.5	0
Ni	28	.5	.00050	.011	8.1	1
Cu	29	.009	.0000098	.00019	8.7	0
Zn	30	.015	.000016	.00031	9.3	0
Total Contribution			.578	.823		

The thermal continuum at $kt = .5$ contributes $.694 \text{ keV/cm}^2 \text{ sec.}$

Table 5.6

Charge Exchange Cross Sections Calculated
for 17 MeV/Nucleon Fe Nuclei Impinging
on Interstellar Matter

Element	Atomic Number	σ (cm ² /atom)	$\bar{\sigma}$ (cm ² /H atom)
H	1	3.45×10^{-23}	3.45×10^{-23}
He	2	1.07×10^{-21}	8.90×10^{-23}
C	6	1.83×10^{-19}	7.29×10^{-23}
N	7	3.46×10^{-19}	3.88×10^{-23}
O	8	5.78×10^{-19}	5.15×10^{-22}
Ne	10	1.24×10^{-18}	1.24×10^{-22}
Mg	12	2.04×10^{-18}	5.12×10^{-23}
Si	14	2.80×10^{-18}	8.85×10^{-23}
S	16	3.38×10^{-18}	7.57×10^{-23}
A	18	3.73×10^{-18}	2.83×10^{-23}
Fe	26	3.58×10^{-18}	5.06×10^{-23}
Ni	28	3.29×10^{-18}	2.87×10^{-24}
Total			1.17×10^{-21}

Table 5.7

Comparison of Observed Probability Distributions in 104.9 sec.
 Fourier Analysis of Cyg X-1 with that Expected from Random Data.
 The contribution to the oscillations of the gondola have been
 removed.

	p<.04	p<.02	p<.01	p<.001	p<.0001
Expected	656	328	164	16.4	1.6
Time 06:11:55	661	330	165	25	1
06:13:40	675	345	177	19	3
06:15:25	636	321	158	20	4
08:24:17	658	345	197	16	2
08:27:05	673	334	162	14	2
08:28:50	655	332	152	16	2
08:30:35	666	331	168	17	0
09:23:25	673	340	164	19	3
09:25:10	639	331	157	10	1
09:26:55	652	321	157	15	2
09:28:40	671	342	156	14	1
09:30:24	668	332	165	15	0
09:32:09	672	352	175	18	3
Mean	661	335	166	16.7	1.8

Table 5.8

Cyg X-3 Observation During 696-P

Sample	Time (Sec.)	Source	Background	Δ	E ⁻⁴	# σ	E ^{-2.3}
1	324	4178	4320	-1.5 σ	118.4	1.8	624.5
2	659	8216	8381	-1.3 σ	321.7	3.5	1558.
3	1196	15123	14857	+1.5 σ	609.7	5.0	2880.
4	2386	29961	30223	-1.1 σ	1127.0	6.5	5284.
5	600	7679	7403	+2.2 σ	257.3	3.0	1214.
6	600	7528	7689	-1.3 σ	218.7	2.5	1045.
Total	5765	72685	72873	- .5 σ	2653.0	9.8	12606.

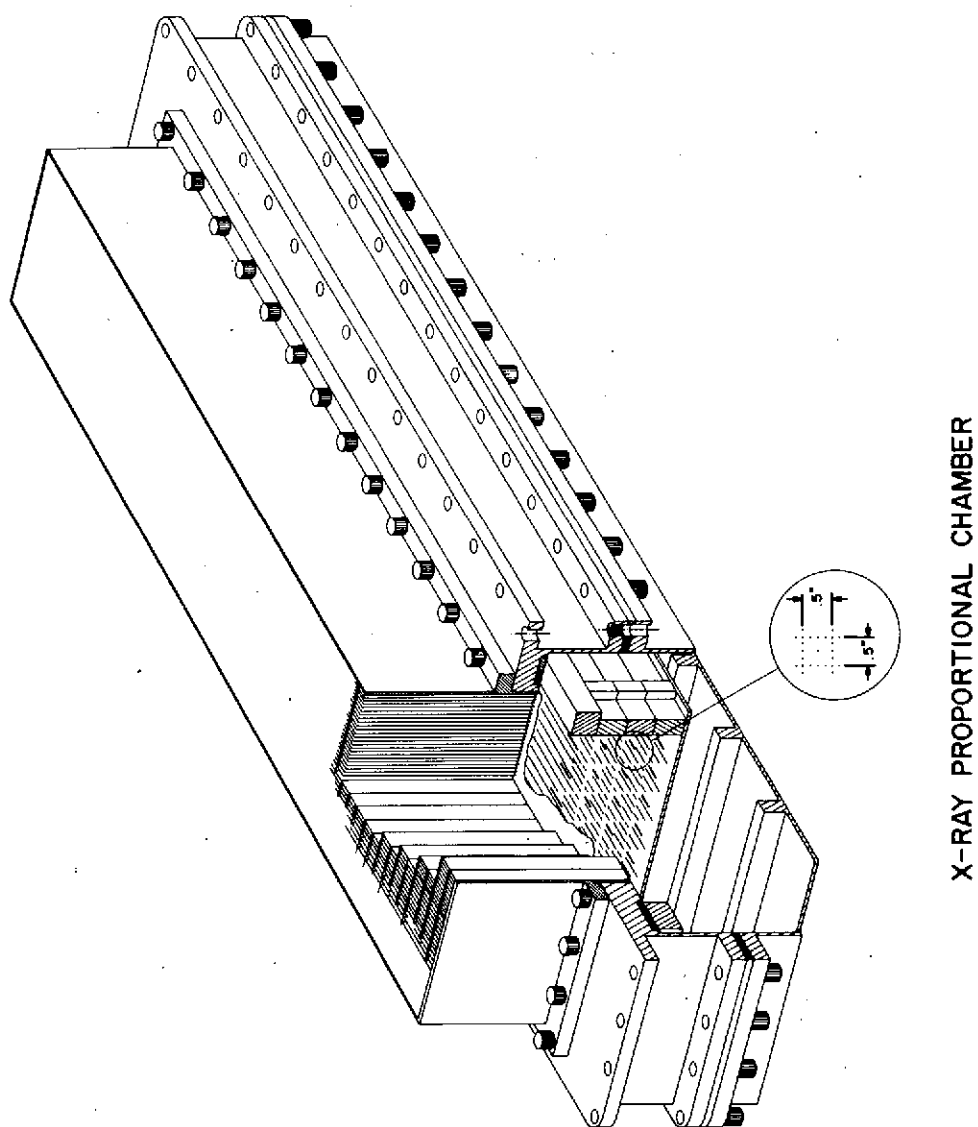


Figure 3.1 - Three-dimensional view of a multilayer multianode X-ray proportional counter, typical of the ones used in these experiments. The cutaway shows the geometry of the cells under the thin window and collimator.

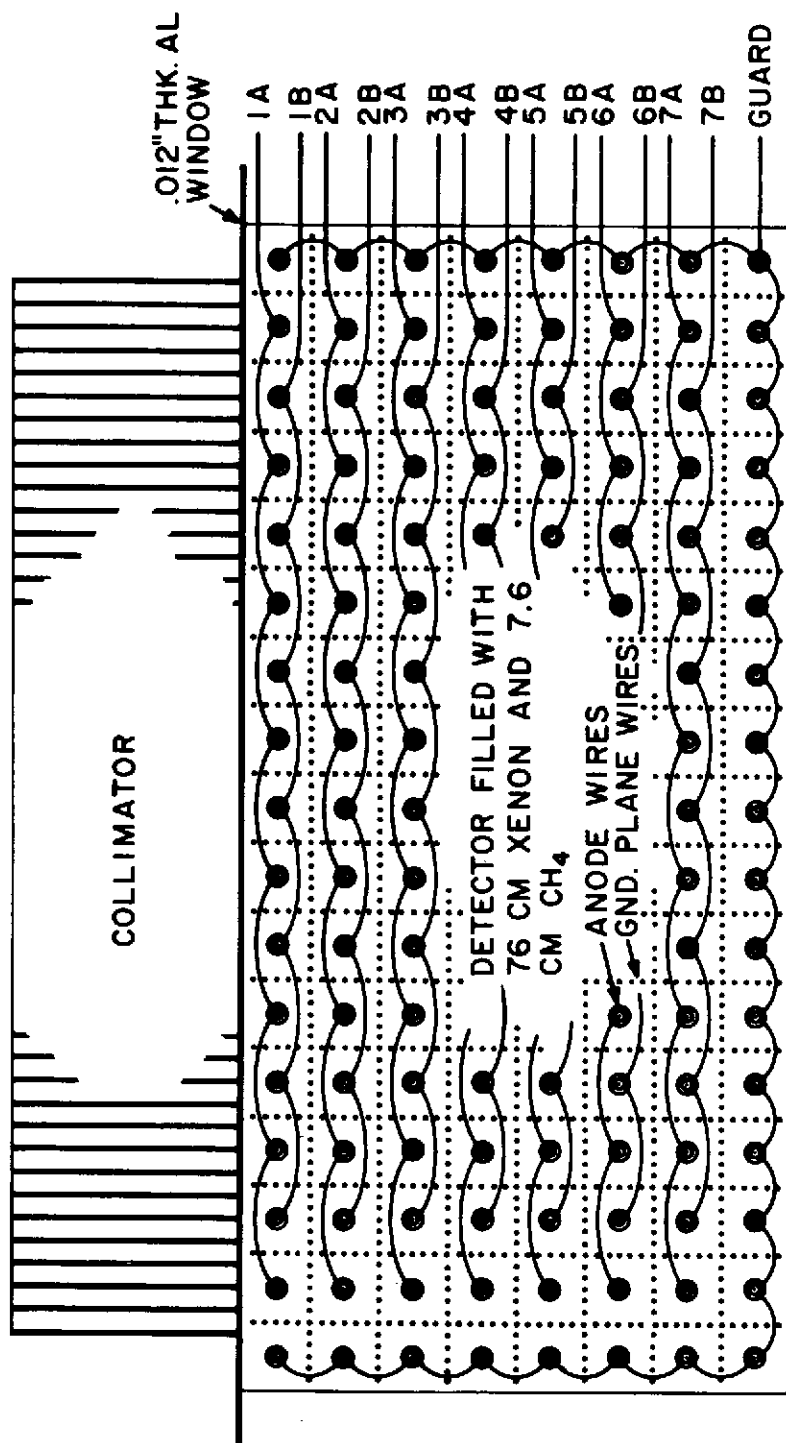


Figure 3.2 - Side view of balloon borne multilayer multianode proportional counter showing location and wiring of cells under the window and collimator. Alternate cells in this detector are coded "A" and "B".

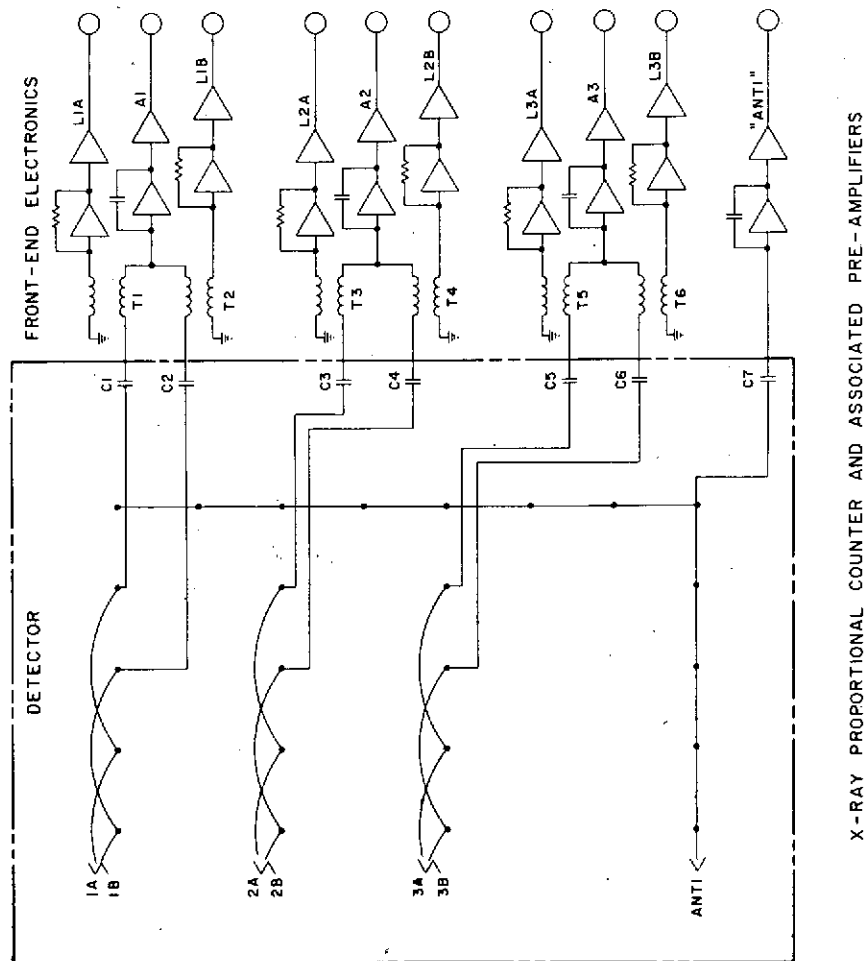


Figure 3.3 - X-ray proportional counter front-end electronics with the wiring of the cells, pulse transformers, and pre amplifiers shown, for the rocket experiments.

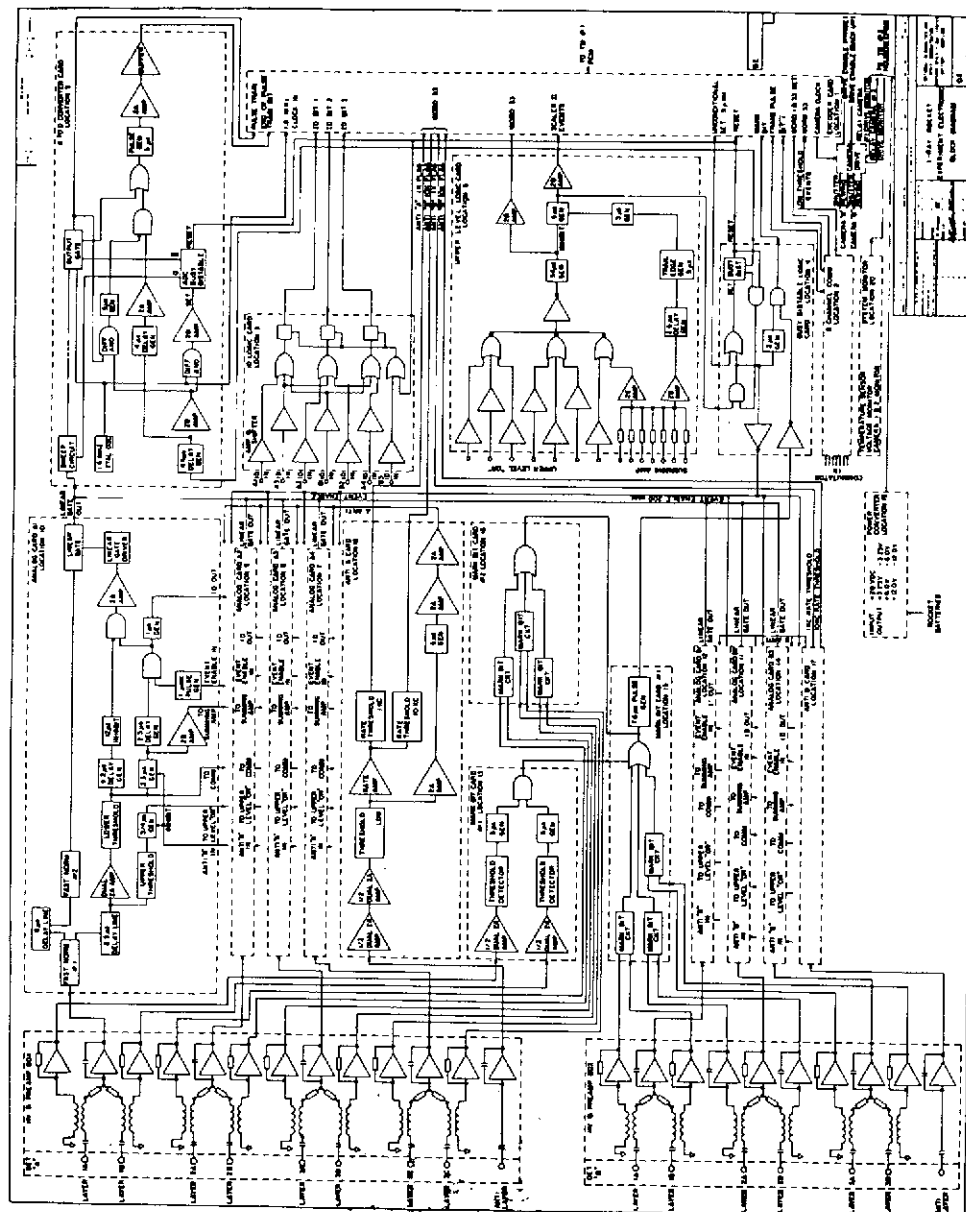


Figure 3.4 - Block diagram of the electronics system used for the balloon and rocket experiments.

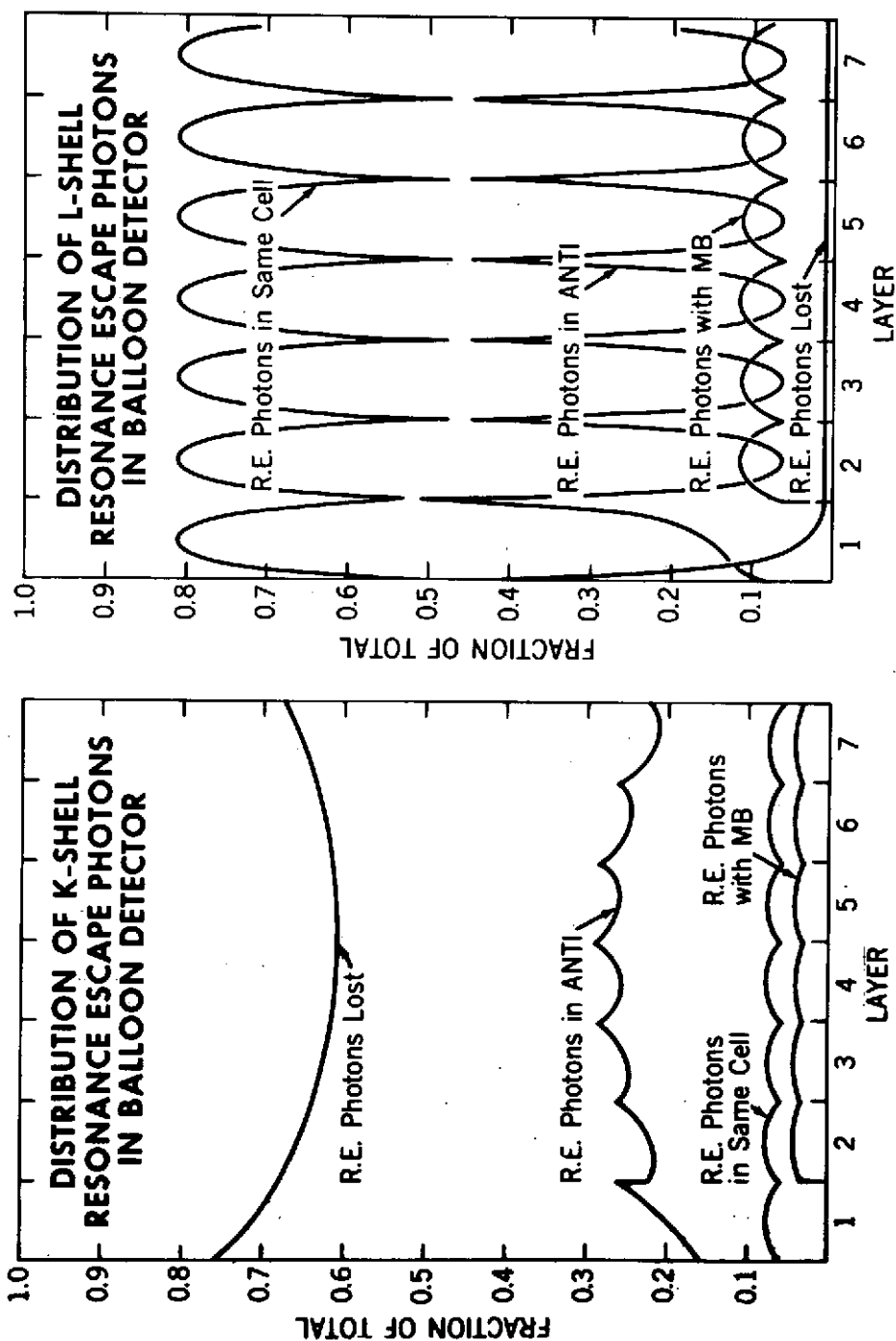


Figure 3.5 - Distribution of characteristic photons leaving a cell (resonance escape) and remaining in the same cell for the K- and L-shell in the balloon experiment as a function of depth (layer).

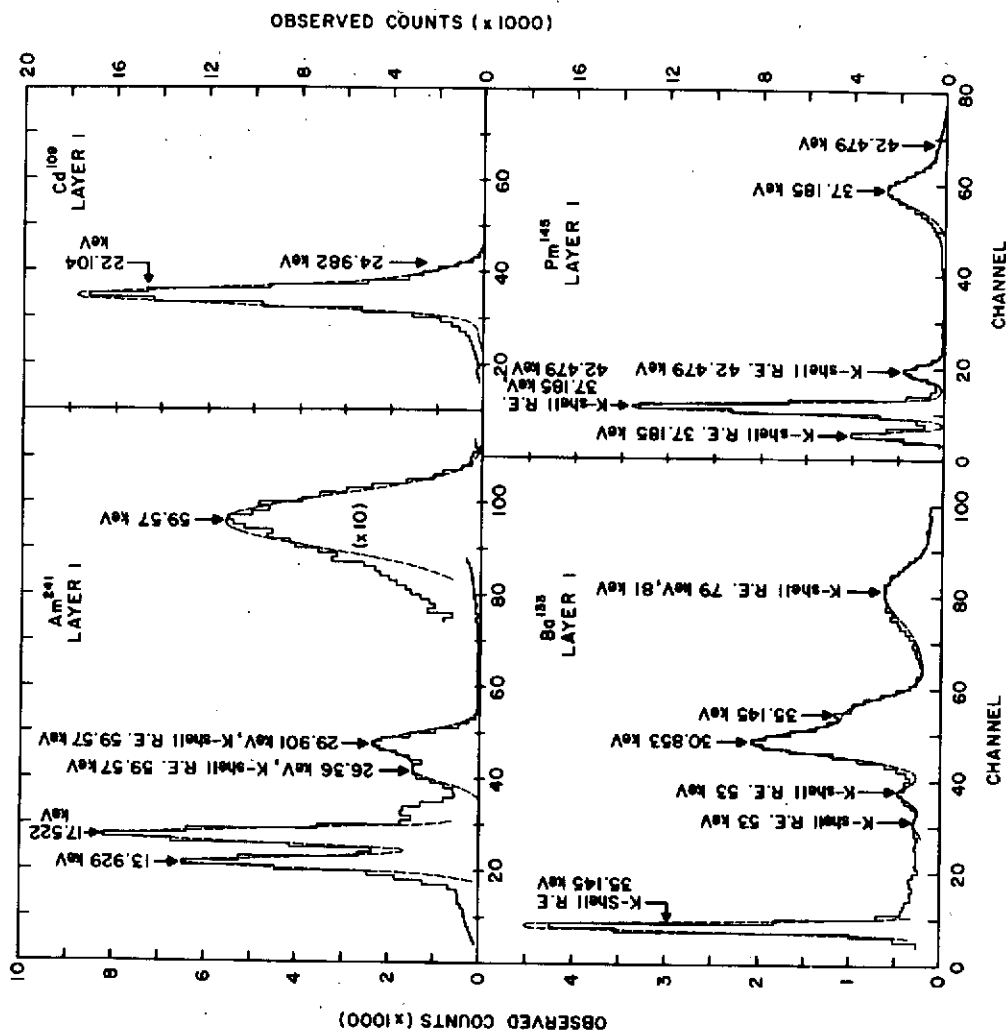


Figure 3.6 - Observed and computed response of layer 1 of the balloon experiment to the laboratory calibration sources Am^{241} , Cd^{109} , Ba^{133} , and Pm^{145} .

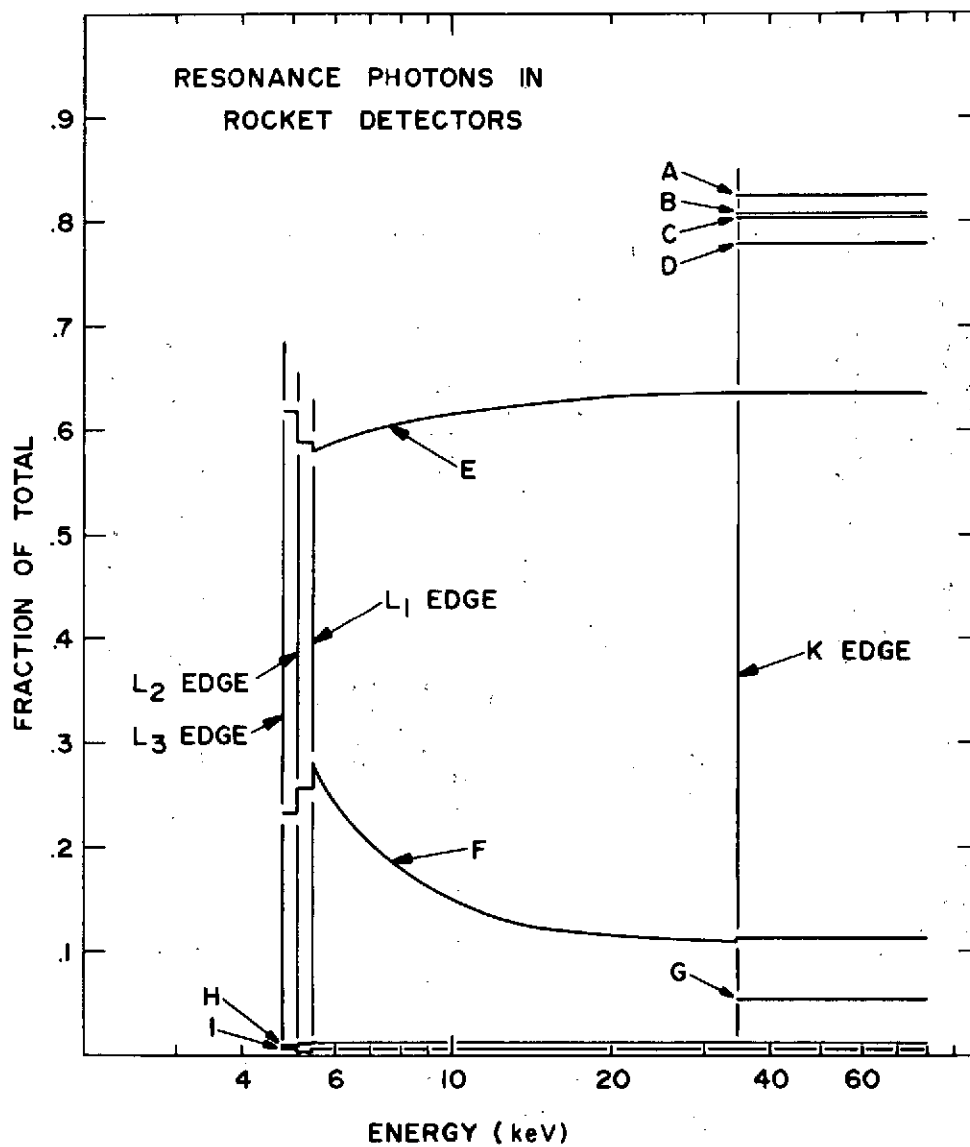


Figure 3.7 - Fractions of characteristic photons leaving the detector (resonance escape, RE) and remaining in the same cell (SC) for the rocket experiment. The data presented are (A) K-shell RE for layer 2, detector A, (B) K-RE for 3A, (C) K-RE for 1B, (D) K-RE for 2B and 3B, (E) L-SC for all layers, (F) L-RE for 1B and 2A, (G) K-SC for all layers, (H) L-RE for 3A, (I) L-RE for 2B and 3B.

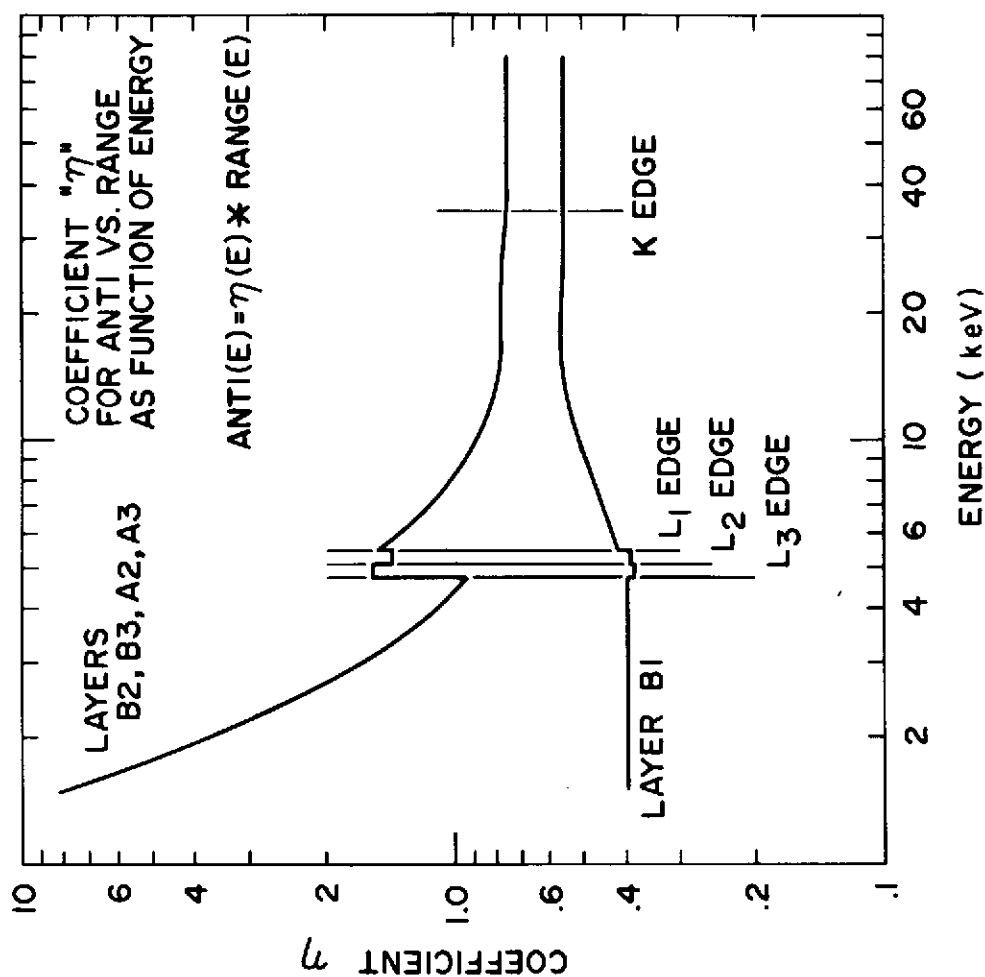


Figure 3.8 - Computed electron antineutrino coefficient as a function of energy for the rocket experiment.

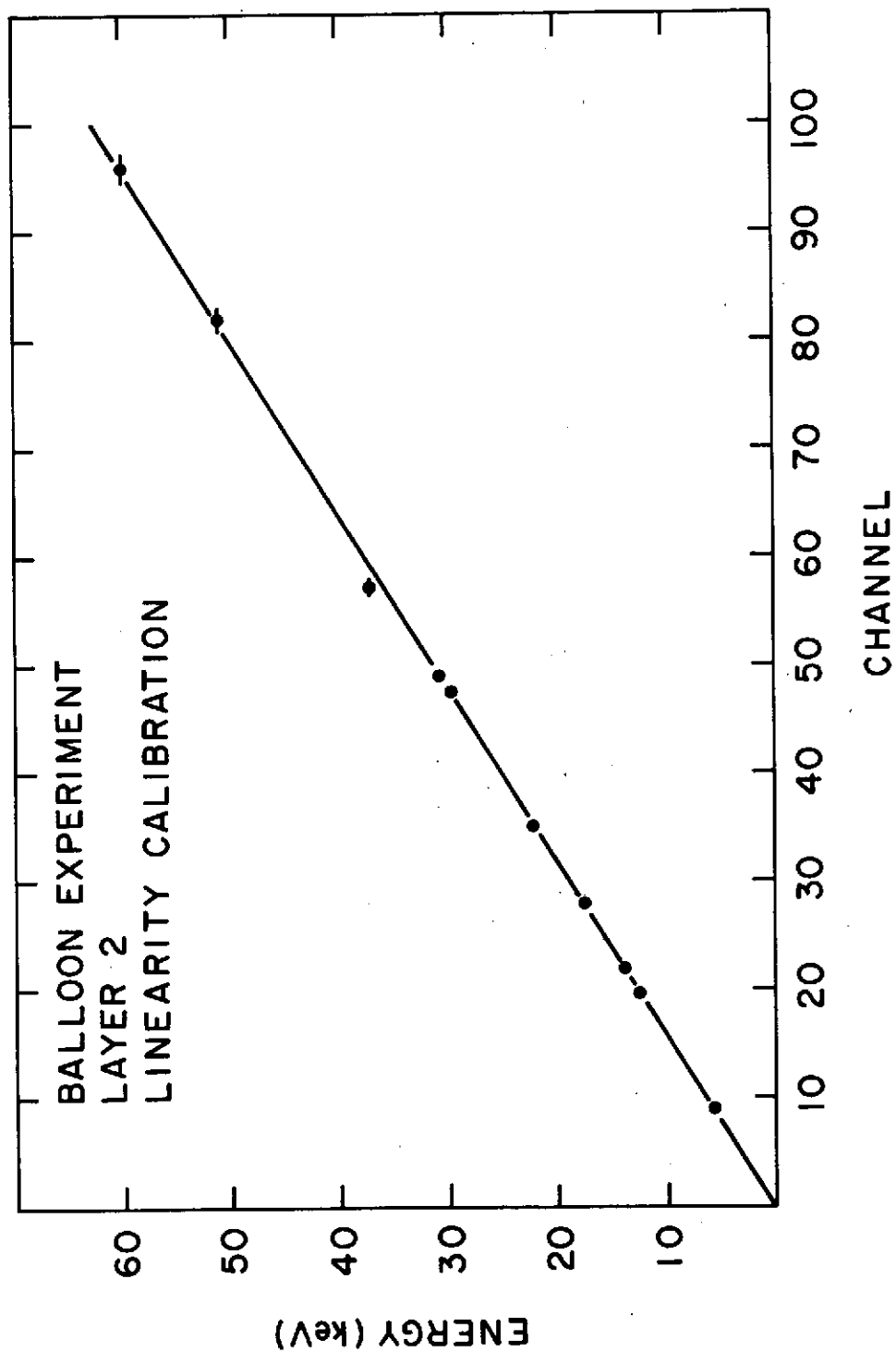


Figure 3.9 - X-ray energy vs. channel number (linearity calibration) for layer 2 of the balloon experiment as determined with laboratory calibration sources.

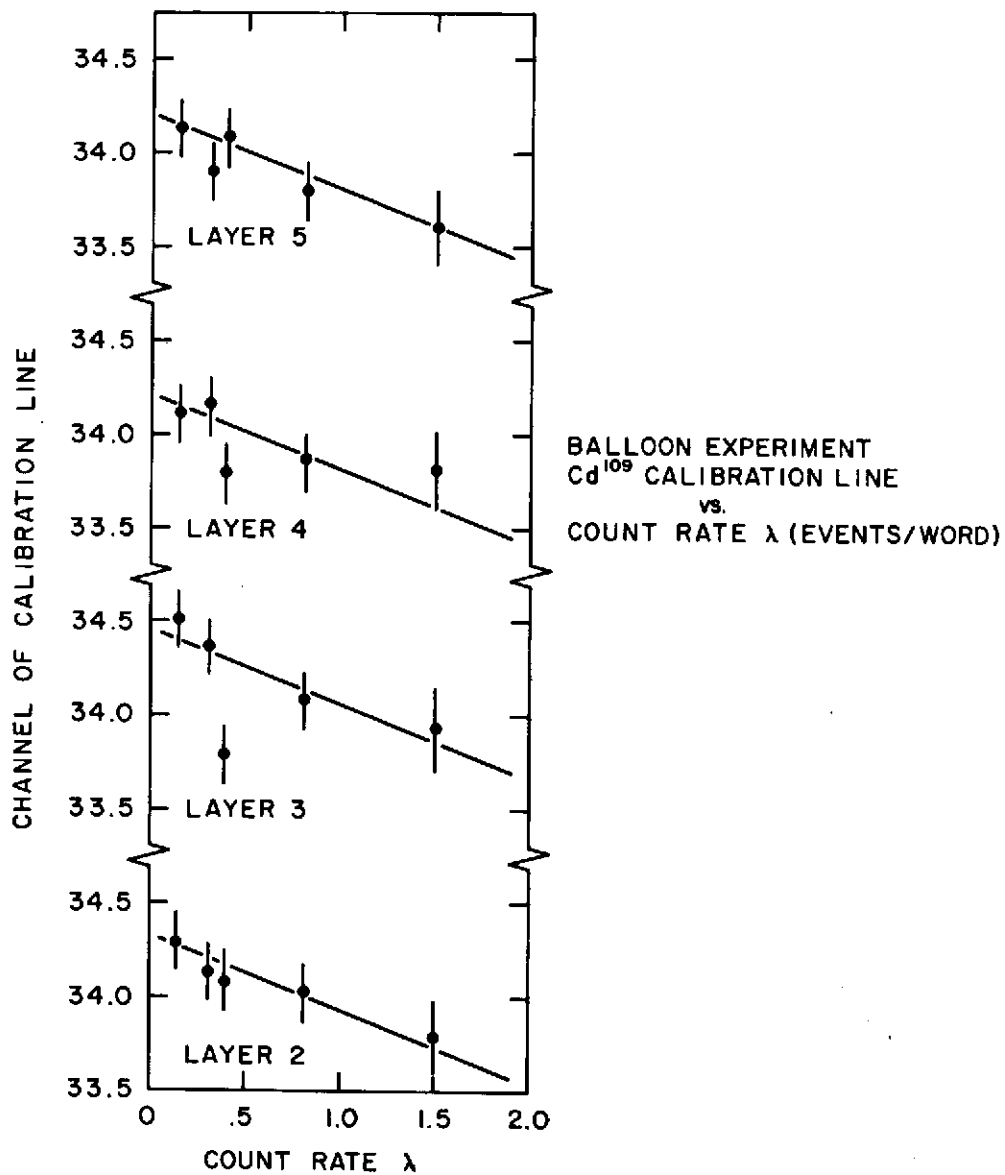


Figure 3.10 - Channel number for a Cs^{109} calibration source as a function of count rate.

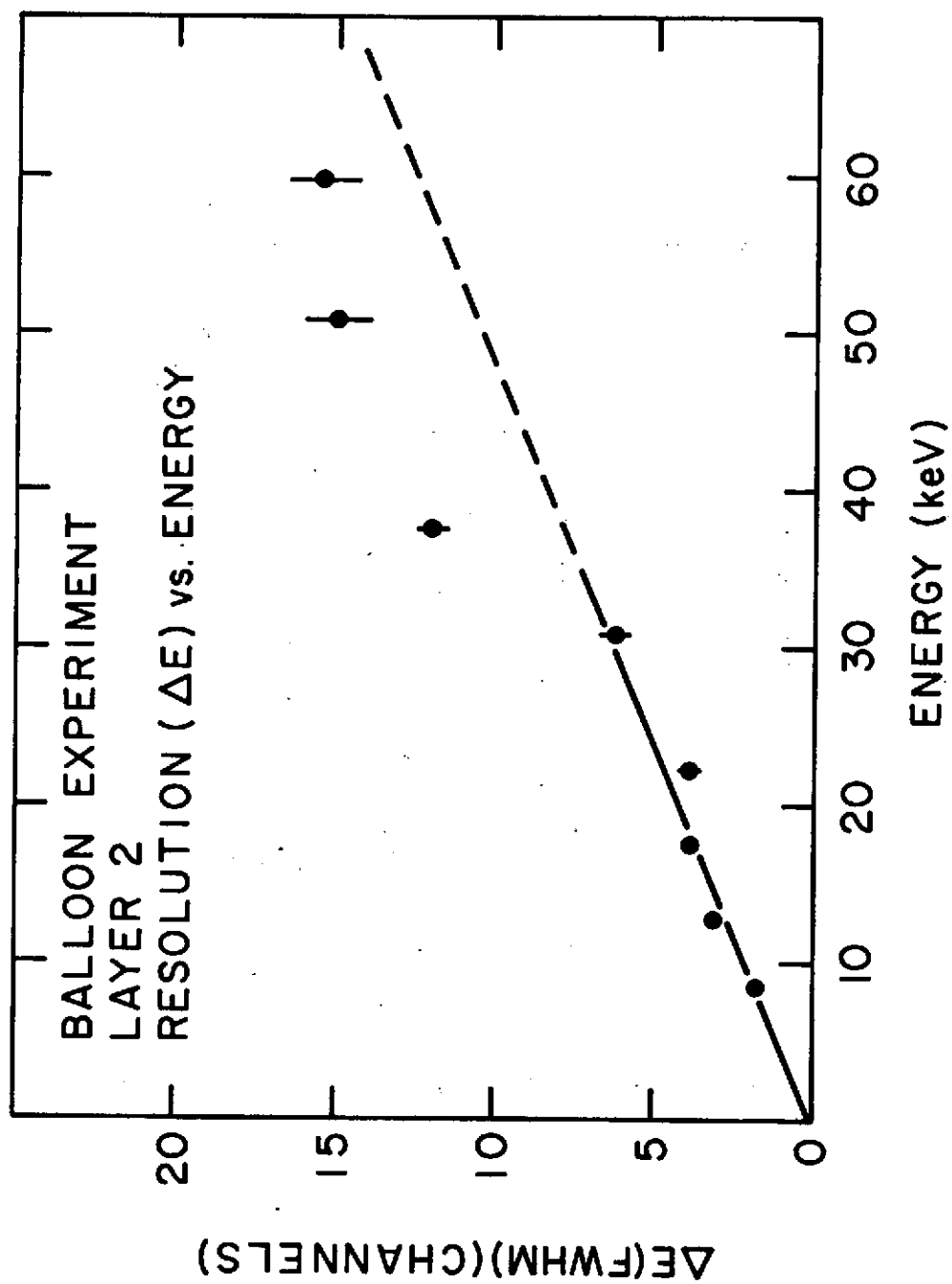


Figure 3.11 - Observed widths of lines from calibration sources as a function of energy in layer 2 of the balloon experiment.

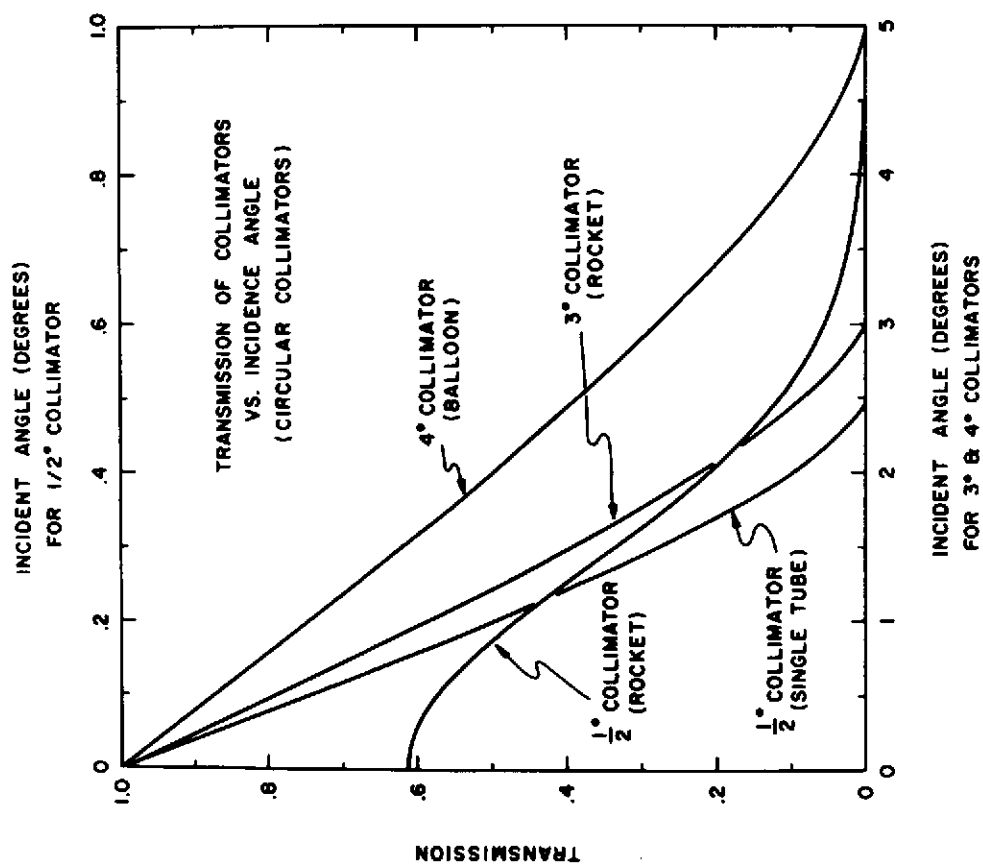


Figure 3.12 - Transmission efficiency of the collimator on the balloon and rocket experiments as a function of offset angle.

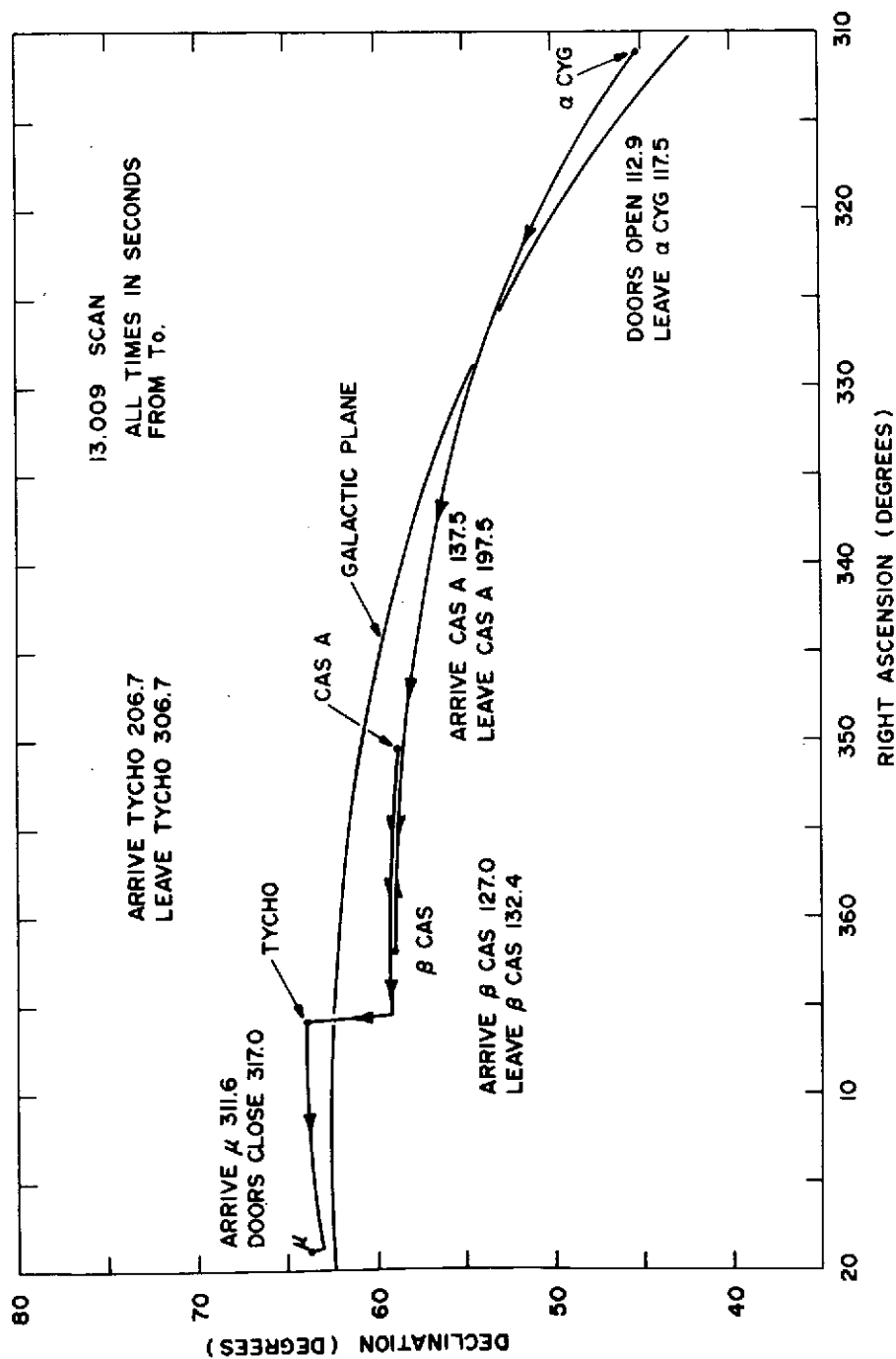


Figure 4.1 - Sky scan of sounding rocket experiment 13.009 showing times in seconds at which key milestones were reached.

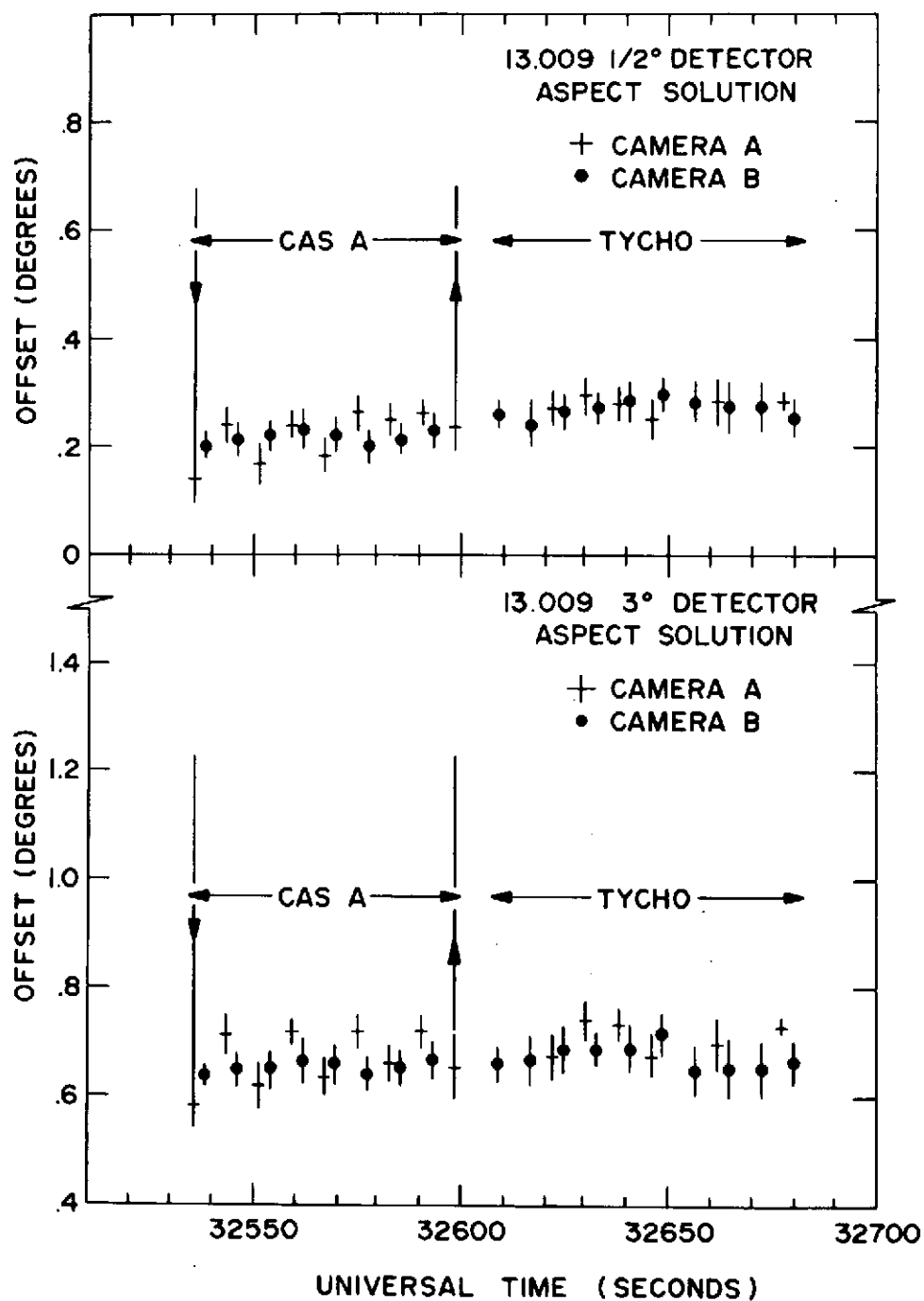


Figure 4.2 - Aspect solution for sounding rocket experiment 13.009 showing offsets in degrees from the intended targets. The error bars represent statistical errors in the aspect solution only, and do not include systematic errors of $\pm 6.1'$ and $\pm 3.2'$ for the 3° and $1/2^\circ$ detector, respectively.

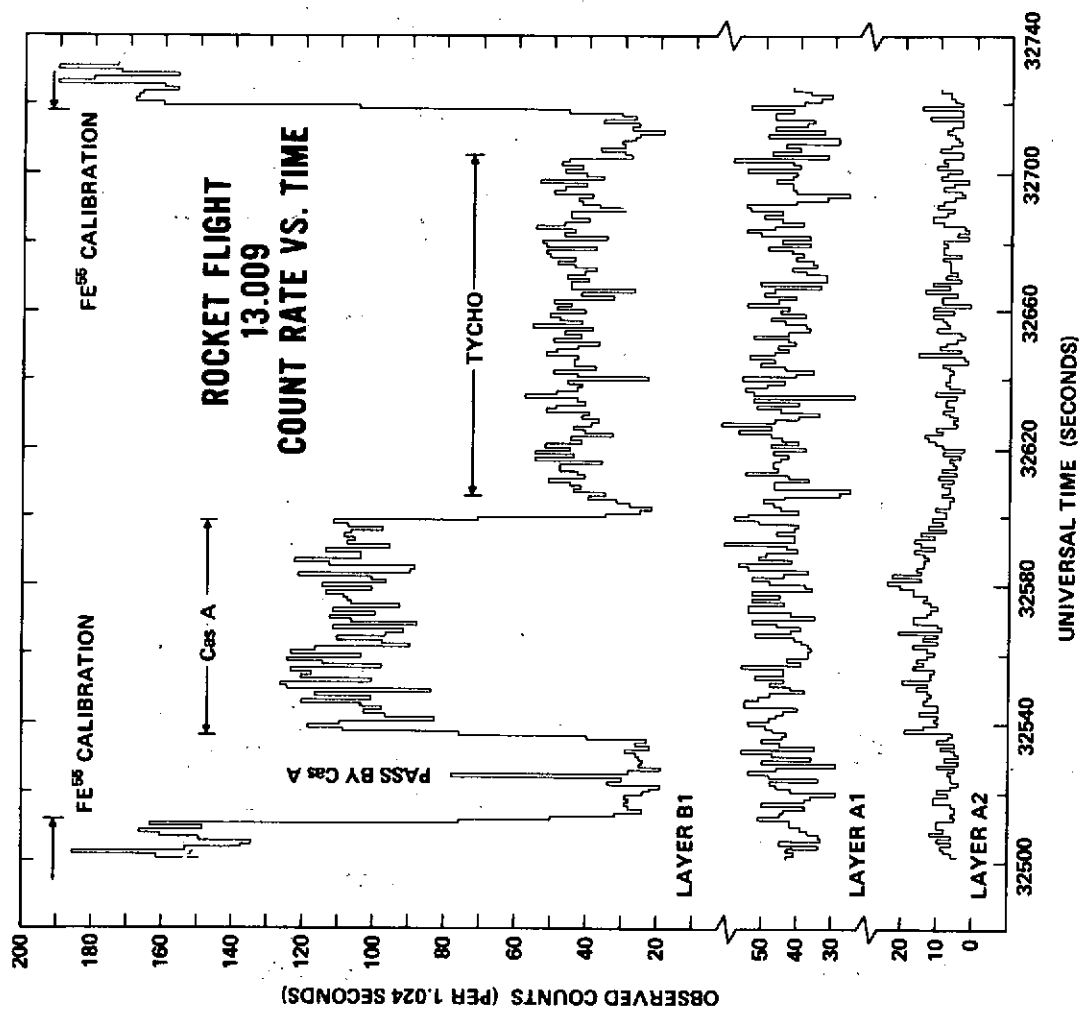
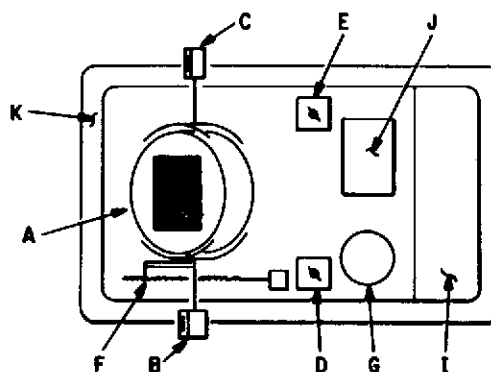
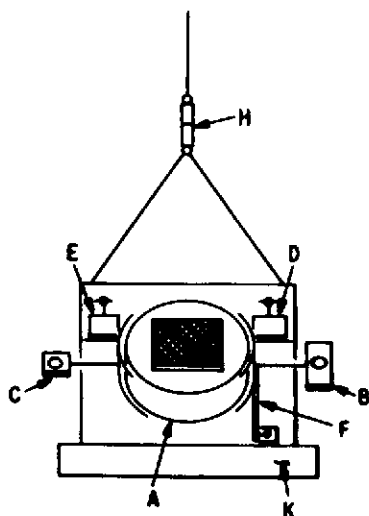


Figure 4.3 - Observed count rate as a function of time for rocket flight 13.009 for layers B1, A1 and A2.

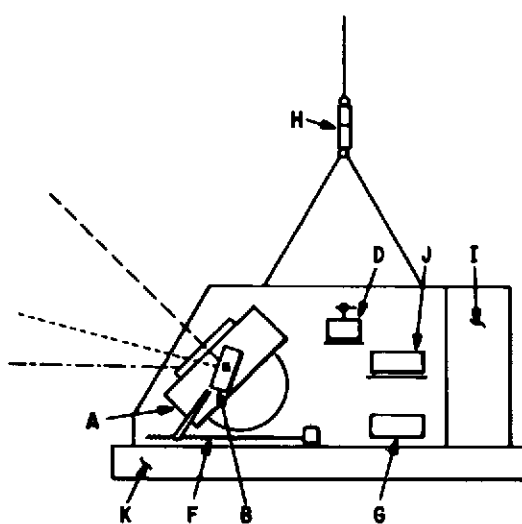
X-RAY EXPERIMENT BALLOON GONDOLA



TOP VIEW



FRONT VIEW



SIDE VIEW

Figure 4.4 - Sketch of balloon gondola, pointing out relative location of (A) detector in swivel mount, (B) experiment camera, (C) gondola system camera, (D) guidance magnetometer, (E) fine readout magnetometer, (F) elevation drive, (G) inertia wheel, (H) momentum unloader, (I) electronics and computer storage bin, (J) power supplies and converters, (K) crush pad, and (L) cable to parachute and balloon.

BALLOON FLIGHT 683-P JUNE 20, 1972

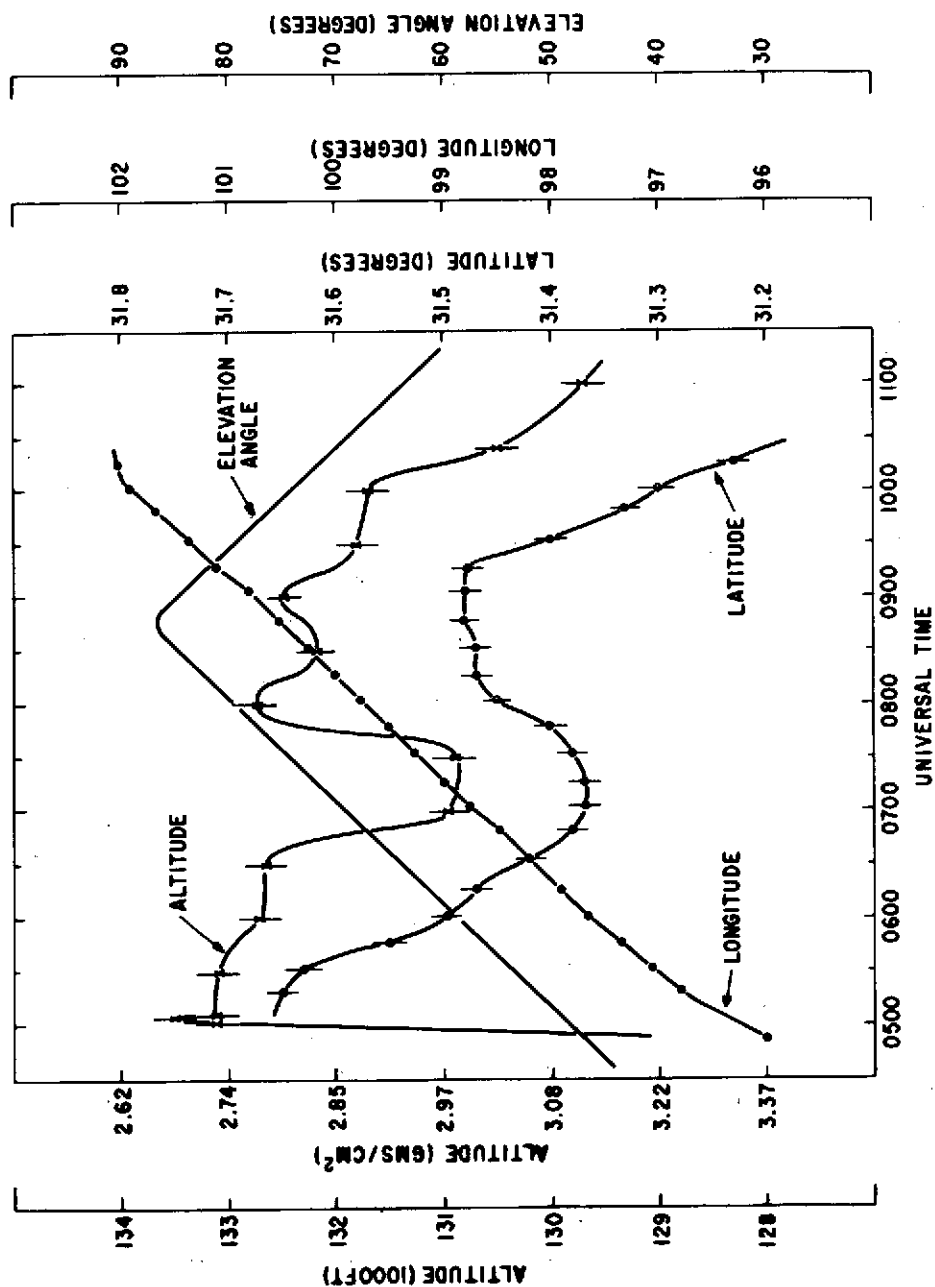


Figure 4.5 - Ephemeris for balloon flight 683-P. Displayed are the latitude, longitude, altitude, and elevation angle of the detector.

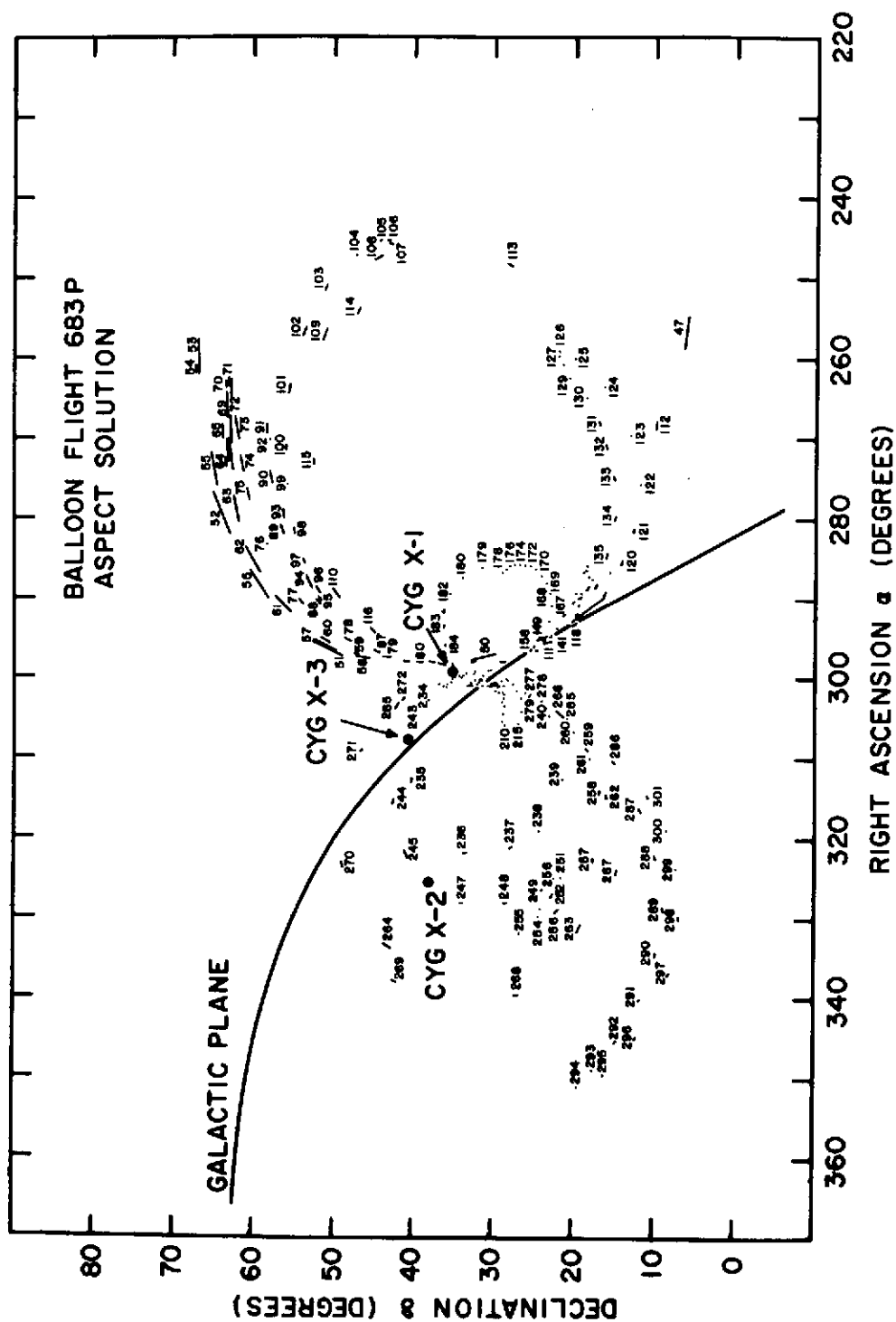


Figure 4.6 - Celestial position for balloon flight 683-P. Numbers indicate sequential photos, one 3 second exposure every 78.6 seconds.

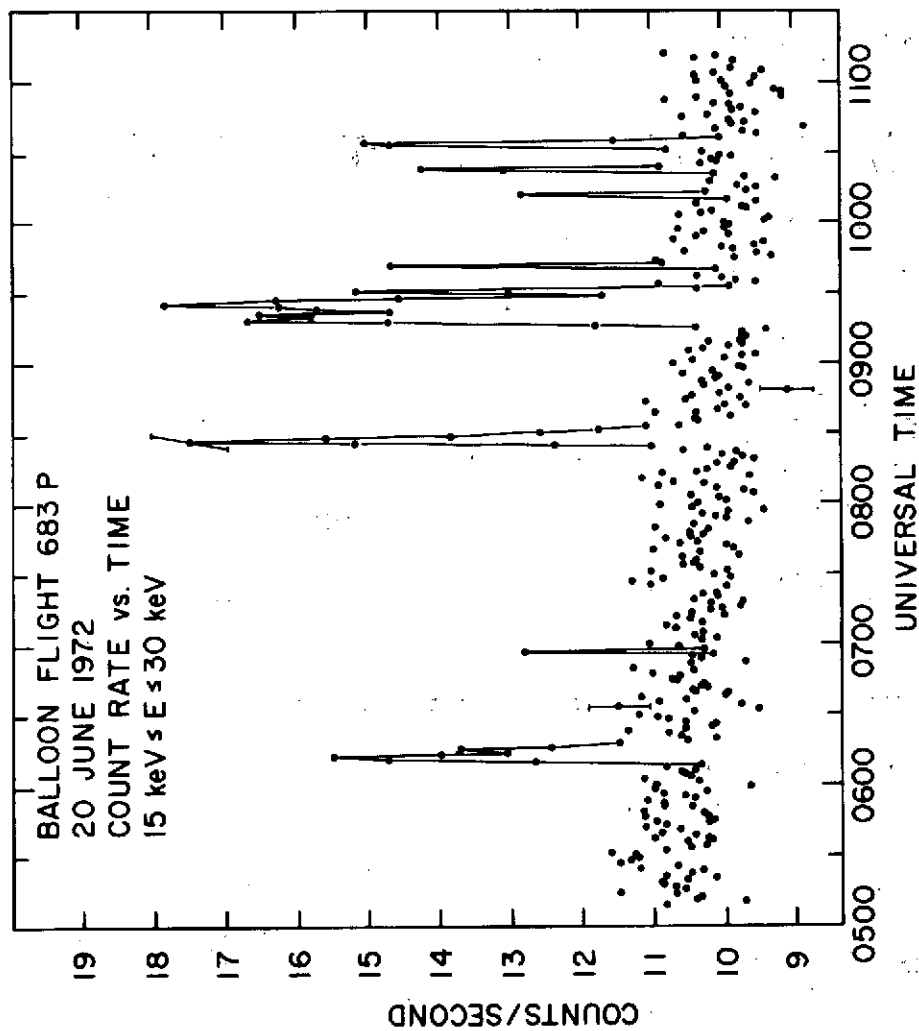


Figure 4.7 - Observed count rate as a function of time for balloon flight 683-P. Data corresponds to the 15 to 30 keV energy band.

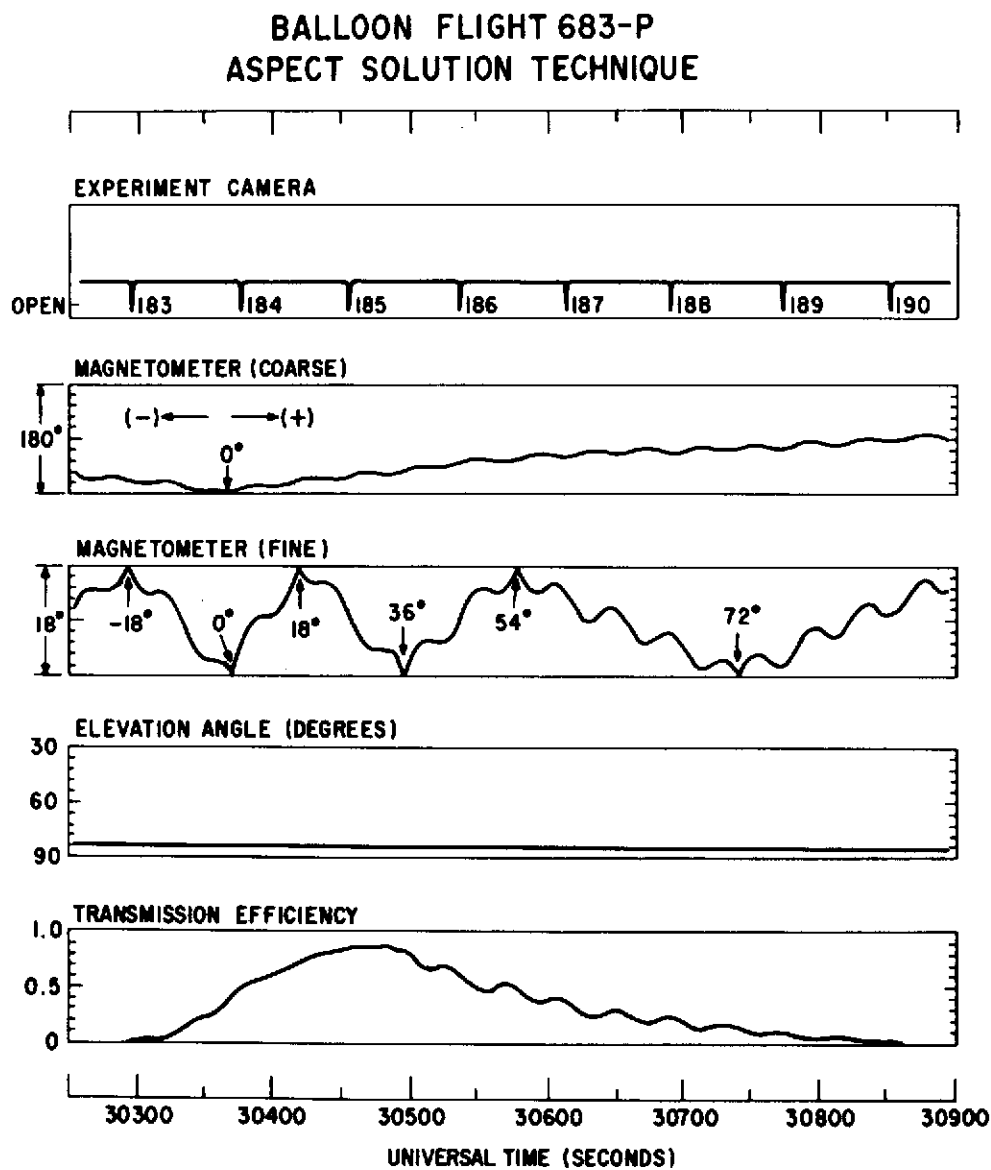


Figure 4.8 - Typical strip chart recordings from balloon flight 683-P showing the experiment camera on-times, coarse and fine readout magnetometer, and elevation angle used to compute the collimator transmission efficiency for X-rays from Cyg X-1.

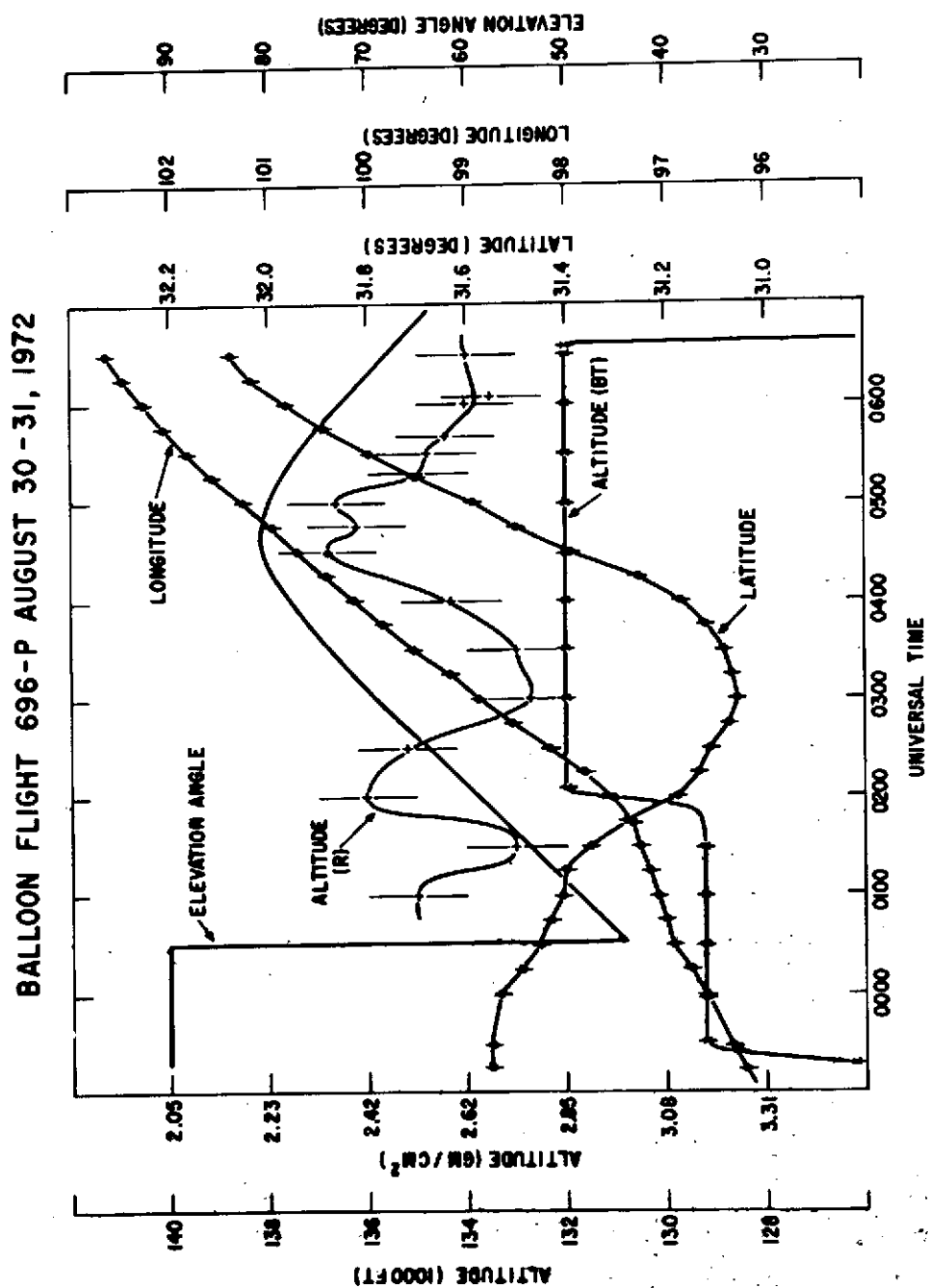


Figure 4.9 - Ephemeris for balloon flight 696-P, showing latitude, longitude, elevation angle, and altitude. Altitude is given separately as determined by the Rosemount pressure transducer (R) and the barotransmitter (BT).

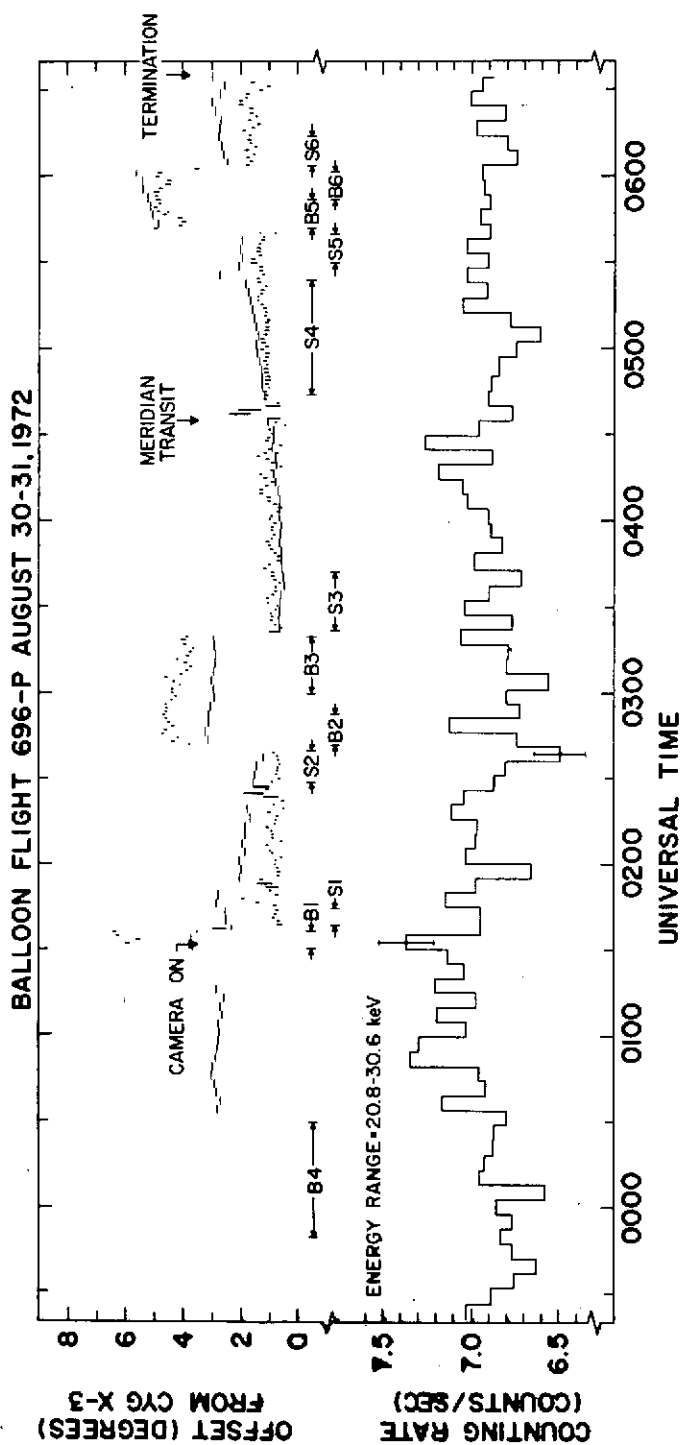


Figure 4.10 - Observed count rate in the 20 to 30 keV band vs. time for balloon flight 696-P. Vertical bars in the upper trace represent the aspect solution as determined by the experiment camera; horizontal bars, by the gondola system.

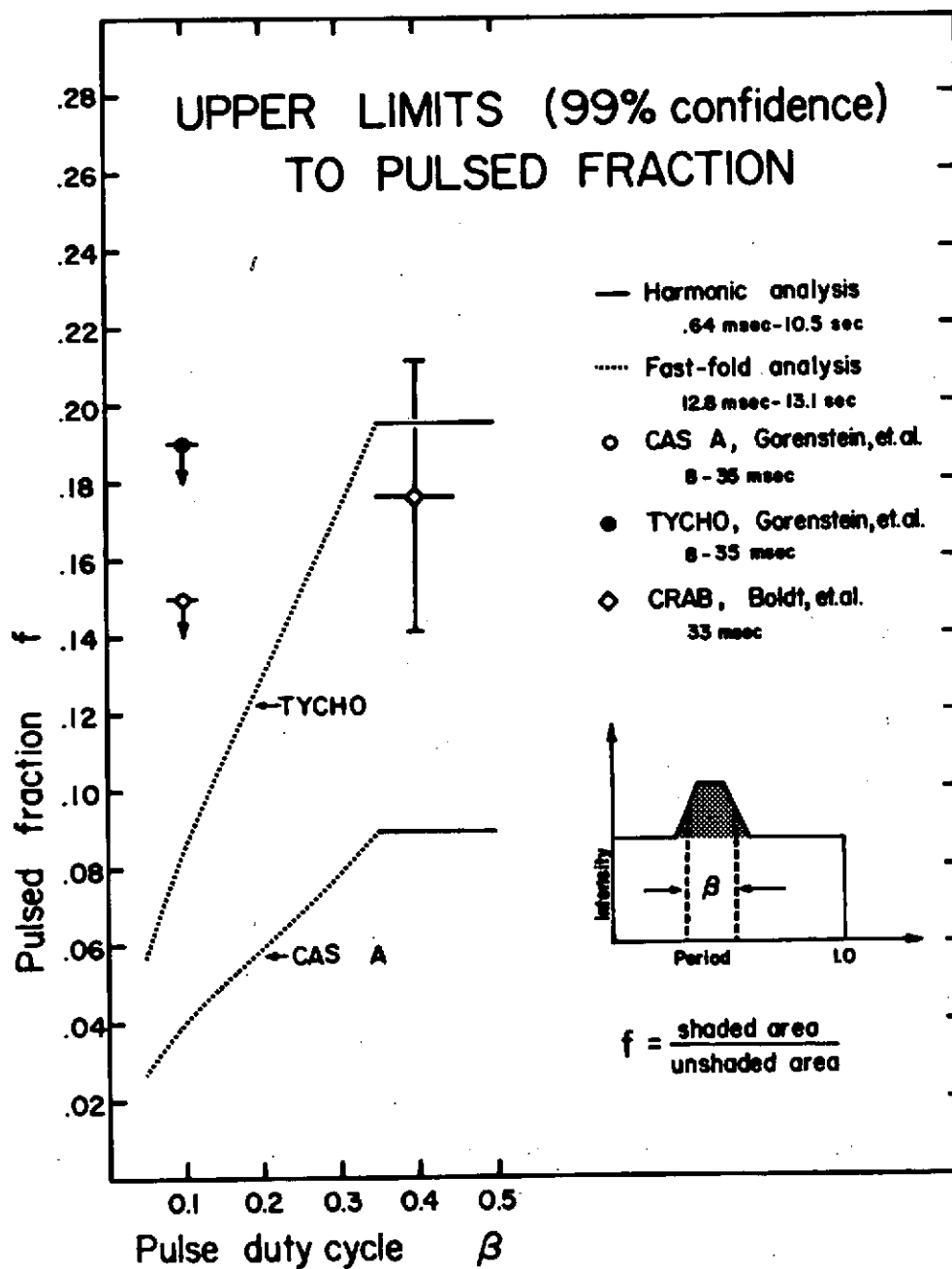


Figure 5.1 - 99% confidence upper limits to the pulsed fraction for Cas A and Tycho, based on Cooley-Tukey harmonic analysis and fast-fold analysis.

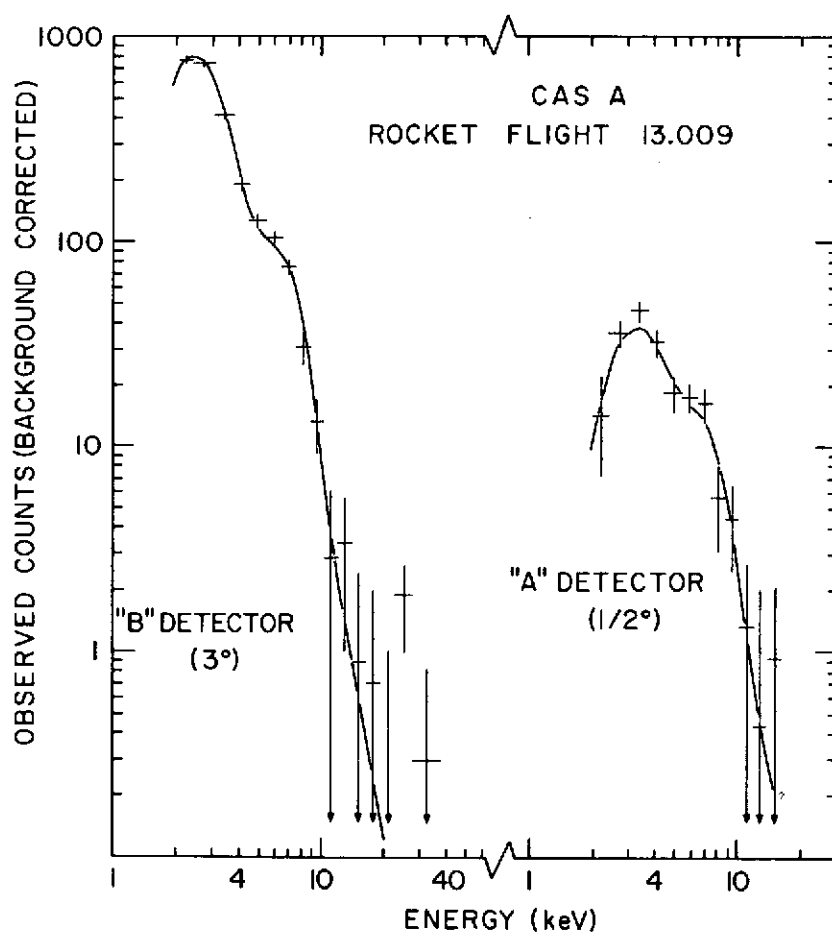


Figure 5.2 - Observed spectra of Cas A with the 3° and 1/2° detectors of the sounding rocket flight 13.009.

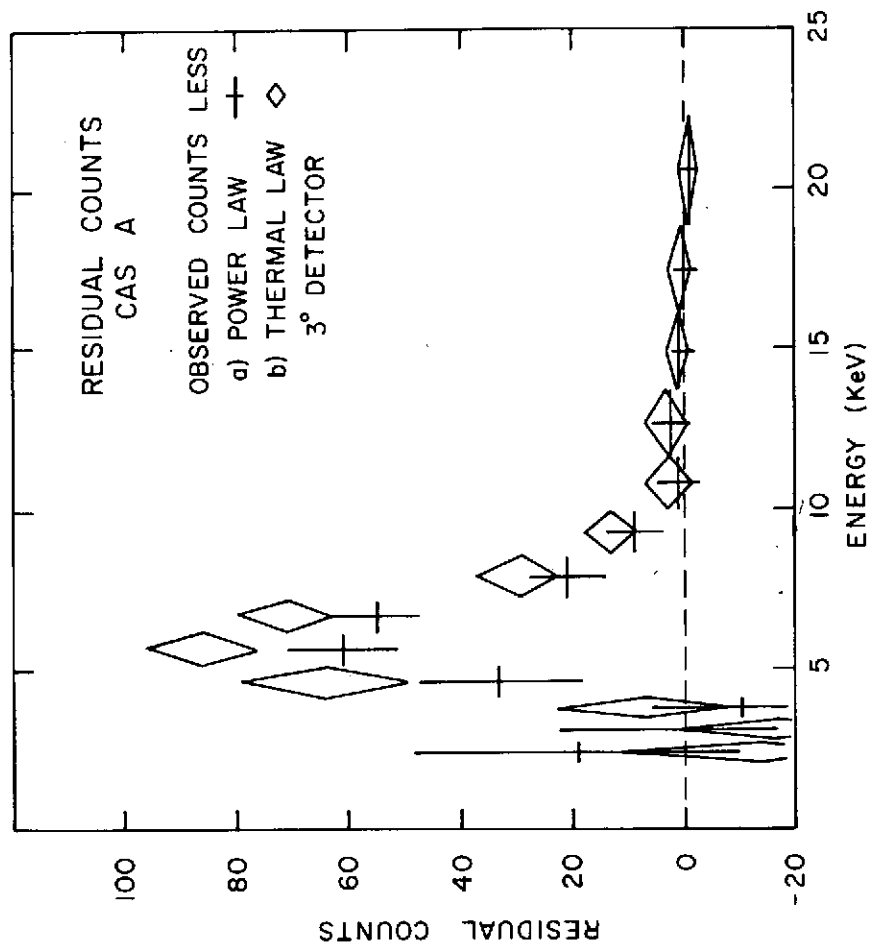


Figure 5.3 - Residual counts after subtracting from the Cas A observed spectrum a computed power law spectrum with an index of 4.35 and a computed exponential spectrum with a temperature of $kT = .83$ keV.

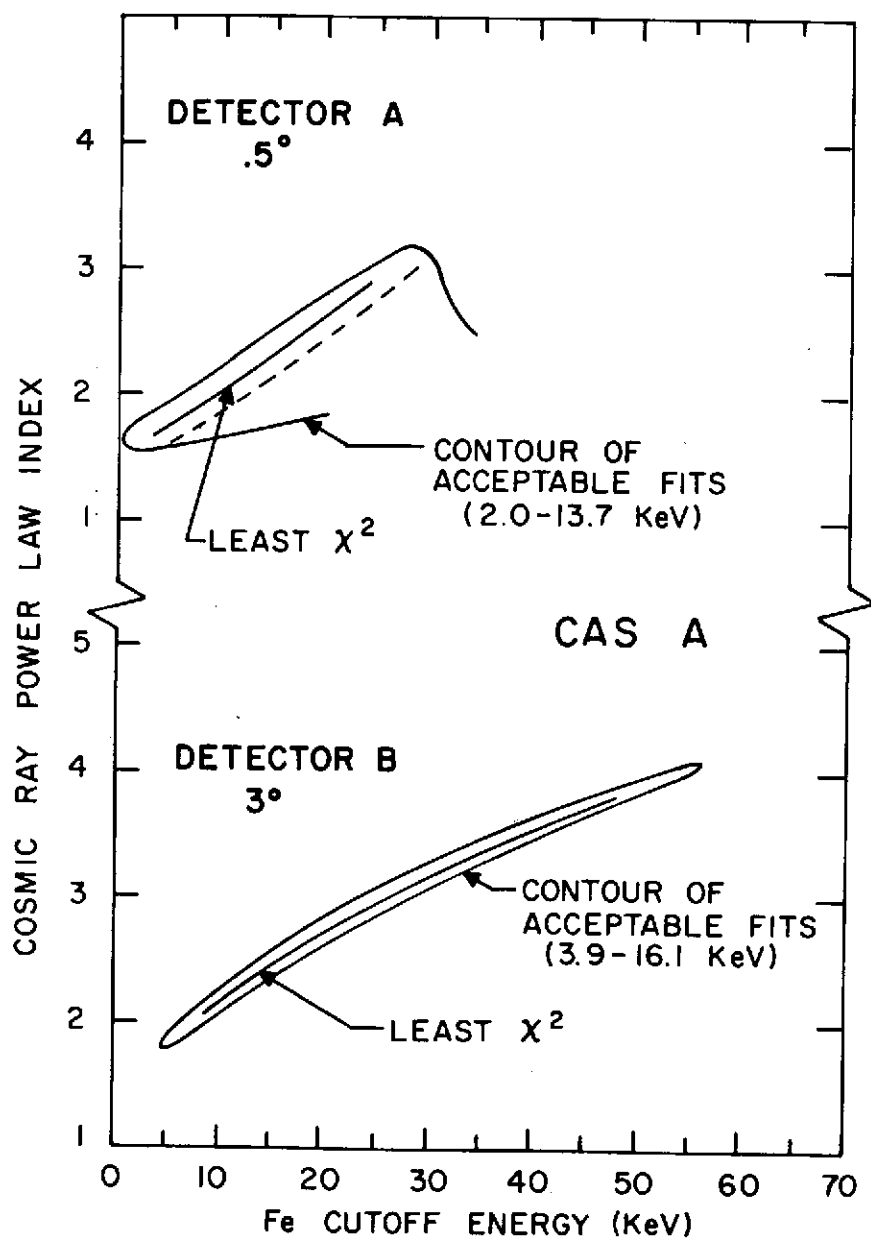


Figure 5.4 - Contours of acceptable χ^2 fits for the Cas A data for cosmic ray power law index vs. the iron low energy cut off.

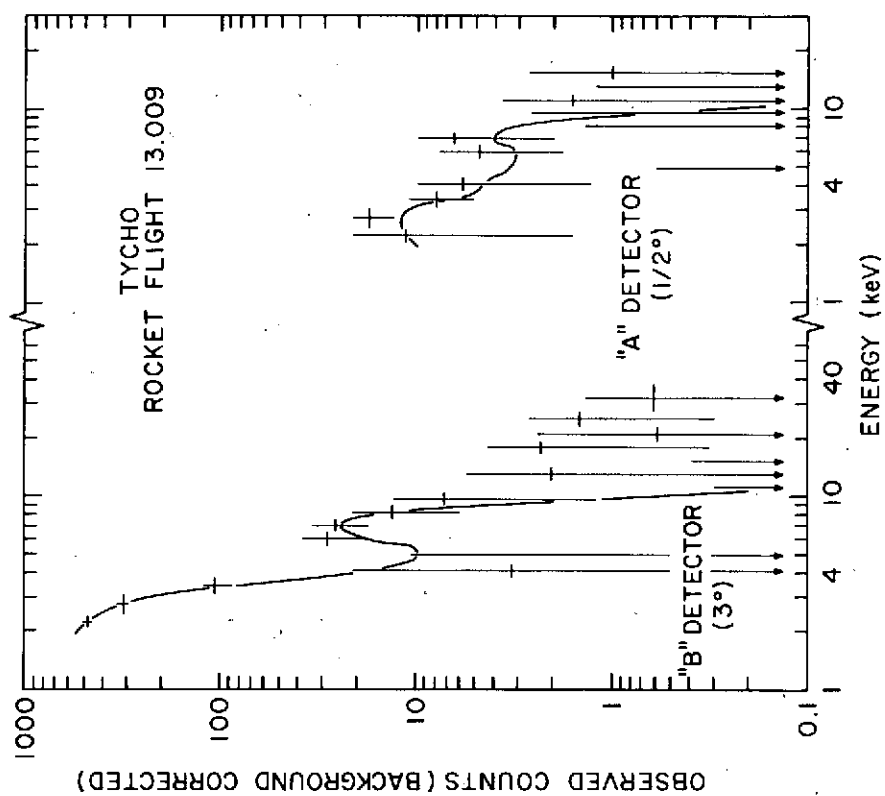


Figure 5.5 - Observed spectra of Tycho with the 3° and 1/2° detectors of the sounding rocket flight 13.009.

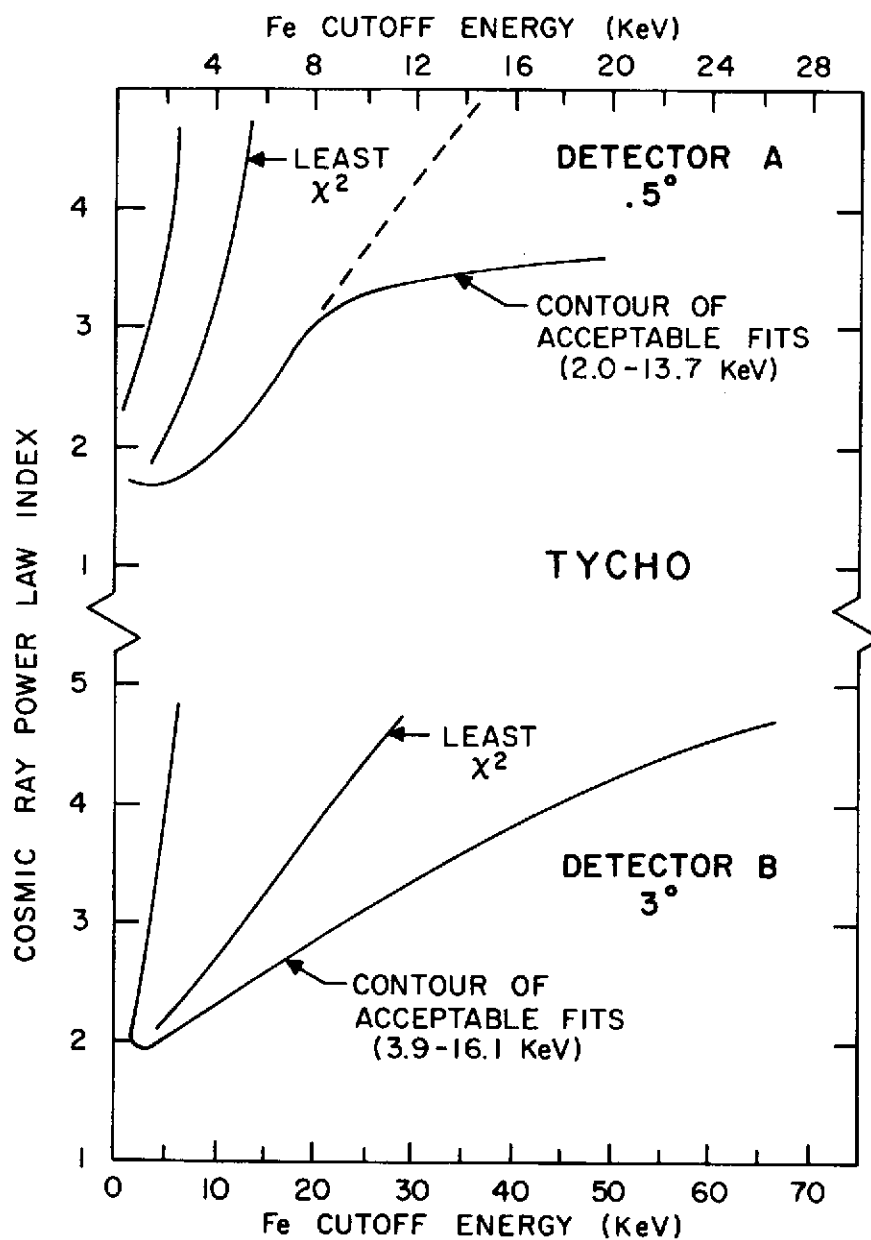


Figure 5.6 - Contours of acceptable χ^2 fits for the Tycho data for cosmic ray power law index vs. the iron low energy cut off.

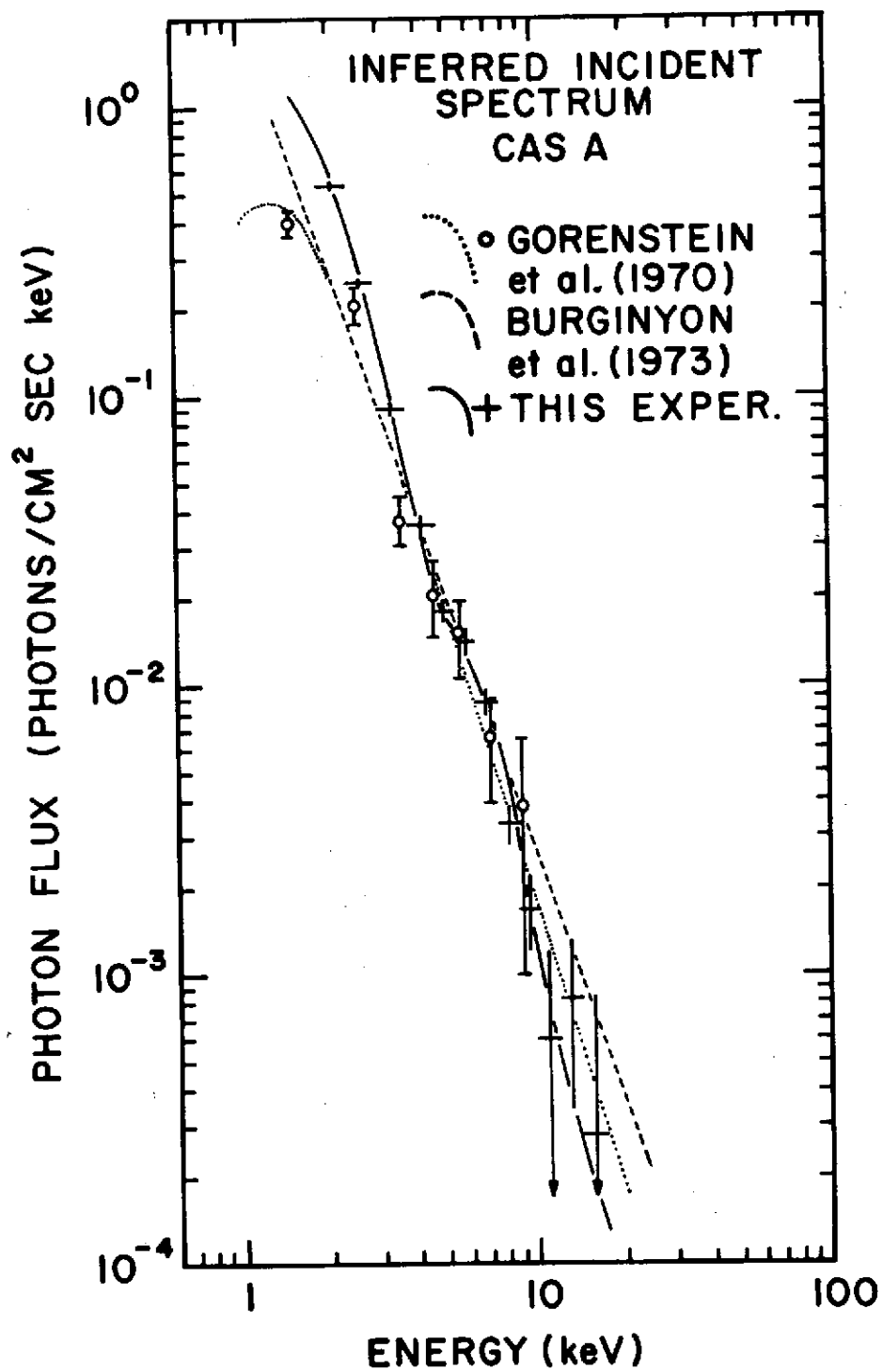


Figure 5.7 - Inferred incident photon spectra of Cas A.

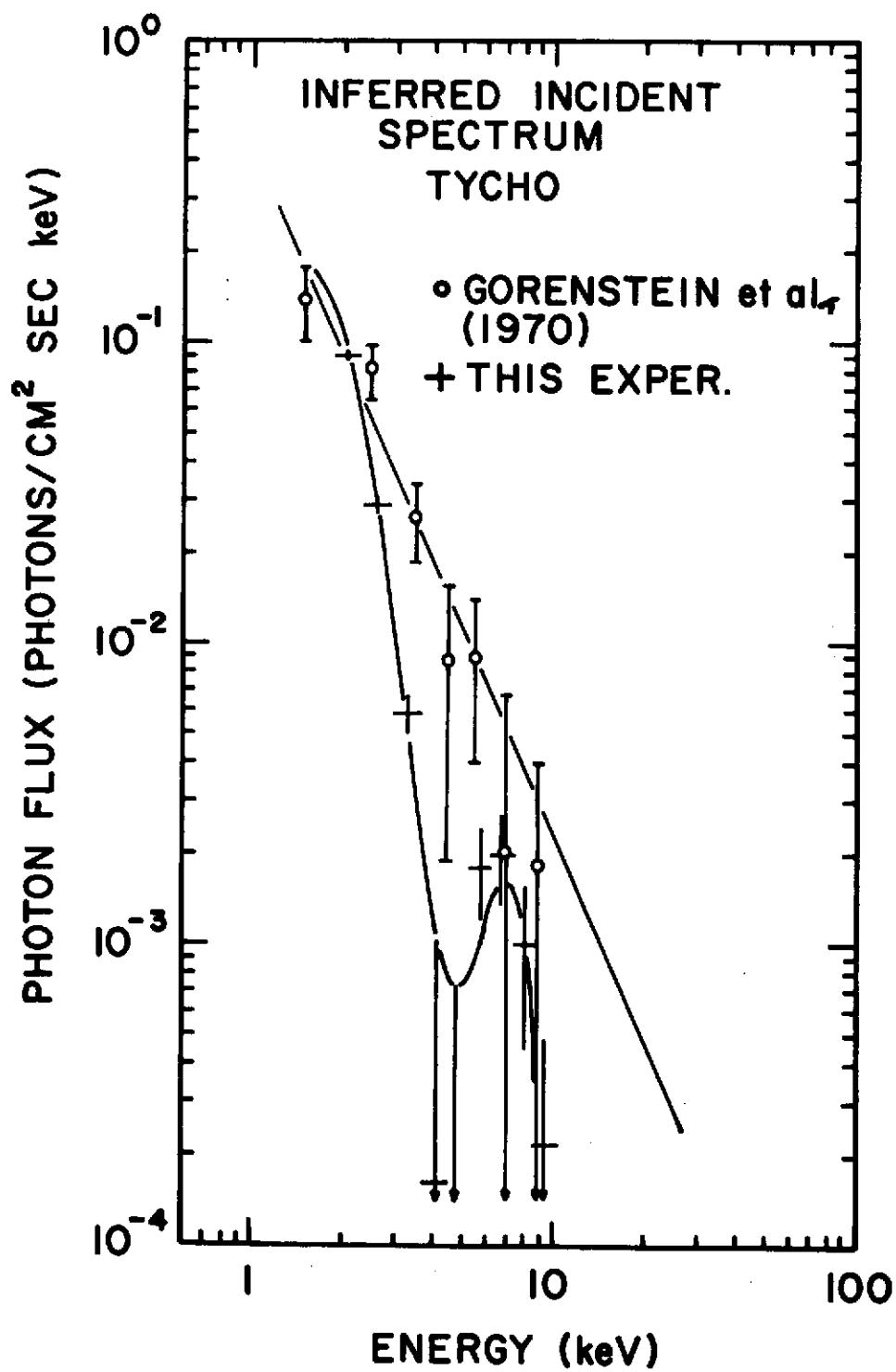


Figure 5.8 - Inferred incident photon spectra from Tycho.

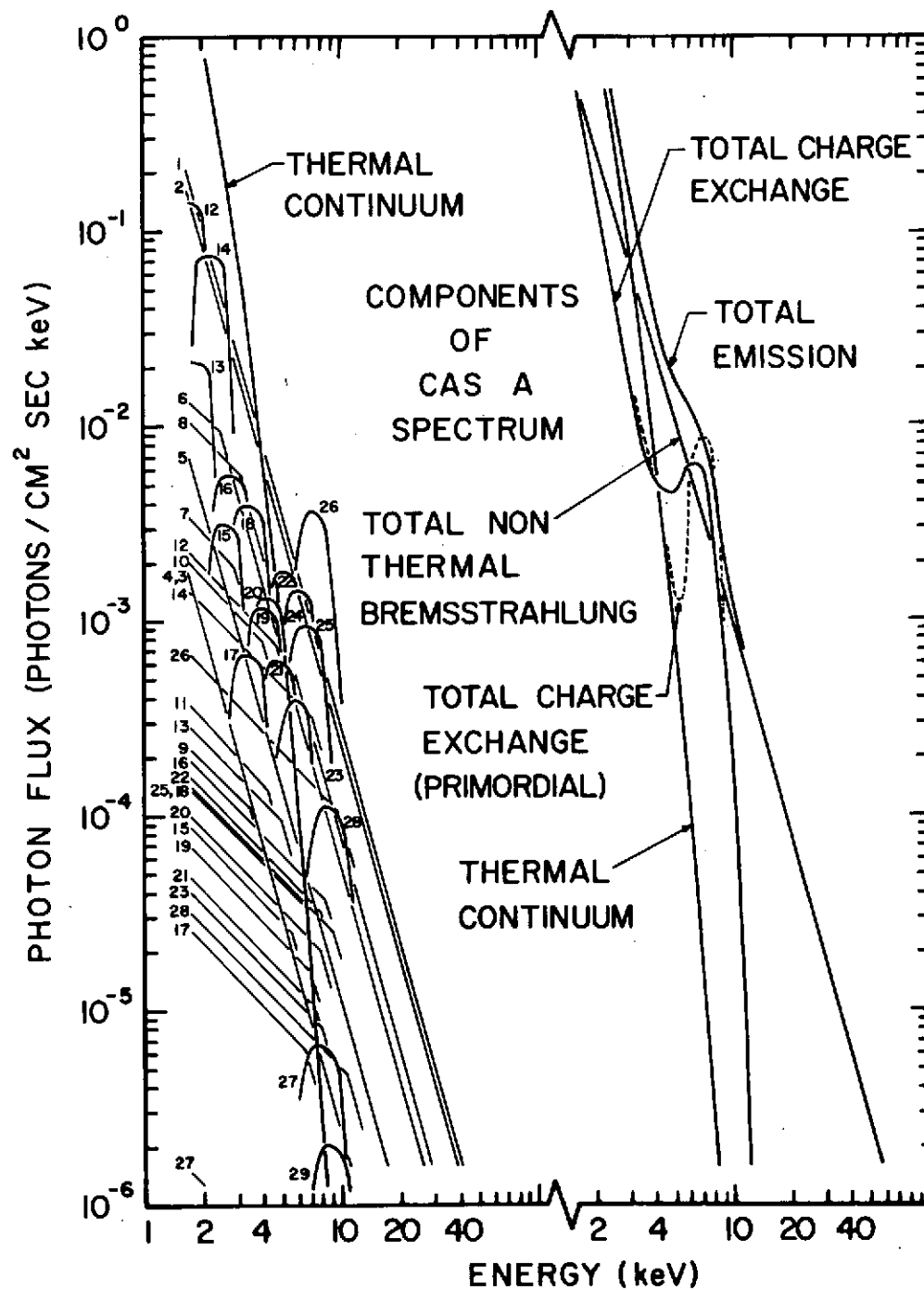


Figure 5.9

Figure 5.9 - The charge exchange, non thermal bremsstrahlung, and thermal bremsstrahlung components of the spectrum which best represents Cas A. The numbers on the left side of the figure represent atomic numbers. Non thermal bremsstrahlung contributions are the power laws; charge exchange contributions are the line features.

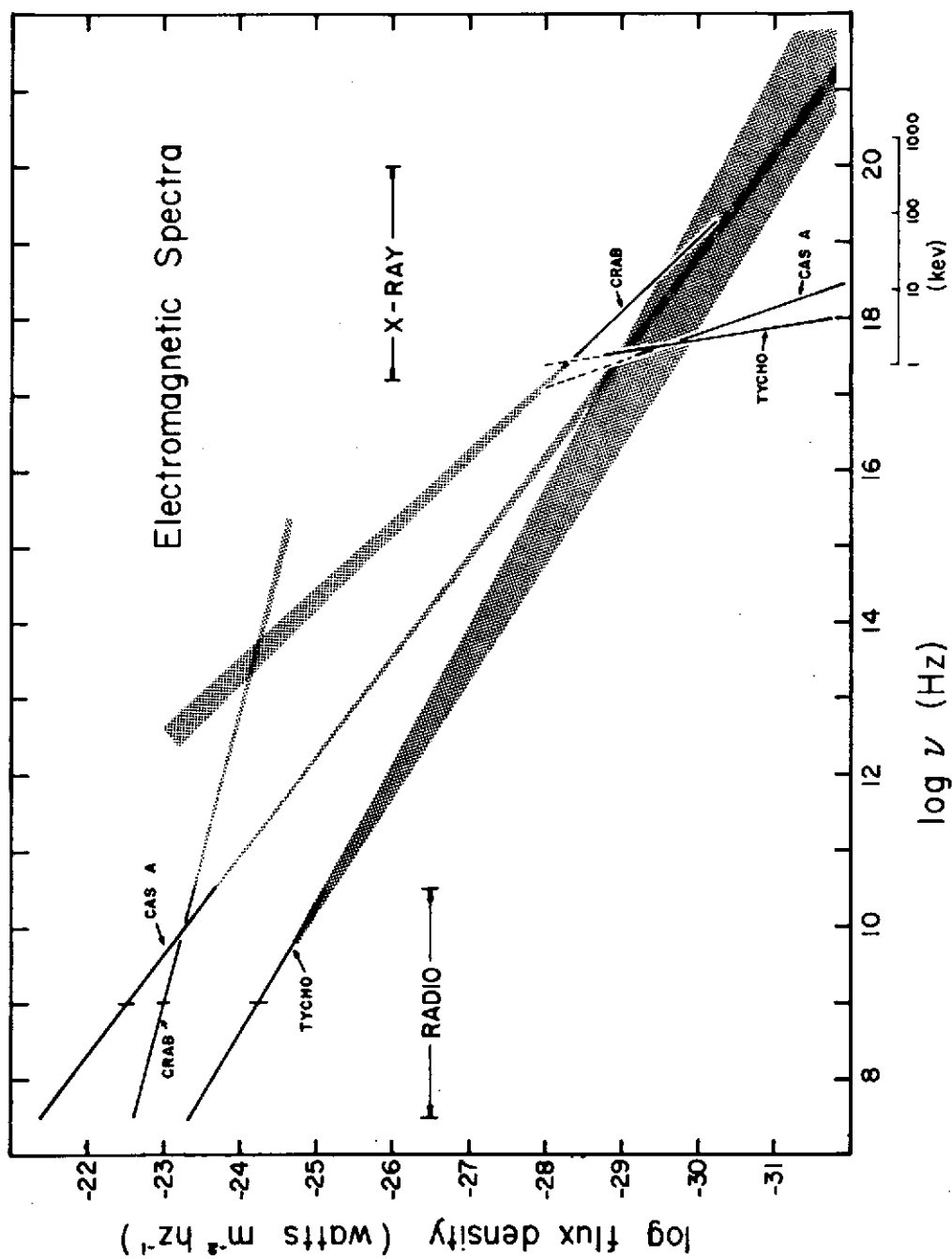


Figure 5.10 - Electromagnetic spectra of the three supernova remnants, the Crab Nebula, Cas A and Tycho.

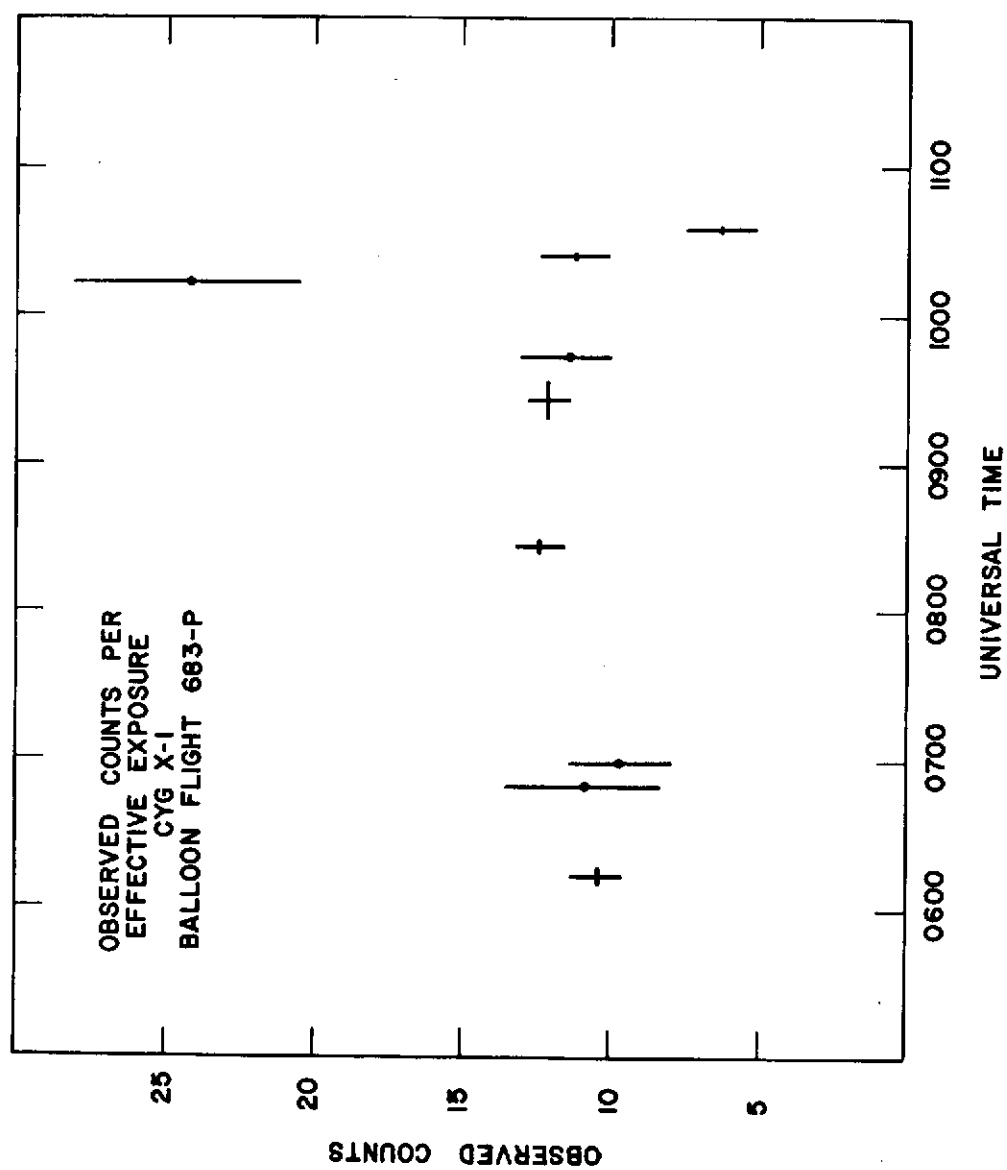


Figure 5.11 - Observed counts in the 13 to 33 keV band per effective exposure for Cyg X-1 during balloon flight 683-P.

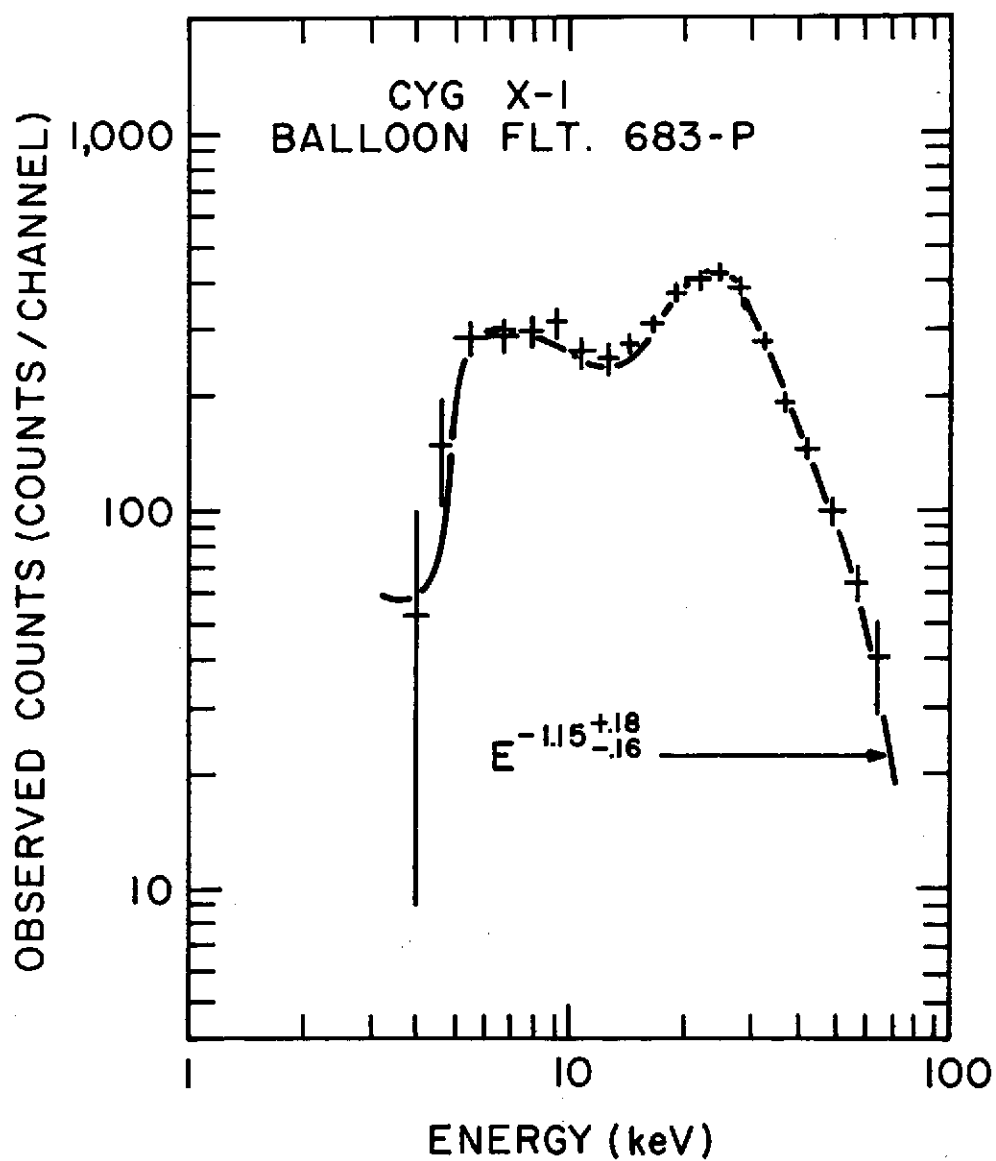


Figure 5.12 - Observed energy spectrum (counts per channel) of Cyg X-1 from balloon flight 683-P.

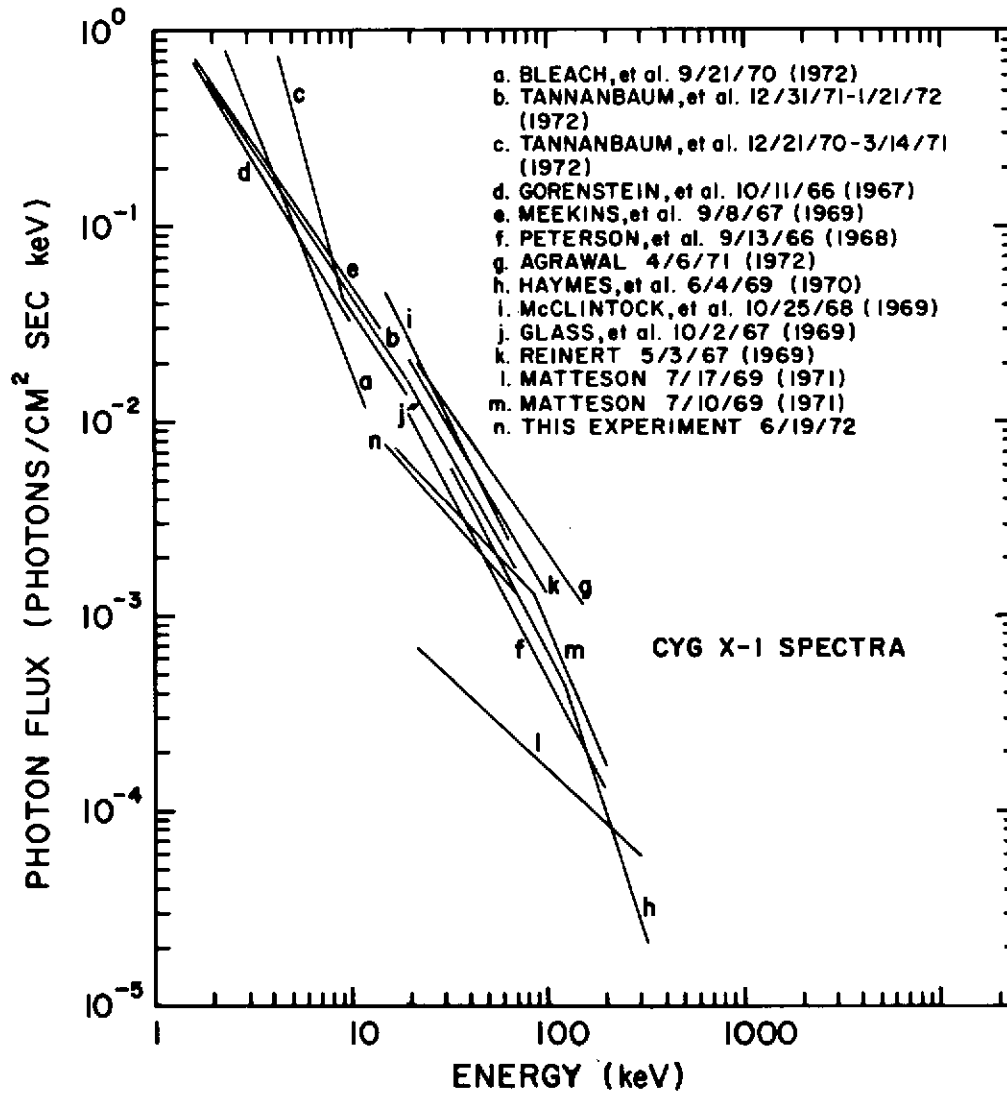


Figure 5.13 - Photon flux (photons/cm²sec keV) of Cyg X-1 as observed by several experiments.

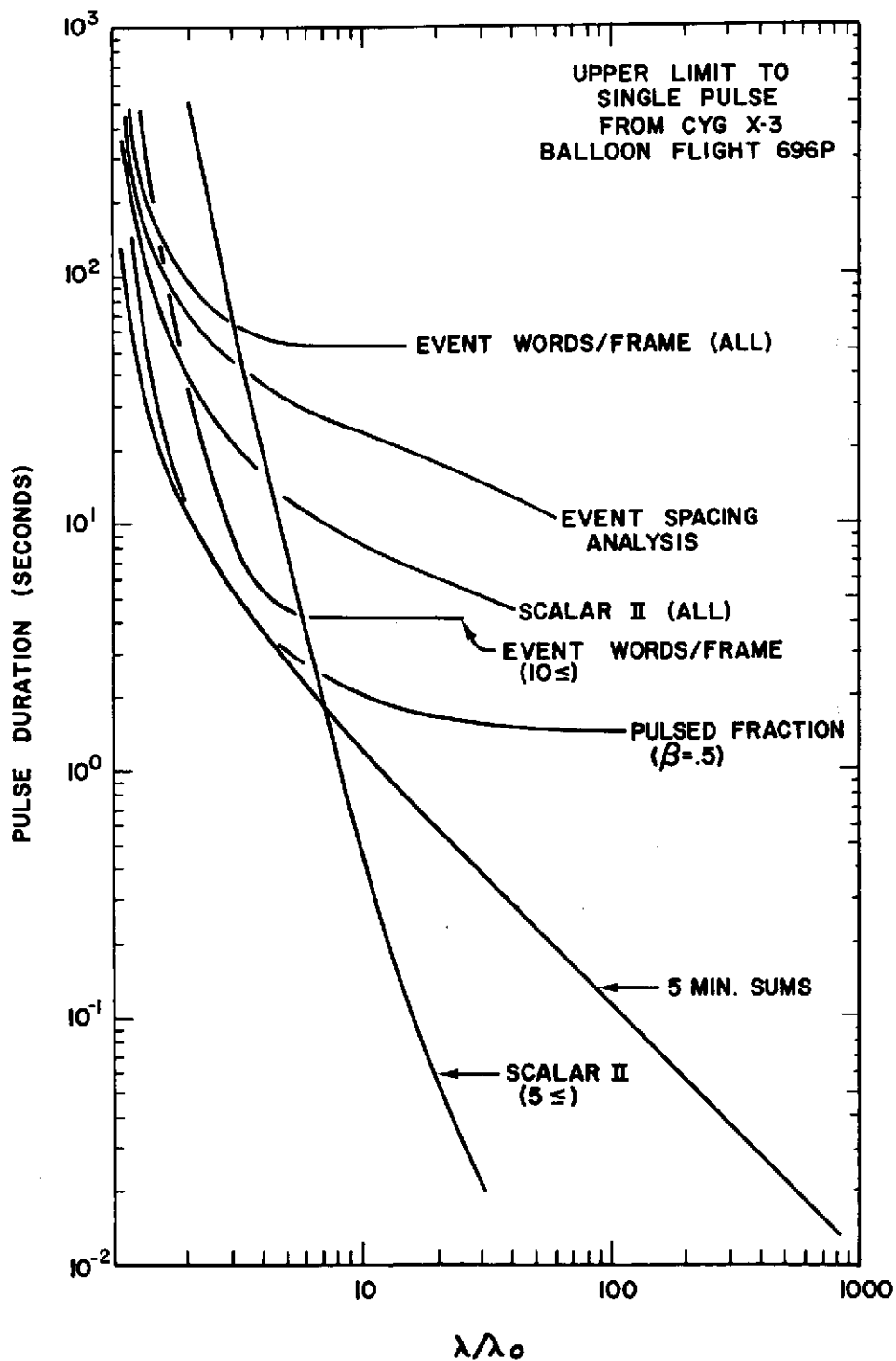


Figure 5.14 - Upper limits on the duration of a single pulse at a 3σ level vs. the fractional increase in count rate λ/λ_0 for Cyg X-3 as observed from balloon flight 696-P.

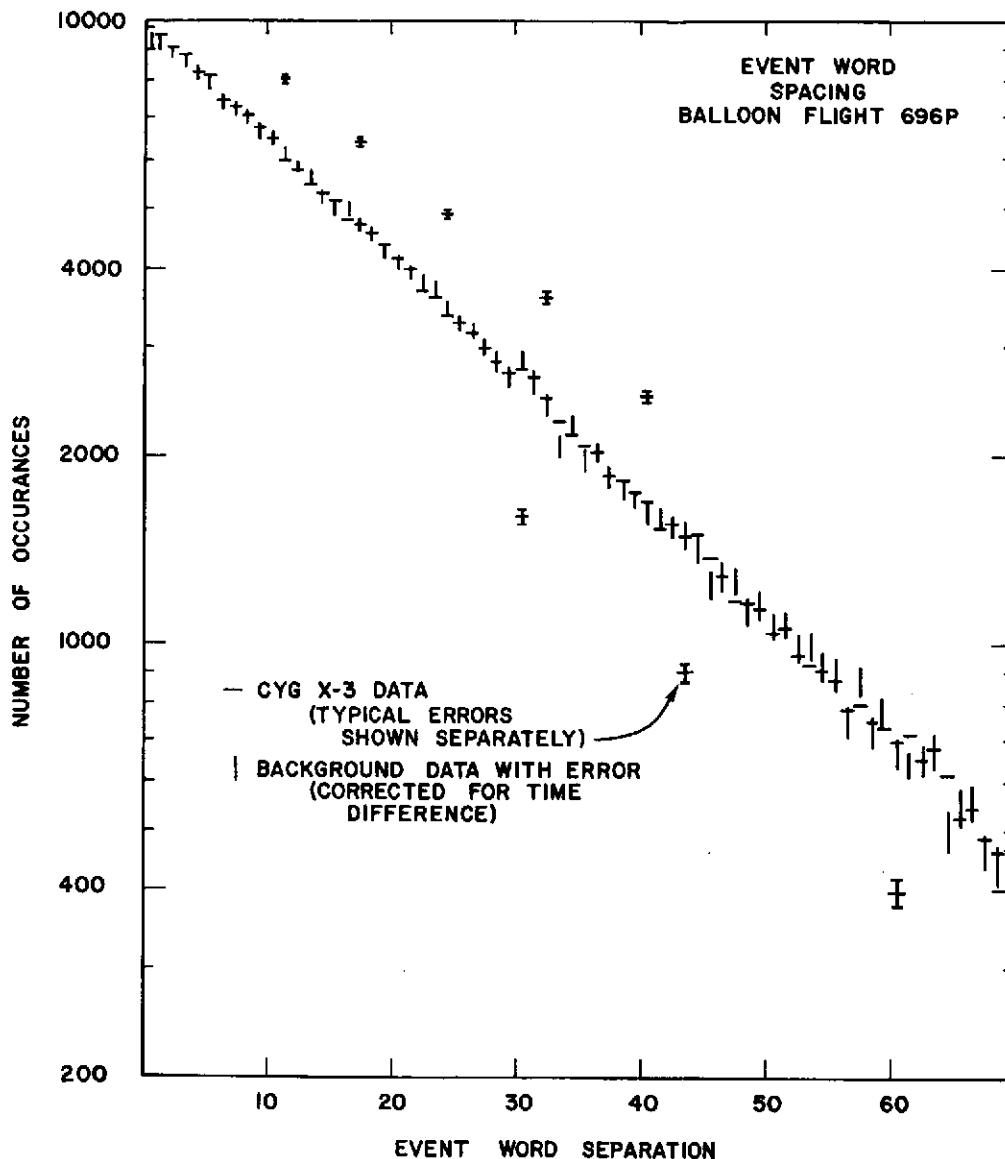


Figure 5.15 - Event word spacing distribution for balloon flight 696-P. Typical error bars for the source data are plotted to the side while error bars for the background data are shown by the vertical bar.

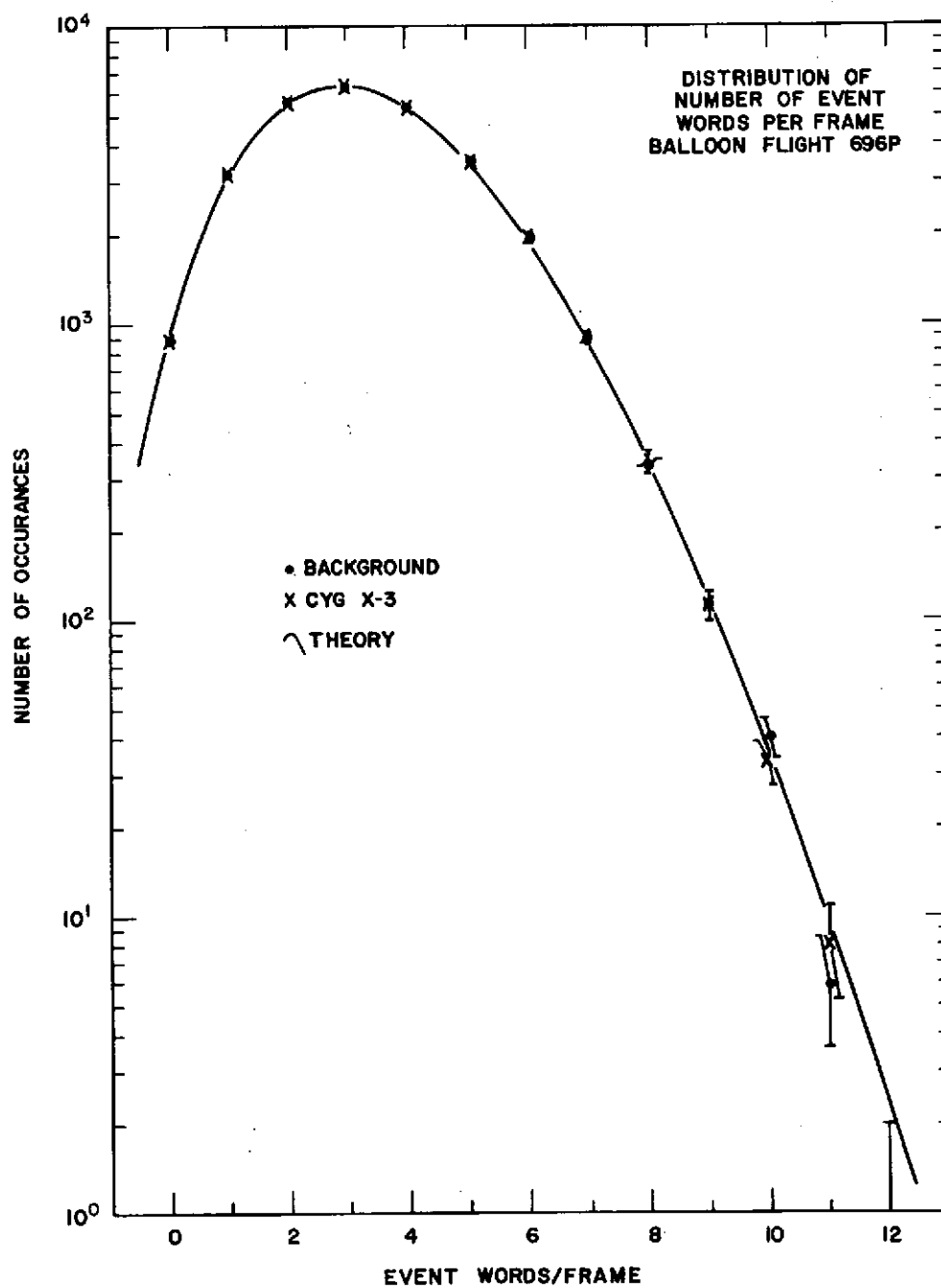


Figure 5.16 - Distribution of number of event words per frame for balloon flight 696-P showing complete agreement between source and background data.

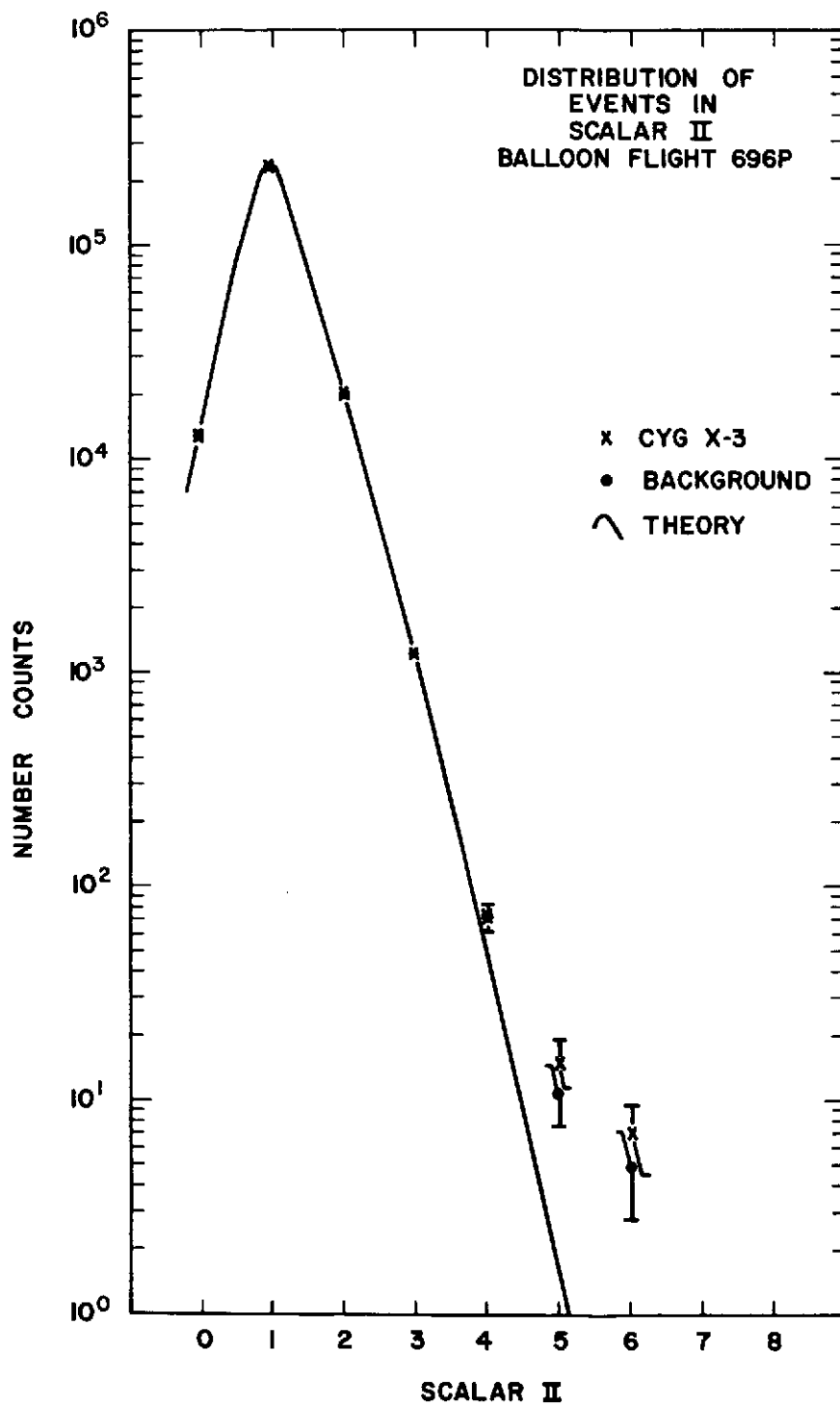


Figure 5.17 - Distribution of events in Scalar II for balloon flight 696-P.

613

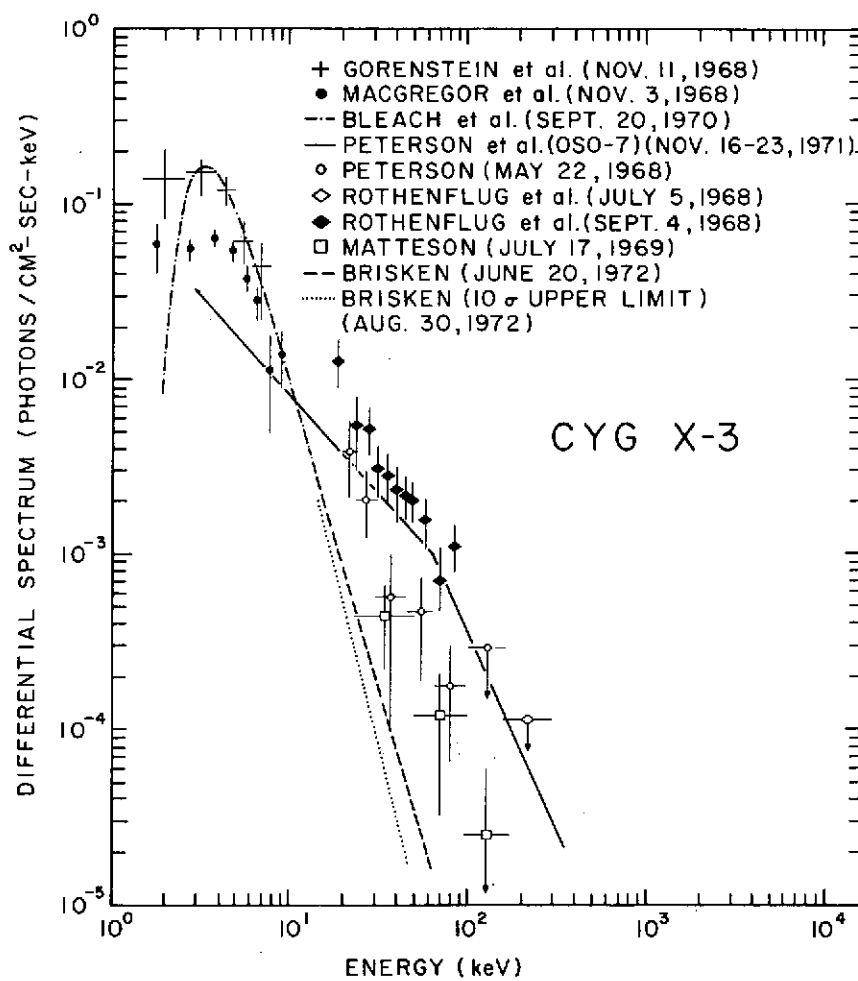


Figure 5.18 - Photon flux (photons/cm²sec keV) of Cyg X-3 as observed by several experiments.

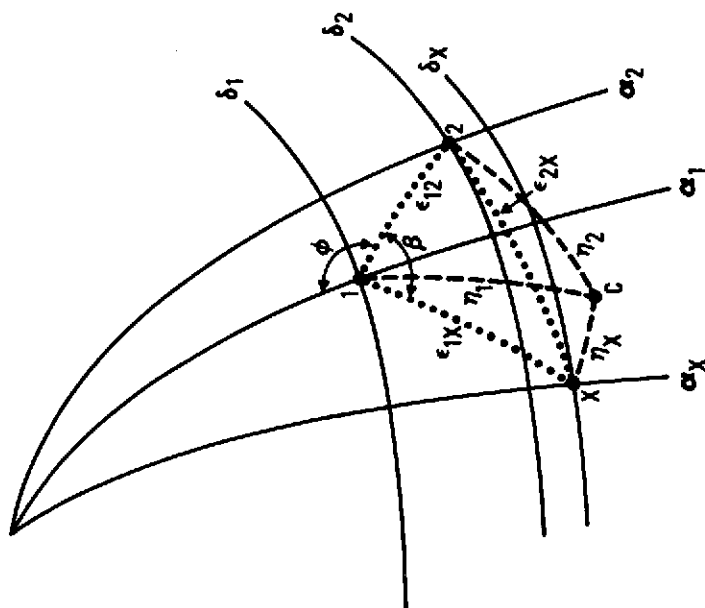
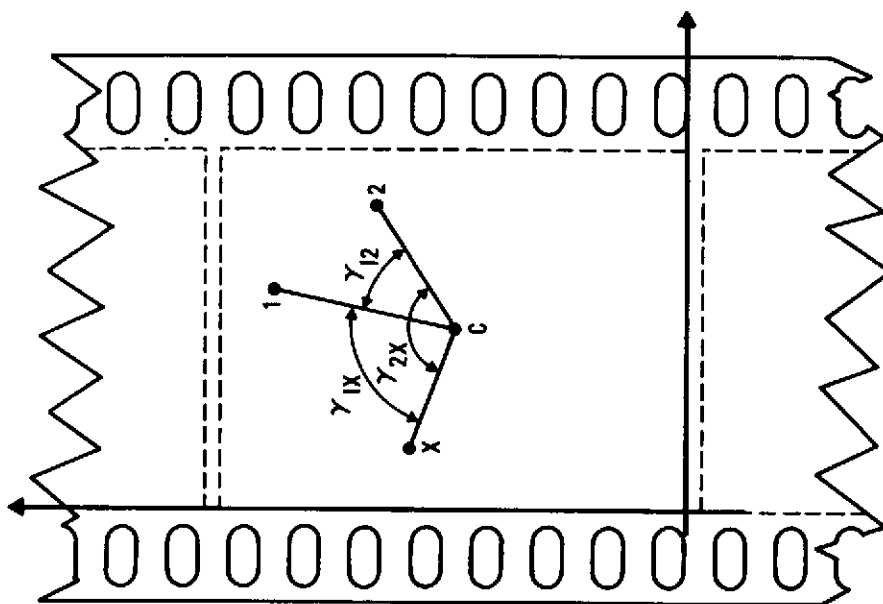


Figure A1 - Coordinate system used in star field analysis in the celestial sphere (a) and the plane of the photograph (b).